UNIVERSITÀ DEGLI STUDI DI CATANIA
DOTTORATO DI RICERCA IN INGEGNERIA FISICA

ROBERTO PAGANO

OPERATIVE PARAMETERS OF Si PHOTOMULTIPLIERS

Coordinatore: *Prof. G. Giaquinta*
Tutor: *Prof. G. Falci*
Supervisori: *Dott. S. Lombardo*
Dott.ssa S. Libertino

Tesi per il conseguimento del titolo di dottorato
XXII-Ciclo

INDEX

Chapter 2

Single Pixel: Electrical and Optical Characterization…….56

Chapter 3

SiPM Characterization……96

Introduction

Silicon Photomultipliers (SiPMs) are a very promising alternative to conventional photomultipliers (PM) thanks to some interesting characteristics: they are insensitive to magnetic fields, hence can be used in environments with high fields; their operation voltage is far lower, and they ensure better robustness and reliability than PM; they are much cheaper than their traditional counterpart.

SiPM structure consists in a parallel array of equal single pixels, each one made of a silicon p-n junction avalanche photodetector with an integrated resistor. The SiPM is biased above the breakdown voltage, that is, each pixel is operated in Geiger mode, above the breakdown voltage (BV) of the p-n junction. The junction is carefully doped in order to have breakdown only in the central active area of the pixel, used for the photon detection, and by the avalanche mechanism (not by Zener). To understand the photon detection concept, let us assume to bias such junction above breakdown with a fast voltage step. In this condition, if no carrier is present in the depletion region the junction is highly sensitive to the detection of single photons. In fact, if the photon is absorbed by creating an electron-hole pair, both carriers will start to drift in the high field region of the depletion layer and, being the voltage above breakdown, this drift will result with a 100% probability in the impact generation of a second e-h pair, and so on, up to the build-up of the junction avalanche. The avalanche is limited by the buildup of a limiting space charge in the depletion layer which decreases the field Moreover, since the photodetector has a resistor in series, when the avalanche current flows through the resistor, the voltage applied to the junction drops below BV. It quenches the avalanche, the current decreases to zero, and the voltage across the p-n junction increases again above BV. The pixel is ready again to detect the arrival of a new photon. Clearly, all the

transients recorded are the result of both capacitive effects and (generally faster) avalanche build-up characteristic times.

Such ideal picture is strongly modified by the occurrence of phenomena leading to dark current, generally attributed to generation effects from Shockley-Read-Hall (SRH) defects in the depletion layer, afterpulsing effects, and diffusion of carriers from the quasi-neutral boundaries of the p-n junction .

The purpose of this work was to understand the behavior of dark current in single pixels of SiPMs. Chapter 1 introduces the field of research. It reports the most important characteristics that photomultipliers must have and a brief comparison between traditional photomultipliers and SiPM. A brief history of SiPM invention and devolution is also discussed.

Chapter 2 reports a detailed experimental characterization of single pixels. In particular, current voltage (I-V) characteristics in both forward and reverse biases were collected. The careful analysis of the data allowed us to obtain information on the junction quality (ideality factor) and on the behavior in the operation range. Moreover, by taking into account the contribution given by the avalanche build-up and quenching and the effect of generation / diffusion of carriers in the depletion layer, we provided a detailed understanding of the I-V curves. We also proposed a physical model of the I-V above breakdown voltage able to reproduce the voltage and temperature dependence of the current for the studied devices, still in Chapter 2.

The current-voltage characteristics of matrixes from 5×5 pixels up to 64×64 pixels (pre-commercial devices) are reported in Chapter 3. In this chapter some fabrication issues are also shown: the uniformity problem, the effect of the presence of optical trenches (introduced to improve the structure performances) and the importance of the substrate dopant.

Finally, Chapter 4 reports some preliminary results on the effect of irradiation on the devices. In particular, measurements were performed after irradiating the devices with different species: X-rays, light ions (Boron) and heavy ions (Brome and Gold)

Chapter 1

SiPM: principles and features

The ability to detect single photons represents the ultimate goal in optical detection. To achieve such sensitivity a number of technologies have been developed and refined to suit particular applications. These include: Photomultiplier Tubes (PMTs), Microchannel Pate Photomultiplier Tubes (MCPMT), Hybrid Photon Detector (HPD), p-i-n photodiodes, linear and Geiger mode Avalanche Photo Diodes (APDs) and much more. The need for ever more sensitive, compact, rugged and inexpensive optical sensors in the visible region of the spectrum continues today, and is particularly acute in the fields of the biological sciences, medicine, astronomy and high energy physics. Applications such as fluorescence and luminescence photometry, absorption spectroscopy, scintillation readout, light detection and ranging and quantum cryptography require extremely sensitive optical sensors often in adverse environments, such as high magnetic fields, and where space is limited.

In many of these applications the PMT has become the detector of choice. However, since its inception in the 1980's, the so-called silicon photomultiplier (SiPM) has begun to rival the PMT in many of its parameters such as gain, photon detection efficiency and timing. In addition, the SiPM has all the additional benefits of silicon technology such as compactness, high volume, low cost production.

In the next sections we will briefly introduce the photodetectors characteristics, we will then discuss the history of SiPM birth, its operation principle and properties and, finally, we will get a look on some application fields.

§ 1.1 Introduction to Photodetectors

Photodetectors are electronic devices that give an electrical output signal in response to a light input signal. They are essential elements in any optoelectronics system and their importance is comparable to the light source.

The genesis of photodetectors can be ascribed to the discovery of the photoconductivity (1873 by W. Smith) [1]. Great breakthroughs occurred with the discovery of the photoelectric effect by Millikan and its interpretation by Einstein in 1905 [2] and with the introduction of the quanta hypothesis to solve the blackbody emission [3-4] by Planck. Since then, different and equally important devices were invented. The most popular are the photoelectric vacuum-tubes, including the photomultiplier tube (PMT), and the semiconductor photodetectors.

A photodetector is generally characterized by different properties, which are normally the average value of a statistical distribution [5]. Since all of them will be widely discussed in the following sections of this chapter, here they will be only listed, and they are:

- *Quantum efficiency* (*QE* or ε_Q): it is the probability that a photon incident on the active surface of the detector generates a photoelectron. ($0<\varepsilon_Q<1$).
- *Collection efficiency* (*CE* or ε_C): it is the probability that a generated photoelectron start the electron amplification mechanism ($0<\varepsilon_C<1$)[1].
- *Gain* (*G*): it is the mean value of the charge produced by the internal electron amplification mechanism per photoelectron generated.
- *Dark Current* or *Dark Noise*: it is the electrical current produced by the internal noise mechanisms of the photodetector in dark condition (i.e. when no photons strike the sensitive area of the detector).

[1] The term *photon detection efficiency* (PDE) is often used for the combined probability to produce a photoelectron and to detect it (PDE=$\varepsilon_C \cdot \varepsilon_G$).

- *Dynamic range* and *Linearity*: it is the maximum signal produced by the detector without a significant distortion with respect to the input signal.
- *Response time*: this includes the transit time, that is the time elapsed between the photon arrival time and the electrical output response of the detector, and the transit time spread, which contributes to the pulse rise time and the duration.
- *Single photon detection capability*: it is important when measuring very low photon flux.
- *Rate Capability*: it is the maximum rate for photon detection and it is inversely proportional to the time needed, after the arrival of a photon, to get ready to detect the next.
- *Stability*: essential for long term operation at elevated counting rate.

Before starting the description of Silicon photomultipliers, the object of this thesis, it is fundamental to briefly review the most diffused photodetector used in ultra-weak photon detection.

1.1.1 Vacuum photodetector

In a vacuum photodetector the photocathode and the electron multiplication stage are enclosed in a vessel made of glass or ceramics. Vacuum photodetector are of three types: photomultiplier tube (PMT), microchannel plate photomultiplier tube (MCP) and hybrid photodetector (HPD).

The PMT was proposed almost 100 years ago, in 1919, by J. Slepian [6] and the first real device was demonstrated by Iams and Salzberg in 1935 [7] and by Zworikyn in 1936 [8]. PMT has been unrivaled by semiconductor photodetectors in the single photons detection field for long time, thanks to its good response speed and its very low excess noise. Up to now, PMTs are widely used in many applications where a low photon flux must be detected.

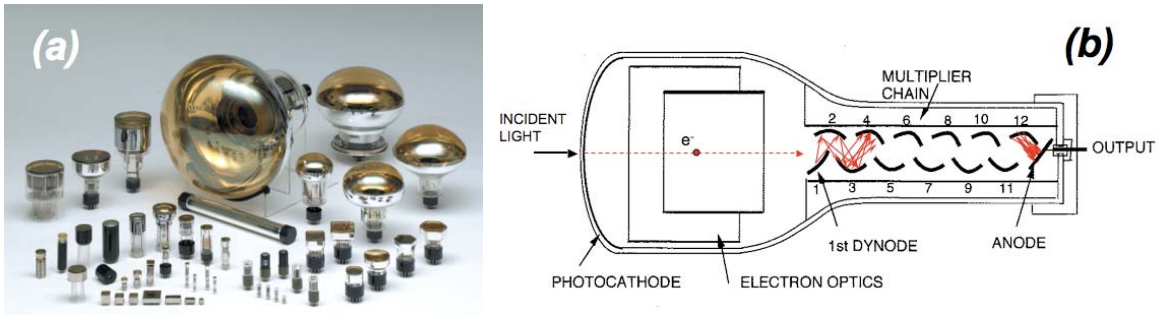

Figure 1.1: *(a) PMT's typical format [9]; (b) Basic structure of a PMT.*

They are fabricated in different formats (some examples are shown in Figure 1.1 (a) and very large sensitive area up to 50×50 cm^2 can be realized.

The basic structure of a photomultiplier tube, shown in Figure 1.1 (b), is composed of a photocathode (mostly in transmission, sometimes in reflections[2]), an electron optics (missing in slow units and in compact devices), a dynode chain that yields a high internal gain of charge multiplication, an anode (output electrode) to collect the amplified charge. A bias voltage of hundred Volts is applied between the photocathode and the first dynode, as well as between the successive dynodes. Such high voltage is needed to ensure that the photo-emitted electrons will hit the next electrode with adequate energy for the multiplication (~100 eV), and that the collection efficiency will be close to the unity.

The photocathode is a thin semiconductor film, with a suitably low work function. When a photon impinges on the photocathode sensitive surface an electron is generated by photoelectric effect. This photoelectron is then accelerated by the high electric field and guided (focused) by the electron optics to hit the first dynode. At the first dynode, the primary photoelectron produces the emission of g electrons from the dynode, by a phenomenon know as secondary emission. Secondary electrons leaving the first dynode are accelerated to the second dynode, where they produce g^2 electrons, and so on up to the last dynode. For n dynodes, at the anode we will find g^n electrons. The gain (G) is g^n, is very high even for a

[2] In a reflection photocathode the electrons are emitted from the same side surface on which photons impinge, in a transmission photocathode the electrons are emitted from the opposite side surface.

moderate g: for example, for g=4, with n=8...14, we get $G=6\cdot10^4\ldots2\cdot10^7$, respectively. The current collected at the anode is in the order of few mA even for a single photon detected and can be directly processed with standard electronic instrumentations. The total gain depends on the applied voltage U as $G=AU^{kn}$, where k ~ 0.7 —0.8 (depending on the dynode material), n is the number of dynodes and A is a constant (which also depend on n).

The sensitive wavelength range covered by a PMT depends on the photocathode material (long wavelength cut-off) and on the light enter window material (short wavelength cut-off).

Despite of the complex amplification process, the response to the light impulse is relatively fast, few nanosecond duration. The critical drawback of PMTs is their sensitivity to external magnetic field (sometimes even to the geomagnetic one). It deflects electron in flight from their standard trajectory causing a loss in the efficiency and in the gain and an increase in the time spread $\Delta\tau_d$. A high-permeability metal shield is often necessary to allow operation in moderate fields, up to ~ 0.1T. Moreover, since the electrode structure is not so rugged, photomultipliers are not immune to vibrations, that could induce the modulation of the gain during normal operation. Finally, the high bias voltage required (1000 — 2000V) between the anode and the cathode induces a high power consumption.

In a MCP the discrete dynode chain is replaced by continuous multiplication in 6-20 μm diameter cylindrical holes, or channel (Figure 1.2 (a) and (b)). These channels are densely

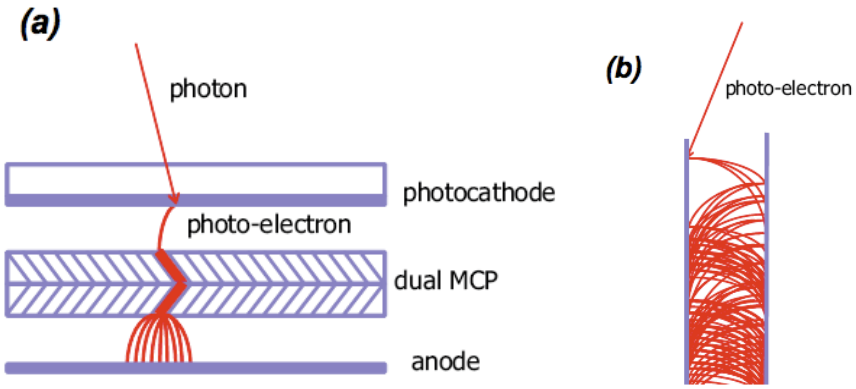

Figure 1.2: *(a) Microchannel plate photomultiplier tube, (b) electron multiplication in a channel [10].*

packed in few mm thick glass plate. The inner channel walls are processed to have proper electric resistance and secondary emission properties. The multiplication gain depends exponentially on the ratio of the channel length to its diameter. A typical value of this ratio is 40, and a typical gain of a single microchannel plate is ~ 10^4. For higher gain to or more channel plates are used in series. MCP offer good spatial resolution, excellent time resolution (~20ps) and can tolerate axial magnetic fields exciding 2T. However, they suffer of a relative long recovery time and a short lifetime.

HPD combine the sensitivity of a vacuum PMT with the excellent spatial resolution of a Si detector [11]. The photoelectron is accelerated trough a potential difference of ~ 10÷20 kV before hits the silicon sensor as shown in Figure 1.3. The electric field is usually shaped in such away that the entry light is de-magnified onto the silicon sensor that can be smaller than the window. The gain is smaller than in typical PMT and a low-noise amplifier must be used to read out when low photon flux must be detected. HPD also requires high bias voltage and it can't work in magnetic field.

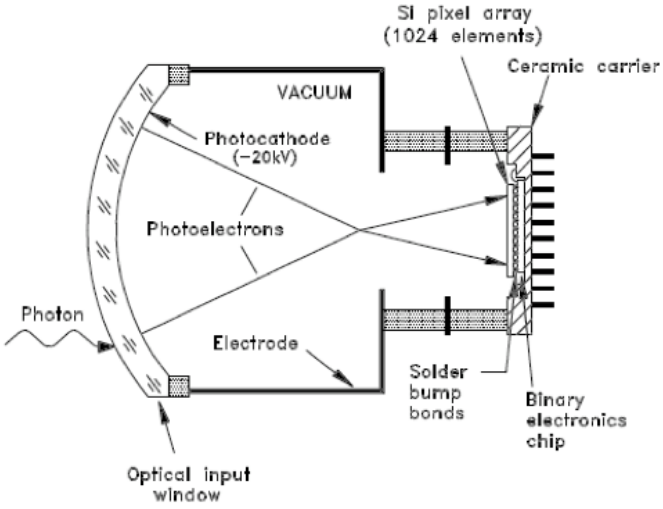

Figure 1.3: *Hyprid photon detetctor. The larger photocathode surface isimaged onto a much smaller Si sensor by a suitable shaped electric field [12].*

1.1.2 Semiconductor Photodetectors

Semiconductor photodetectors were developed after the Second World War thanks to the progresses obtained in the comprehension of their physics and to the improvement in the control of their technology. Semiconductor detectors are solid-state devices exploiting the internal photoelectric effect, as opposed to photoemission effect of vacuum photodetectors. In them, the charge-carries pairs generated by photon absorption contribute to electrical conduction internal to the device, and to a corresponding current at the contacts of external circuit. Thus, in a semiconductor photodetector, detection and production of photoelectrons take place in the same thin material.

Absorption of photons will depend on the semiconductor characteristics (for a detailed discussion on photon absorption in semiconductors see APPENDIX A). In order to generate a charge carrier pair in the semiconductor material, photons need to have sufficient energy $h\nu > E$, where E is the energy that must by supplied at the expense of the photon energy $h\nu$. This condition leads to a long wavelength cutoff $\lambda_c = hc/E$ for the absorbed photon wavelength. Concerning the energy E suitable for photon absorption, in intrinsic semiconductor, where the photon absorption produces a transition of an electron from the valence band into the conduction band, E is equal to E_G, the energy gap of the semiconductor. In extrinsic semiconductor energy levels in the forbidden-gap are involved in the carrier generation. The long-wavelength cutoff then will depend on the energy level position in the bandgap. In silicon, that is an intrinsic semiconductor, photon with wavelength shorter than about 1050 nm (i.e with energy exceeding the silicon bandgap E_g=1.12 eV) can create electron-hole pairs by the photoelectric effect.

A silicon photodiode, in its simplest form, is a reverse-biased p-n junction (as shown in Figure 1.4), and the electron and hole are collected on the p and n side, respectively.

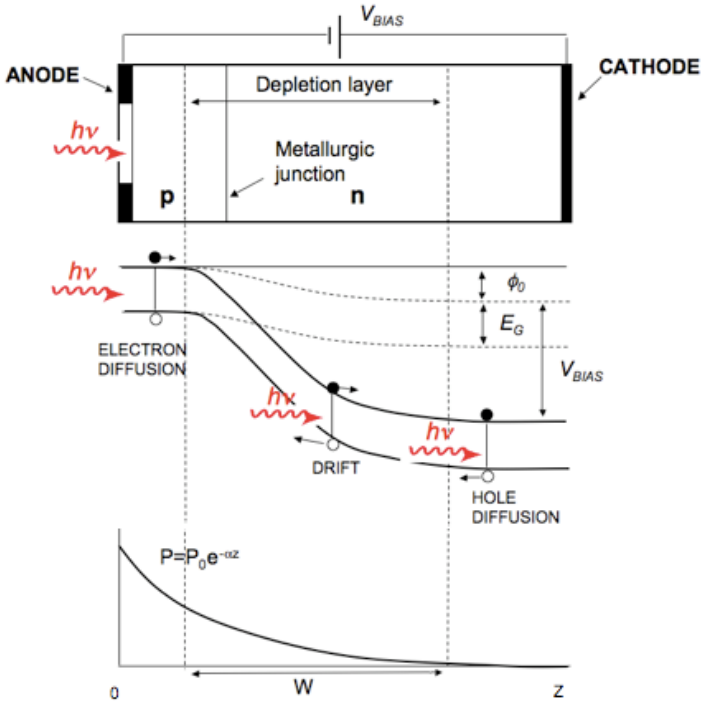

Figure 1.4: *Representation of a p-n junction photodiode, the photo-generated charge transport mechanism and the optical transmitted power.*

Radiation is incident on the p-type region which carrier the ohmic anode contact, a metallization shaped as a ring around the access window to avoid optical obstruction. The p region is made relatively thin, by doping it more heavily than the n region, so that photons have a good chance to cross it and be absorbed in the depleted region of the junction.

The charge carriers (electron and hole) generated by absorption of photons with energy $h\nu \geq E_G$, decrease exponentially with depth z like the optical power (see Figure 1.4). The main contribution to photogenerated current comes from the pairs generated in the depleted layer. Here, electrons and holes are separated by the electric field and by drift they reach the neutral-charge regions where they are collected by the electrodes.

The PIN photodiode is the most common type of photodiodes used in low light detection. It is an intrinsic piece semiconductor sandwiched between two heavily doped n+ and p+ regions (Figure 1.5). The reverse bias increases the thickness of the depleted region. This has two benefits with respect to other devices: the decrease of electronics noise due to a lower capacitance and an improved sensitivity at higher wavelengths because the absorption length (Figure 1.6) is comparable to the thickness of the sensitive region (typical 100µm). The

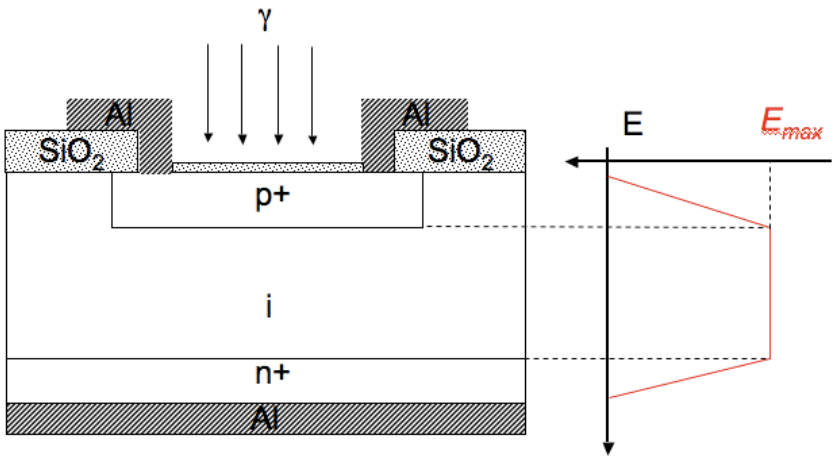

Figure 1.5 *Structure of a p-i-n avalanche photodiode and its electrical field for a reverse polarization.*

quantum efficiency can exceed 90%, but decreases towards longer wavelengths because of the increasing absorption length of light in silicon.

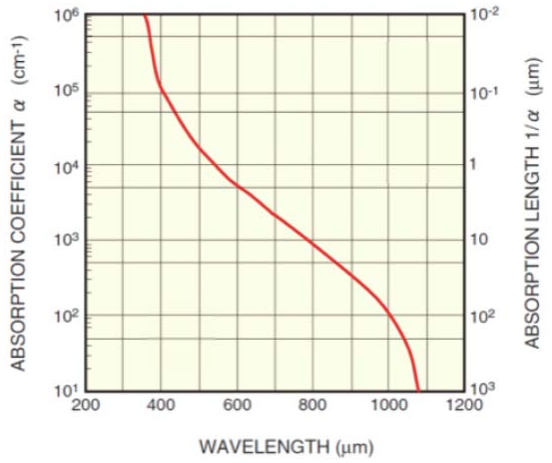

Figure 1.6 *Absorption coefficient α and absorption length 1/α in silicon semiconductors.*

Since there is no electron multiplication (G=1), amplification of the signal is needed. Low light level signal detection is limited to a few hundred photons even if an amplifier is used.

Avalanche photodiode (APD's) have similar structure of regular photodiodes, but they are operated at a much higher reverse bias. This allows each photo-generated carrier to get multiplied in an avalanche, resulting in an internal gain (typical G=10÷200) within the photodiode [13]. As a result, a detectable electrical response can be obtained from low intensity optical signals, as low as 10÷20 photons. Well designed APDS have achieved photon detection efficiency of ~70% with sub-ns response time [14].

The sensitive wavelength window and the gain depend on the semiconductor used. Stability and monitoring of the operating temperature are important for the linear-mode operation and cooling is often necessary.

The APD can also be biased at voltage larger than the breakdown voltage resulting in a infinity gain operation. An external load of high value limit the maximum current to a safe mode. This working regime is called Geiger Mode, since the APD is more akin to a Geiger-Muller counter. With an APD working in GM mode, we can get an output pulse for each detected photon. It has to be noted that in GM-APD, also called, SPAD (Single Photon Avalanche Detector) one ore more photons produce the same output pulse.

Since the devices discussed in the rest of this work are particularly designed APDs working in GM, most of the photodiode characteristics, such as the multiplication gain M, the quantum efficiency, noise, will be better discussed in the following sections, referring to those devices.

		VACUUM PHOTDETECTOR			SEMICONDUCTOR PHOTODETECTORS		
		PMT	**MCP-PMT**	**HPD**	**PN, PIN**	**APD**	**GM-APD, SiPM**
Photon detection efficiency	**Blue**	20 %	20 %	20 %	60 %	50 %	30%
	Green-yellow	40 %	40 %	40 %	80-90 %	60-70 %	50%
	Red	< 6 %	< 6 %	< 6 %	90-100 %	80 %	40%
Timing / 10 ph.e		~ 100 ps	~ 10 ps	~ 100 ps	tens ns	few ns	tens of ps
Gain		10^6 - 10^7	10^6 - 10^7	3 - 8x10^3	1	~ 200	10^5 - 10^6
Operation voltage		1 kV	3 kV	20 kV	10-100V	100-500V	< 100 V
Operation in the magnetic field		< 10^{-3} T	Axial magnetic field ~ 2 T	Axial magnetic field ~ 4 T	No sensitivity	No sensitivity	No sensitivity
Photons sensitivity		1 ph.e	1 ph.e	1 ph.e	~100 ph.e	~10 ph.e	~1 ph.e
Shape characteristics		sensible bulky	compact	sensible, bulky	robust, compact, mechanically rugged		

Table 1.1: *Vacuum and semiconductor photodetector characteristics.*

Compared to traditional vacuum-based detector, semiconductor detectors have several advantages. They are compact and robust, do not require high voltages, and are insensitive to magnetic fields. An other advantage is the low cost due to the relative inexpensive production method.

In Table 1.1 are compared the most relevant characteristics of the vacuum and semiconductor photodetectors discussed and those of a Silicon Photomultiplier, the argument of this thesis.

§ 1.2 SiPM History

The Silicon Photomultiplier (SiPM) is the last born in the family of solid state photodetectors and the research and development to reach better performances is ongoing.

The first pioneers in the development of a solid state detector working in the so called Geiger mode, that is, biased over the breakdown voltage, were R. J. McIntyre and is coworkers at the RCA company and R. H. Haitz and his colleagues in the Shockley research laboratory, during studies on the physics of avalanche multiplication with high electric field intensity in semiconductor devices [15-16]. This was at the beginning of the sixties of the last century. The work of McIntyre and Haitz led to a basic insight in the phenomenon of avalanche breakdown, the physical phenomena involved in the avalanche buildup after the arrival of a photon, and in dark-current pulses. They provided important insight for the modeling of the behavior of the device operating in Geiger mode [17-18]. The two test structures fabricated and described by the two groups are shown in Figure 1.7. These structures were not conceived as photodetectors, and their performances were indeed severely limited by the technology available at that time for silicon devices. The main problems derived from the instability of the breakdown over the whole sensitive area of the detector. In fact, only a small volume of silicon could be depleted for the long time needed to detect photons due to the presence of many defects created during the fabrication process.

Only with the improvement of the fabrication technology, it was possible to fabricate the first planar Single Photon Avalanche Diode (SPAD) and the Super-low k APD structure (SLIK^{TM}, used nowadays in the Single Photon Counting Modules SPCM produced by Perkin Elmer Optoelectronics [19]). The quenching of the breakdown voltage was obtained using a large external resistance, like in the Geiger counter, that reduces the voltage applied to the junction below the breakdown value so that it quenches the spread of the avalanche current. In this way the recovery time, i.e. the time needed to quench the avalanche and restore the

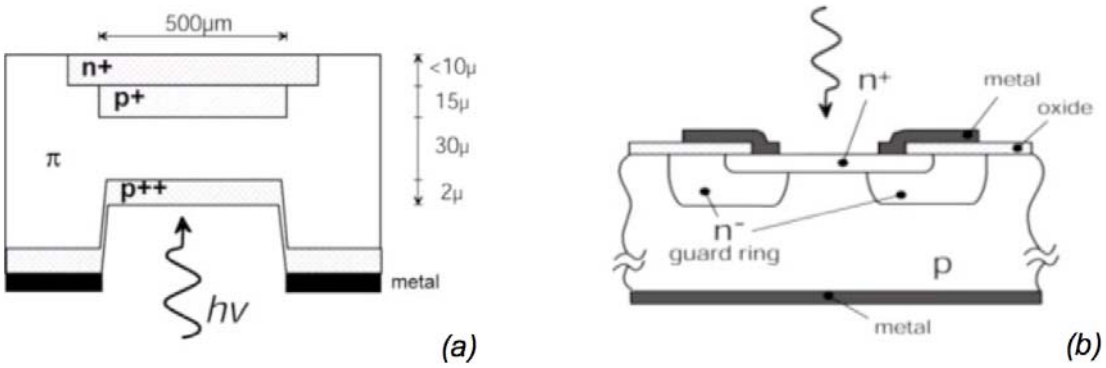

Figure 1.7: *The first two prototypes of silicon single photon detector. (a) The reach-trough structure realized at the RCA company by McIntyre group. (b) The planar n+p junction operating in Geiger mode developed at the Shockley laboratory by Haitz.*

voltage over the breakdown value, was slow. The maximum counting rate that could be achieved was smaller than 100 kHz. The development of active quenching circuits, started in the eighties, allowed to improve the SPAD counting rate to more than 1 MHz, thus reducing the recovery and dead time [20-21].

The next logical step was to try to fabricate many individual single photon avalanche diodes quenched either in passive mode (i.e. with an external resistor) or in active mode (i.e. using an integrated quenching circuit) in a single silicon wafer. At the end of the nineties, the RMD company (Radiation Monitor Devices Inc.) developed an array of 6×14 avalanche photon diodes operating in Geiger mode with single photon avalanche capability. It was used for the detection of internally reflected Cherenkov light. Each APD was quenched using an active quenching circuit [22].

At the same time, in Russia was invented the MRS APD (Metal Resistor Semiconductor Avalanche Photodiode). It consists of a p^+n or an n^+p junction designed to work over the breakdown voltage with a thin metal layer on the top of the structure (Ti~0.01 μm) covering a resistive layer made with SiC or Si_XO_Y (30-80 MΩ cm). The resistive layer on the top of the junction realized the negative feedback in the local area of the multiplication process to switch off the avalanche: the avalanche process increases the current through the resistive layer at the silicon interface redistributing the potential in the structure. This causes a

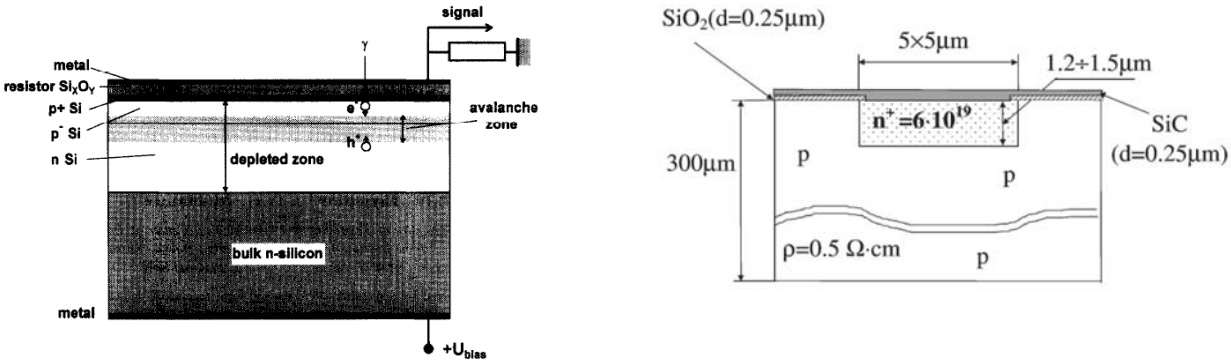

Figure 1.8: *Scheme of different Metal Resistor Semiconductor (MRS) structures with single photon detection capability in the light and near UV wavelenght: (a) MRS structure with Si_XO_Y resitor layer from [23], MRS structure with SiC resistive layer from [24].*

deceleration of the avalanche process itself and finally its termination. It is to be noted that the resistive layer negative feedback has a local nature due to a very low tangential conductivity of the resistive layer. In Figure 1.8 are shown two examples of different MRS structures; the first has an Si_XO_Y resistive layer consisting essentially of SiO_2 interspersed with amorphous silicon (Figure 2a), and the second with a SiC resistive layer, (Figure 2b). The resistive layer on the top of the Silicon surface is an important feature of the structure. As already said, it performs the quench of the avalanche process by a local negative feedback, thus stabilizing the avalanche process itself. At the same time it realizes an electrical decoupling agent between adjacent identical structures. This allows the production of a large numbers of microcells in a very fine structure on a common substrate with common electrodes, as shown in Figure 1.9. This structure represents therefore the birth of the silicon photon multiplier. Key personalities in this development were V. Golovin [25] and Z. Sadygov [26]. The technology for producing the SiPM is compatible with the standard Metal Oxide Silicon (MOS) process and promises the realization of sensors with a great area and a large number of micro cells at low cost of fabrication. From this initial seed, many different configuration and structures have been proposed and numerous new developments are ongoing. Nowadays, a few first generation devices are commercially available, but the level of maturity of the conventional PMT has still not been reached. In Table 1.2 are listed all the producers that are

involved, till today, in the fabrication and development of this sensor. Every producer uses its own name for this type of device (for a complete list of the names used see Table 1.3) but the basic structure of all the commercially available sensor is the same and it is reproduced in Figure 1.10. Devices with up to 40.000 cell/mm^2 are nowadays available.

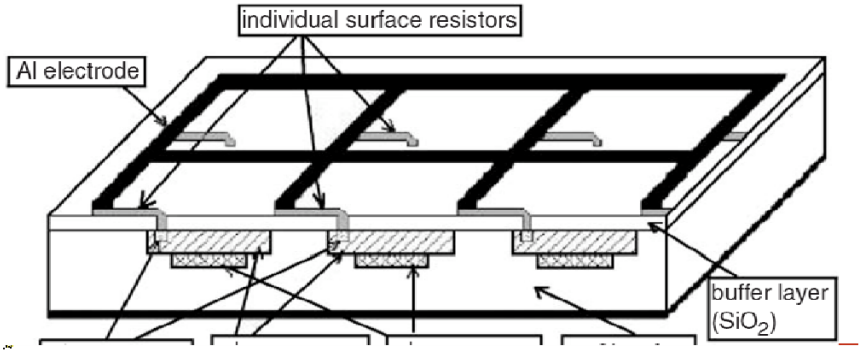

Figure 1.9: *Basic structure of Silicon Photomultiplier (SiPM) taken from [26].*

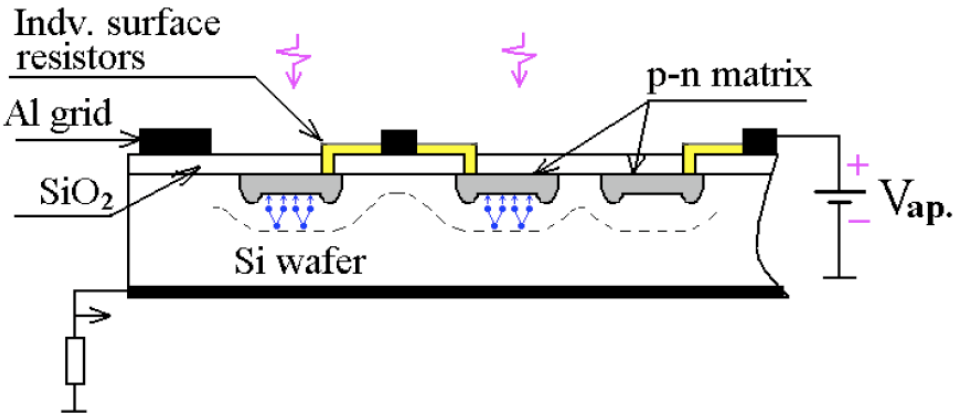

Figure 1.10: *Schematic cross section of a SiPM. Each pixel has an individual surface resistors connected to a common contact via a metal grid [27].*

Producer/Developer	Country	Detector Acronym
CPTA/Photonique	Moscow /Geneva	MRS APD/SSPM
Zecotek	Singapore	MAPD
MEPhI/Pulsar	Moscow (Russia)	MRS APD
Amplification Technologies	Orlando (USA)	DAPD
Hamamatsu Photonique	Hamamatsu (Japan)	MPPC
SenSL	Cork (Ireland)	SPM
RMD	Boston (USA)	
MPI Semiconductor Laboratory	Munich (Germany)	
Voxtel	Beaverton (USA)	SiPM
FBK-irst	Trento (Italy)	SiPM
ST Microelectronics	Catania (Italy)	SiPM

Table 1.2: *Producer and developer of Silicon Photomultiplier over the world.*

Acronym	Extended Name
SiPM	Silicon Photomultiplier
MRS APD	Metal Resistor Semiconductor Avalanche Photodiode
MAPD	Micro-pixel Avalanche Photodiode
MPPC	Multi-Pixel Photon Counter
SPM	Silicon Photomultiplier
SSPM	Solid State Photomultiplier
PPD	Pixelated Photon Detector
DAPD	Discrete Amplification Photon Detector
AMPD	Avalanche Microchannel Photodiode
GM-APD	Geiger Mode Avalanche Photodiode

Table 1.3: *Acronyms used in literature or coined by producer to identify the SiPM.*

§ 1.3 Description and principle of operation

The Silicon Photomultiplier, as already said, is a pixilated photon detector, formed by a matrix of independent cells. Each cell (or pixel) is connected to the others by metal grids so to have common contacts. In Figure 1.11(a) a photograph of a real commercial silicon photomultiplier produced by Hamamatsu Photonique with an area of 3×3 mm^2 is shown. The schematic structure of the SiPM is proposed in Figure 1.11(b): a matrix of N×N cell is fabricated on a common substrate (the yellow layer). The active volume of the device, where photons are mainly absorbed and the carrier pairs produced are multiplied by the intrinsic mechanism of amplification of the device, is confined in a few microns under the top surface (white layer). Finally a metallization grid is fabricated on the top of the structure in order to connect all the N×N pixels each to the others. The single cell (a schematic cross section is shown in Figure 1.11(c) is essentially an APD operating in the Geiger mode (GM-APD) with an integrated resistor in series whose goal is double: the quenching of the avalanche breakdown when the cell is fired by an incoming photon and the isolation between adjacent cells. To better understand the working principle of the whole detector it is helpful to briefly discuss the physics involved in the amplification of photons in an APD and the operation in Geiger Mode.

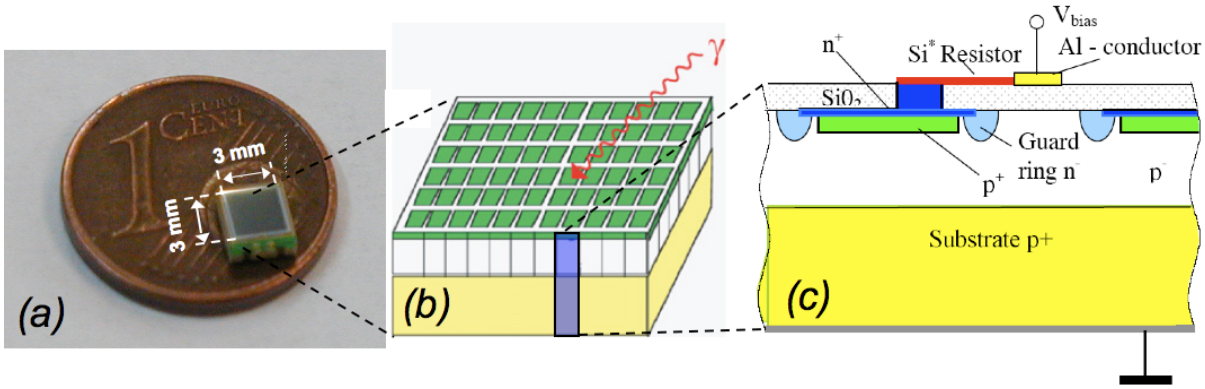

Figure 1.11 *(a) Photography of a SiPM produced by Hamamatsu Photonic (MPPC S10931-050P) with 3×3 mm^2 area. (b) Schematic view of a SiPM structure. (c) Cross section of a single cell.*

In an APD the weak light detected is internally amplified The avalanche multiplication by impact ionization is the mechanism that allows the photogenerated carriers amplification. The avalanche is obtained by applying a high reverse bias voltage to the photodiode, so as to bring it into the breakdown region usually avoided in normal operation.

The structure we will use to describe the multiplication process is, for simplicity, a p-i-n avalanche photodiode, schematically shown in Figure 1.5. In a p-i-n avalanche photodiode, as previously discussed, an intrinsic region i, is fabricated between the p^+ and the n^+ regions. The electric field (E) in the intrinsic region i, when the diode is reverse polarized, is constant and equal to the maximum E_{max}. When a photon impinging on the open window of the device is absorbed, it creates an electron-hole pair. The high electric field accelerates the photo-generated carriers, raising them to a kinetic energy large enough to ionize the crystal lattice with the subsequent production of electron-hole pairs. The new pairs are accelerated and multiplied as well, originating a process named avalanche multiplication. If M is the total number of pairs produced by an initial photoelectron, the output current (I) is $I = MI_{ph}$, where I_{ph} is the total photocurrent produced by the absorption of an incident radiant power P.

In silicon, the charge carriers multiplication process is described by the ionization coefficient α and β of electrons and holes, defined as the number of new pairs generated for unit length by the carrier at a given electric field E.

Figure 1.12 shows the curves of α and β as a function of the electric field in silicon. As it is evident, starting from 10^5 V/cm, the ionization coefficient increases dramatically even for a small increment of the electric field, while for $E < 10^5$ V/cm ionization is negligible. It has also to be

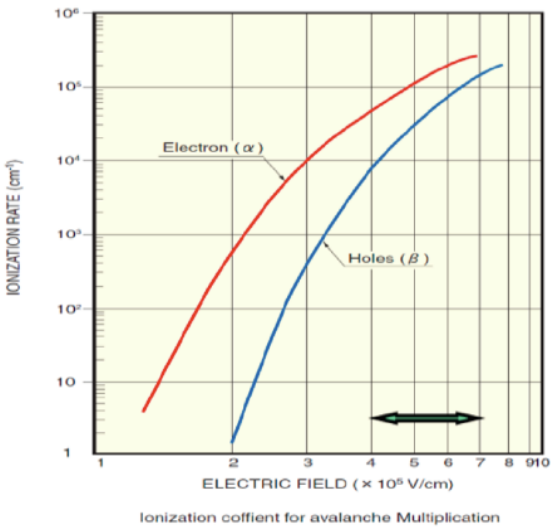

Figure 1.12 *Ionization coefficient of electron α and hole β as a function of the electric field for silicon.*

noted that in silicon the ionization of electrons is more efficient than for holes [28].

To evaluate the low frequency avalanche gain, M, of the avalanche photodiode, we assume a multiplication structure of length W, with a uniform field, as it is shown in Figure 1.13, so that α and β are constant. Let's assume that a primary electron is photogenerated at x=0 and that the amplified current is collected at x=L.

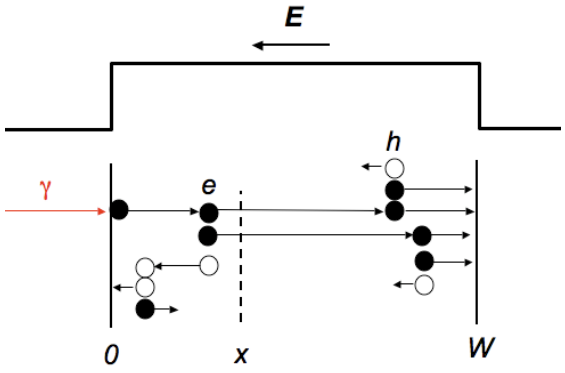

Figure 1.13 *Avalanche multiplication in a uniform electric field starting from a primary electron injected at x=0.*

If i_e and i_p are the electron and hole current at x, their increment along an elemental path dx is proportional to α and β and to the current itself:

$$\frac{di_e}{dx} = \alpha \cdot i_e + \beta \cdot i_h \,, \qquad \frac{di_h}{dx} = -\left(\alpha \cdot i_e + \beta \cdot i_h\right) \tag{1.3.1}$$

Solving Equations 1.3.1 with the boundary condition $i_e(0)=I_{ph}$, $i_e(L) = I = MI_{ph}$ and $i_h(L)=0$, we obtain the avalanche multiplication gain of the APD (M), as follow:

$$M = \frac{(\alpha-\beta)\exp\left[(\alpha-\beta)W\right]}{\alpha-\beta\exp\left[(\alpha-\beta)W\right]} \tag{1.3.2}$$

The gain M depends on the applied reverse voltage through the field dependence of the ionization coefficient α and β (see Figure 1.12). In silicon, as already discussed, the coefficient α>>β, thus leading to a simplified expression of Equation 1.3.2. In general, for α≠β, the gain always become infinite when $exp(\alpha-\beta)W=\alpha/\beta$. This condition can be obtained by incrementing the bias voltage over the breakdown voltage, V_{BD}, of the APD. An APD in

fact can be operated in two different modes: in linear mode and in Geiger mode. Common APDs are fabricated to work in linear mode. The multiplication gain, in this condition, is finite and can be tuned by varying the applied voltage. The mean number of multiplied carriers per photogenerated electron is constant and depends on the bias voltage. This mode of operation, illustrated in Figure 1.14 (a) and (c), is named linear since the number of collected carriers is proportional (by a factor *M*) to the number of absorbed photons.

When the applied bias voltage exceeds the breakdown voltage V_{BD}, the APD would enter into the Geiger mode operation. In this condition, the electric field across the junction is so high that the multiplication mechanism brutally increases and tends to infinite. Electrons and holes have enough energy to allow multiple ionizations in the crystals lattice. This

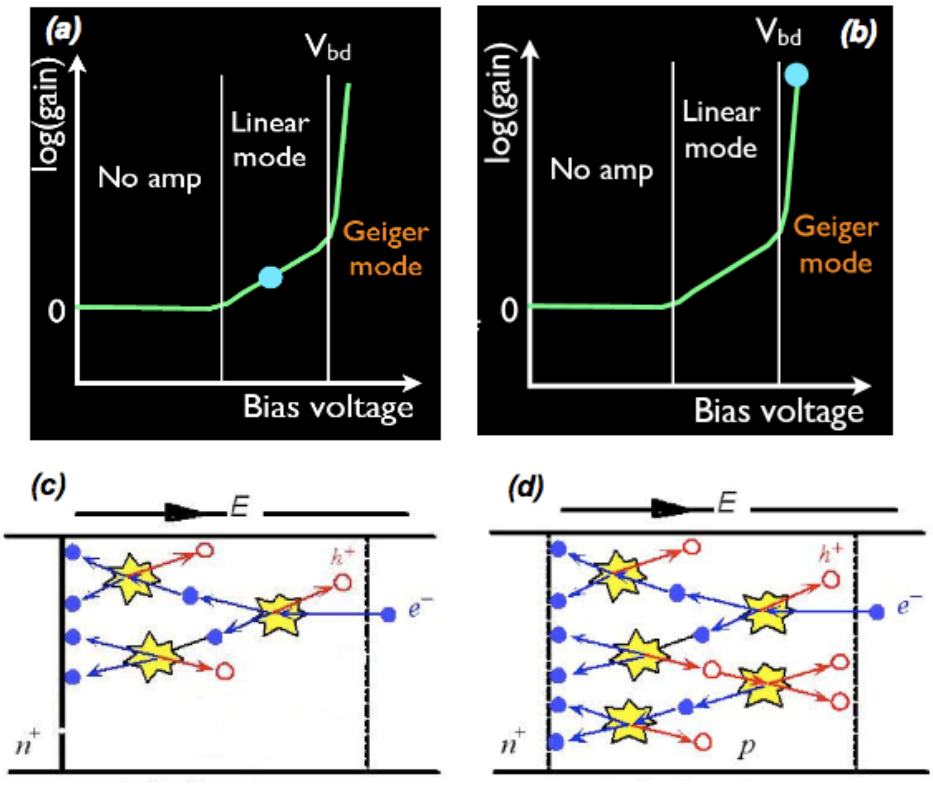

Figure 1.14. *Gain as function of the bias voltage for an APD working in linear mode (a) or in Geiger mode (b). The number of multiplied carriers by impact ionization when polarized above the V_{BD} is finite (c) while tends to infinite when polarized over the V_{BD} (d).*

process is self sustaining and the output current is in the order of the milli-Amperes [29]. The Geiger mode of operation is shown in Figure 1.14 (b) and (c).

If an APD operated in Geiger mode is connected to the bias voltage through a large resistance, R_Q, as illustrated in Figure 1.15 (a), the Geiger discharge would be quenched because the effective bias voltage at the APD terminals drops below V_{BD}. This is the basic structure of the single pixel of the Silicon Photomultiplier. In Figure 1.15 (b) it is shown its electrical scheme.

A circuit model, which emulates the evolution of the signal of a GM-APD in series with a quenching resistance, was developed in the1960s to describe the behavior of micro-plasma instabilities in silicon [16]. According to this model, the pre-breakdown state can be represented as a capacitance (the junction capacitance, C_D) in series with the quenching resistor. Referring to Figure 1.15 (b) this state corresponds to the switch in the OFF condition. In steady state, the capacitance is charged at $V_{BIAS}>V_{BD}$. When a carrier crosses the high-field region, there is a certain probability, known as turn-on probability, to trigger an avalanche circuit a voltage source V_{BD} with a series resistor R_S in parallel to the diode capacitance

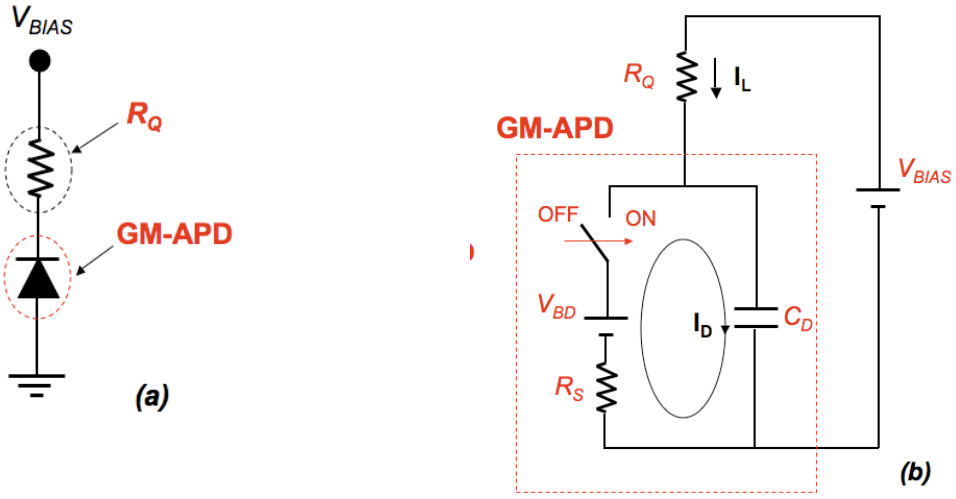

Figure 1.15. *(a) Schematic representation of the single pixel of the SiPM. (b) Equivalent circuit of the single pixels of the SiPM.*

discharge. If this happens, the new state of the system can be represented by adding to the (switch closed in Figure 1.15 (b)). R_S includes both the resistance of the neutral regions inside the silicon as well as the space charge resistance. C_D, originally charged at $V_{BIAS}>V_{BD}$, discharges through the series resistance down to the breakdown voltage with a time constant τ_D given by the product R_SC_D. R_S is estimated to be much smaller than R_Q. It should be noted that the discharge current is initially limited by the build up of the avalanche process which can take some hundreds of ps. Since R_S ranges from 100Ω to few kΩ, this time can be similar to τ_D for small diodes. As the voltage on C_D decreases, the current flowing through the quenching resistance, and as a consequence through the diode, tends to the asymptotic value of $(V_{BIAS}-V_{BD})/(R_Q+R_S)$. In this final phase, if R_Q is high enough, the diode current is so low that a statistical fluctuation brings the instantaneous number of carriers flowing through the high-field region to zero, thus quenching the avalanche. The capacitance charged at V_{BD}, starts recharging again to the bias voltage with a time constant C_DR_Q, and the device becomes ready to detect the arrival of a new photon. The typical output pulse, observed at R_Q, is schematically shown in Figure 1.16.

The single pixel of the SiPM works exactly as a SPAD with an external quenching resistor in series. The main limitation of a SPAD is that the output signal is the same regardless of the number of incoming photons, i.e. it works as a binary device. In order to overcome this limitation, multiple pixels can be connected in parallel to a single output. The structure so obtained is properly the Silicon Photomultiplier. A schematic circuit representation of a SiPM is shown in Figure 1.17.

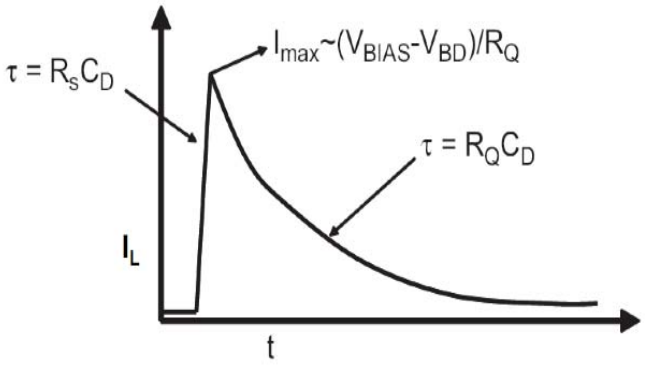

Figure 1.16. *Output pulse shape at the quenching resistance.*

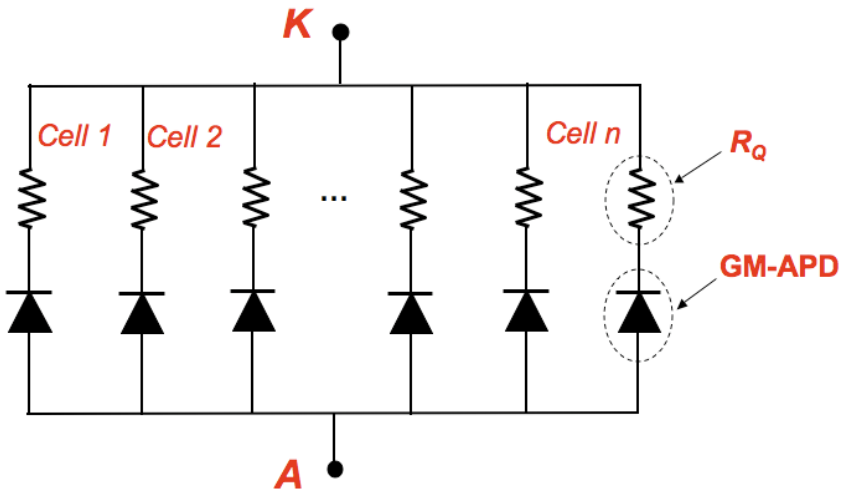

Figure 1.17. *Schematic circuit representation of a SiPM with n cells.*

Each pixel of a SiPM, when fired by a photon, works independently, producing the same output current pulse. When multiple photons hit the SiPM active area, the output signal is then the sum of each individual signal produced by the single pixels and, therefore, proportional to the number of cells hit by a photon. In this way the binary single device has been used to fabricate an analog device able to quantify the number of photons from a low intensity light source.

Using a simple linear amplifier, the output pulses of a SiPM can be observed on an oscilloscope or recorded with an Analogue to Digital Converter (ADC) with a fixed gate. In Figure 1.18 (a) a typical oscilloscope screenshot of the output pulse of a 100 pixel SiPM produced by Hamamatsu is shown; Figure 1.18 (b) shows the histogram, the photoelectron spectrum, of the ADC output in response to repeated fast pulses of a weak light incident on the SiPM sensitive area. The first peak in the spectrum, the pedestal, is a measure of the noise in the system (detector+electronics) and corresponds to the moments in which no pulses were recorded during the gate time. The second peak of the spectrum or the first photoelectron (1 p.e) corresponds to a single pixel fired, the third peak to two simultaneous

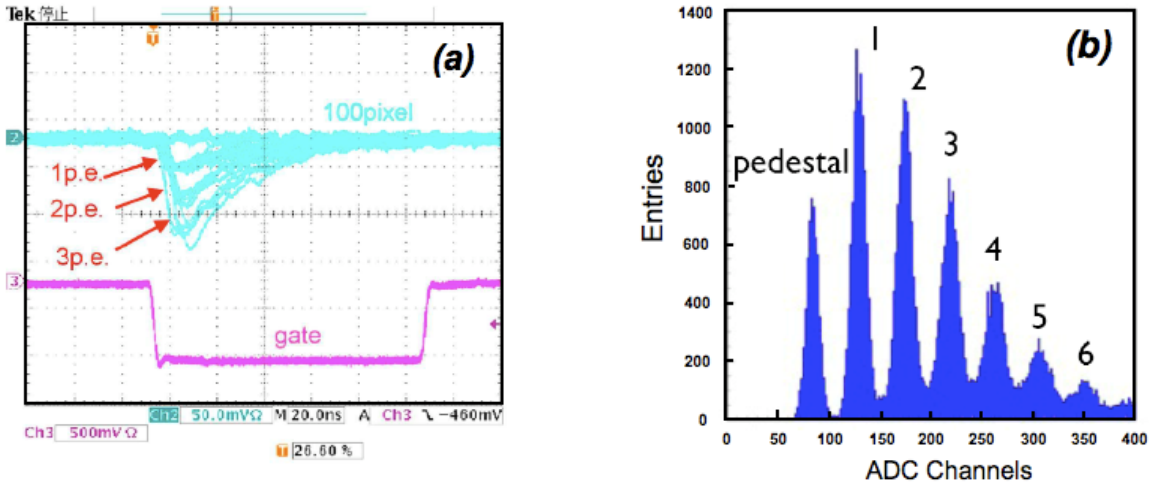

Figure 1.18. *(a) Oscilloscope screenshot of the signal produced by a SiPM with 100 pixels when illuminated by a low-photon flux. (b) Photoelectron spectrum of SiPM recorded with ADC readout as a response of a low-photon flux reprinted from [30].*

pixels fired (2 p.e) and so on. The straight separation between peaks and the good uniformity of the single peak demonstrates the good performance of the SiPM to detect a low photon flux.

§ 1.4 SiPM Properties

§ 1.4.1 Photon Detection Efficiency (PDE)

The Photon Detection Efficiency (*PDE*) of a SiPM is the statistical probability that an incident photon produces a Geiger pulse from one of the SiPM pixel i.e. the probability that a photon impinging on the sensor surface is detected. It is a function of the wavelength and of the bias voltage and it is defined as the product of three components:

$$PDE(\lambda,V) = QE(\lambda) \cdot P_t(V) \cdot \varepsilon_{GEO} \tag{1.4.1}$$

where QE is the quantum efficiency of the photosensitive area (see next section); P_t is the triggering probability i.e. the probability that a photo-generated carrier has to trigger an avalanche breakdown; ε_{GEO} is the geometric fill factor of the device i.e. the ratio of the photo-sensitive area to the total area of the sensor.

Like other silicon-based photodetectors, the silicon photomultiplier has a high quantum efficiency (*QE*), close to 100%, in the visible range. However, the overall photon detection efficiency for present state of the art SiPM is lower, due to other additional contribution apart from *QE*. All these factors have a relevant impact on the overall efficiency and must be

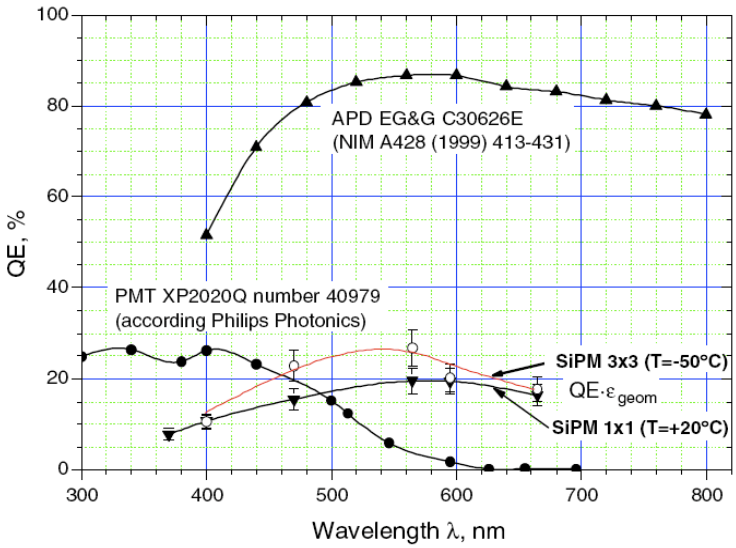

Figure 1.19. *(a) Comparison of PDE for SiPM, APD and PMT [31].*

carefully optimized to maximize the overall *PDE*. Figure 1.19 shows the PDE for present state of the art SiPMs in comparison with the typical QE of PMTs and APDs. The SiPM PDE is at the level of the PMT QE for blue light and larger in the yellow-red region.

§ 1.4.1.1 Quantum Efficiency (QE)

The quantum efficiency of the photosensitive area represents the probability for a photon, impinging on the active surface of the detector, to generate an electron-hole pair in the active thickness of the device that could be trigger an avalanche breakdown. Not all the incident photons produce an e-h pair since not all the incident photons are absorbed. Some of them simply fail to be absorbed because of the probabilistic nature of the absorption process. Others may be reflected at the surface of the detector, thus further reducing the quantum efficiency. Furthermore, some electron-hole pairs produced near the surface of the detector could quickly recombine due to the abundance of recombination centers close by and are therefore unable to trigger a breakdown.

The quantum efficiency, can therefore be expressed as:

$$QE = (1-R)e^{-\alpha w}(1-e^{-\alpha W}) \tag{1.4.2}$$

where R is the optical power reflectance at the surface, α is the silicon absorption coefficient (cm^{-1}), w is the depth from the Si/SiO_2 interface of the depleted region (cm) and W is the width of the depleted region (cm). The quantum efficiency is therefore an adimensional number ($0<\eta<1$) sometime expressed in percent.

The first term of Equation 1.4.2, (*1-R*), represents the effect of the reflection at the device surface. When light from a low refractive index medium, such as light in air (refraction index n_0=1), impinges on the surface of a medium having a high refractive index, like silicon (n_{Si}~ 3.5), a large portion of photons is reflected: 30% or more of the incident light is reflected causing a severe decrease of the detector *QE*. However, an anti-reflection coating on the

access window surface can appreciably reduce the reflection loss. This is obtained either with a single layer having a refraction index intermediate between n_0 and n_{Si}, or with a multiple layer of materials, as in the standard anti-reflection coating (ARC) treatment of optical surfaces. Usually, a silicon detector is covered with a thin silicon dioxide layer (SiO_2) having a refraction index n_{SiO2}~1.4, which has a considerable influence on the reflection of photons at the surface. Depending on the wavelength of photons, the reflected photons percentage can be reduced below 30%. Other materials, like Si_3N_4 (n_{Si3N4}~2), can improve the transmission of light at the interface. A single layer on the surface can greatly reduce the reflection loss, but a significantly improvement on the light transmission at the interface can be obtained with a suitable coating made of several thin layers having different refraction index (ARC), as it is in commercially available devices. The reflection loss can be decreased down to values below 10% over the entire visible spectrum [32].

The second term in Equation 1.4.2, $e^{-\alpha w}(1-e^{-\alpha W})$, represents the fraction of the photon absorbed in the depleted region of the device. The photon flux absorbed in the silicon bulk at a depth z from the surface decreases exponentially with the following relation:

$$I(x) = I_0 \exp(-\alpha z) \tag{1.4.3}$$

where I_0 is the incident flux entering the silicon that has passed the passivation top layer, α is the absorption coefficient of Si and z the depth from the Si interface. The carriers (electrons and holes) generated by the absorption of photons having enough energy ($h\nu > E_g$) decrease exponentially with the depth z, like the photons flux. The main contribution to the Geiger count of photons comes from the pairs generated in the depleted region of the device. Electrons and holes, created there, are accelerated by the high electrical field and can trigger, by impact ionization, the breakdown. Conversely, electrons and holes created by photon absorption at depths between the Si/SiO_2 interface and the boundary of the depleted region have a very short life time. In fact, usually the top layer of the photodiode is heavily doped, to reduce the series resistance and to ensure the electric field uniformity. This layer cannot be

depleted. Electrons and holes generated in that layer by photons absorption either recombine promptly or have to move by diffusion and can recombine with the abundant interface states.

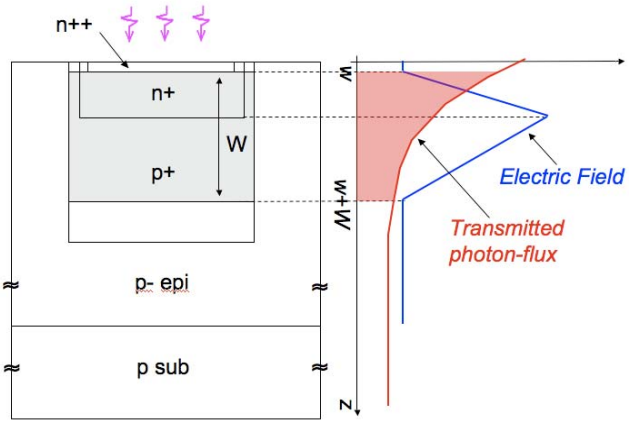

Figure 1.20: *Schematic structure of n on p SiPM with the electric field and the transmitted photon flux as a fuction of the depht from the Si/SiO$_2$ surface.*

The carrier pairs generated in the quasi-neutral region beneath the depleted region are not as useful as those created in the depleted region. A minority carrier, as for example an electron in a p region, has, in fact, a high probability to recombine with a majority carrier, a hole in a p region, thus erasing the photon detection event. Only the pairs created close to depleted region within a minority diffusion length, L_n, can move by diffusion to the high field region and then trigger an avalanche. This contribution is useful but much slower than that of carrier pairs generated into the depleted region since it entails the diffusion time constant of minority carriers $\tau_{Dn}=L_n^2/D_n$ with a characteristic time in the range of microseconds. At the time scale of the nanosecond, as in typical applications, shorter than that of diffusion motion, this contribution could be neglected. Therefore the fraction of charge pairs created to the absorbed photons and useful to trigger an avalanche is given by the fraction of photons dissipated in the range w - w+W, or:

$$\int_{w}^{w+W} \alpha e^{-\alpha z} dz = e^{-\alpha w} - e^{-\alpha(w+W)} = e^{-\alpha w}\left(1 - e^{-\alpha W}\right) \qquad (1.4.4)$$

In Figure 1.20 this situation is graphically represented.

The quantum efficiency of the active area can range from 80% to 90% depending on the wavelength but its maximum peak is relatively narrow with respect to the *QE* distribution of a PiN diode (see Figure 1.21) because the sensitive layer of silicon, i.e. the depleted region, is

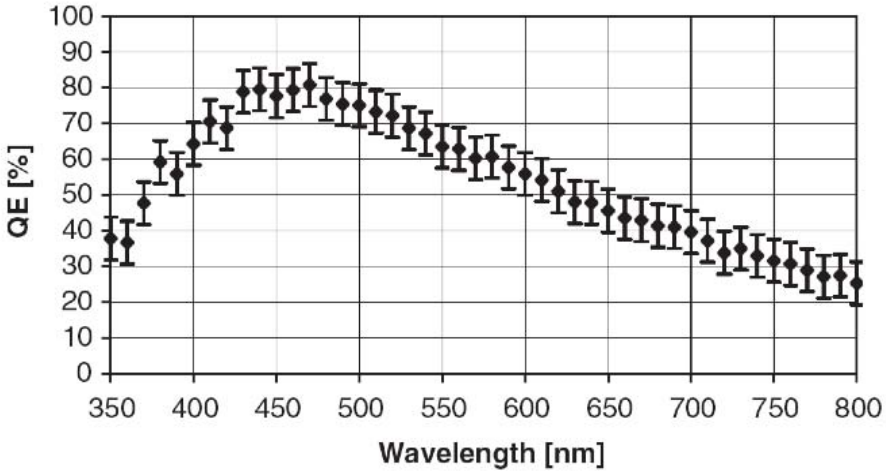

Figure 1.21: *Quantum efficiency of the active area as a function of the wavelength for Hamamatsu 0-50-2 with 400 cells [33].*

very thin (few micrometer). In the case show in Figure 1.21 the SiPM structure is a p-silicon on a n-substrate. The p layer is 0.5 μm on a 4 μm epitaxial layer [33].

§ 1.4.1.2 Triggering Probability (P_t)

A carrier that is moving trought a high-field region has a finite probability to trigger an avalanche breakdown. In the case of a photo-generation event, two carriers are created, an electron and a hole. In a high-field region the two carriers travel in the opposite direction and contribute together to the overall triggering probability that can be calculated from the following relation [34]:

$$P_t = P_e + P_h - P_e \cdot P_h \tag{1.4.4}$$

where P_e and P_h are the electron and hole initiation probability, respectively. These terms can be calculated as a function of the generation position by solving two differential equations involving the carrier ionization rate, as follow:

$$\frac{dP_e}{dx} = (1-P_e)\cdot\alpha_e\cdot(P_e+P_h-P_eP_h)$$
$$\frac{dP_h}{dx} = -(1-P_h)\cdot\alpha_h\cdot(P_e+P_h-P_eP_h) \qquad (1.4.5)\ .$$

$P_e(x)$ and $P_h(x)$ are the probability that an electron or a hole generated within the depleted volume of a pn junction, at the position x, triggers an avalanche breakdown, respectively. α_e and α_h are the ionization coefficients for electrons and holes, respectively.

The total triggering probability P_t can be calculated by integrating these equations with the boundary condition, in the case of a n^+p junction, that $P_e(0)=0$ and $P_h(W)=0$, where W is the width of the depletion region, that means that the probability to trigger an avalanche for a carrier coming from the high field region is zero. This calculation was performed by W. G. Oldaham [34] and the results for a n^+p junction are shown in Figure 1.22.

The overall probability is then a function of the position where the pair is generated (voltage above breakdown) applied to the junction. As a thumb rule, to maximize the triggering probability and

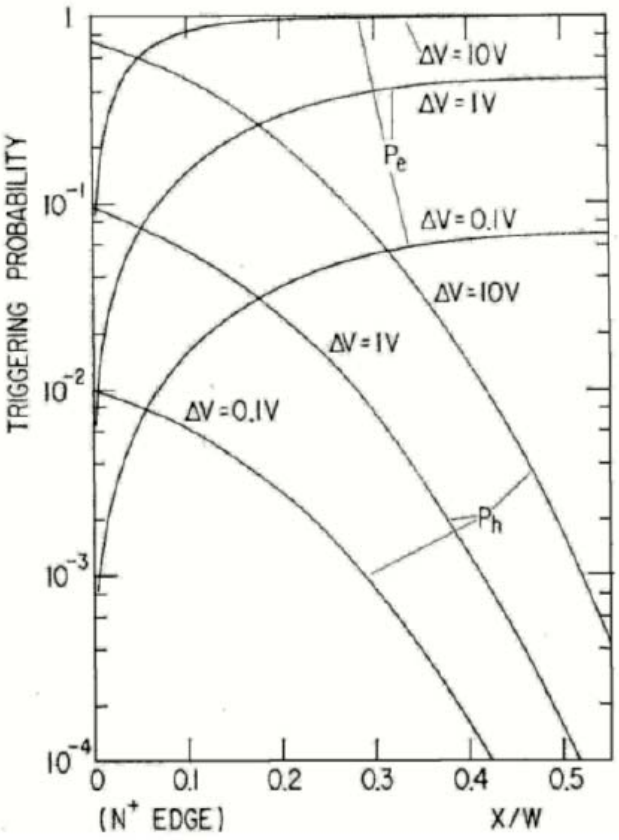

Figure 1.22: *Triggering probability for electron and hole, P_e and P_h respectively for a n^+p diode operating ΔV above breakdown as a function of starting position x [34].*

the *PDE,* the photogeneration should happen in the p side of the junction in order for the electron to pass the whole high field region and the bias voltage should be as high as possible.

It has to be noted that the triggering probability P_t depends on the shape of the electric field and, hence, on the doping profile. Special structures have been designed in order to maximize the triggering probability in such region were the creation of e-h pair is most probable (see for example [35]).

§ 1.4.1.3 Fill factor (ε_{GEO})

Since the silicon photomultiplier is a pixilated sensor, some room between the cells is required for the separation, for the individual quenching resistor, for metallization (it connects all the pixels to the same electrode) and, sometimes, to fabricate the optical trenches that provide the optical isolation between the cells to prevent crosstalk phenomena (discussed in the following paragraph). The total area of the detector is, then, different to the sensitive area.

The geometrical fill factor, ε_{GEO}, of a silicon photomultiplier is defined as the ratio of the photo-sensitive area (A_S) to the total area (A_{TOT}) of the device:

$$\varepsilon_{GEO} = \frac{A_S}{A_{TOT}}. \tag{1.4.6}$$

Since the *PDE* of a SiPM has a strong dependence on the geometrical fill factor, it needs to be accurately optimized and, as we will discuss, the optimization depends on the application. In Figure 1.23 are shown some layouts of the single pixel of a SiPM produced by different developers. The total area occupied by a single cell is delimited with a white line while the sensitive area with a blue line. The currently achieved geometric fill factor in suitable models is in the range from 30% to 60%. As a rule, a SiPM with smaller pixel area has a smaller fill factor, therefore the best filling (and obviously the best *PDE*) can be obtained with a small number of large cells. Unfortunately, a SiPM with few large cells has a reduced linear

dynamic compared to a SiPM with the same total area but with a larger number of small cells. Also a big cell has a greater dark noise than a smaller one, since the dark noise is proportional to the depleted volume of the cell. The increase in area of the cell is limited by the maximum noise allowed in the particular application for which the SiPM is developed. Moreover, a large cell has a longer recovery time, since the time needed to restore the charge accumulated in a pixel is ~ $4C_DR_Q$,where C_D is the capacitance of the cell and R_Q is the quenching resistance. The optimization of the fill factor, ε_{GEO}, of a SiPM is, therefore, a compromise between the maximization of the PDE and the other performances required for the specific application. In those applications where a small number of photons must be detected, as for example in High Energy Physics (HEP) or in Astrophysics experiments, a high PDE is required, hence the best choice is to use a SiPM with few large cells i.e. with the greatest fill factor.

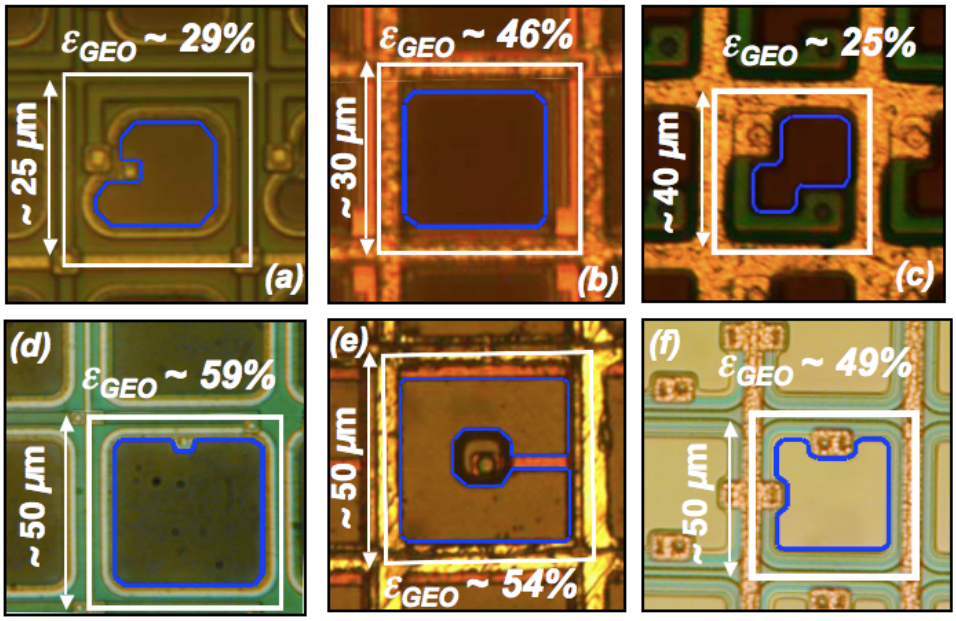

Figure 1.23: *Fill factor for different structure: (a) Hamamatsu 25um cell size. (b) SenSL 30um pixel. (c) FBK-Irst 40um cell sixe. (d) Hamamatsu 50 um cell sixe. (e) CPTA/Forimtek 50 um cell size. (f) ST Microelectronics 40 um cell size. The white line delimits the total area of the cell, the blue line the sensible area of the pixel.*

On the contrary, in those applications where a large number of photons must be detected and the linear dynamic response of the SiPM is therefore much important, a SiPM with a lower *PDE* but with a large number of small pixels, i.e. with a worse fill factor but a better speed, is preferred. An example of the last application is the Positron Emission Tomography (PET). In PET the SiPM is coupled with a Lutetium Oxyorthosilicate (LSO) crystal that convert the *511 keV γ-ray* emitted by the electron-positron annihilation into ~15000 photons in the blue spectra. At the end face of the crystal, where the SiPM is mounted, thousands of photons must be collected. In order to avoid a saturation effect and to improve device speed, the number of cells into the SiPM needs to be large and, in turn, the cells must be small.

§ 1.4.2 Gain

One of the most important features of the SiPM is its intrinsic and stable high gain. The gain instability, observed in normal APDs, is due to the intrinsic statistical fluctuation of the avalanche multiplication process itself. On the contrary the SiPM, being operated in Geiger Mode, i.e. with M theoretically infinite, has a very stable gain. The stability of the gain is obtained thanks to the quenching mechanism provided by the series resistance. The suppression of the avalanche current by the negative feedback on the electric field trough the diode junction stabilizes the oscillation of the gain.

The gain of the SiPM is defined as the ratio of the output charge Q_{tot} produced by n_{ph} detected photons to the charge of an electron q:

$$G = \frac{Q_{TOT}}{n_{ph} \cdot q} \tag{1.4.7}$$

Assuming that on average one photon produce the avalanche of one pixel, the gain is then given, referring to Figure 1.16, by:

$$G = \frac{Q_{pix}}{q} = \int \frac{I_L}{q} dt \approx C_D \frac{(V_{BIAS} - V_{BD})}{q} \qquad (1.4.8)$$

where C_D is the diode capacitance and V_{BIAS}-V_{BD} is the applied overvoltage. Measuring the charge delivered by one pixel is then possible to measure the gain of the SiPM. Since C_D is typically in the range of 10÷100 fF and V_{BIAS}-V_{BD} is in the range of a few volts, a high gain, typically in the range of 10^5÷10^7, is obtained. The charge delivered by one pixel is commonly measured from the separation of peaks in the single photoelectron spectrum (Figure 1.18 (b)) providing the correct ADC channel to charge conversion.

Equation (1.4.8) provides a linear dependence of the gain versus the applied voltage and is the most common definition of the gain [30,31,33,35]. However, it was found that light emitted during the pixel breakdown penetrated adjacent pixels due to optical cross-talk (as discussed in the following paragraph *1.4.3.3*) and fired these pixels. Thus the average number of pixels fired by a primary photoelectron is typically more than one. Then the real SiPM gain is equal to the charge Q_{PIX} multiplied by the average number of fired pixels to the

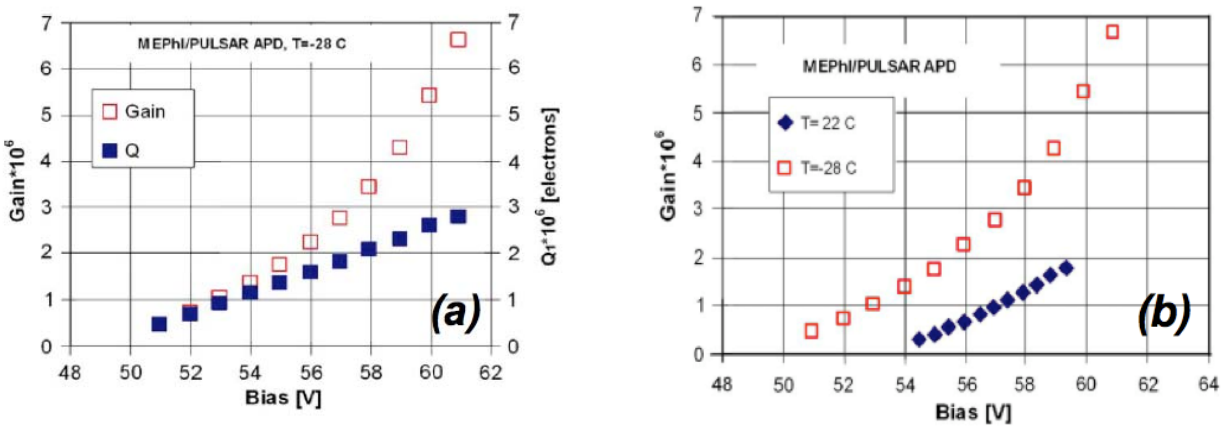

Figure 1.24: *(a) Gain of a Mephi/Pulsar SiPM as a function of the bias voltage measured from the charge delivered by one pixel, denoted as Q, and as the total charge, including the cross-talk effect, denoted as G. (b) Gain G as a function voltage at different temperature reprinted from [36].*

electron charge. In Figure 1.24 (a) are compared the gain obtained measuring the charge delivered by one pixel (blue squares) and the real Gain (red squares) produced by a detected photons as described in [36].

The SiPM gain is also temperature dependent. As the temperature rise, the lattice vibrations in the crystal become stronger. This increases the probability that carriers may strike the crystal before the accelerated carrier energy has become large enough, and make it difficult for ionization to occur. Then, as the temperature rises, is required more energy from the electric field, i.e. a greater V_{BIAS}, to produces an avalanche discharge as shown in Figure 1.24 (b).

§ 1.4.3 Noise

An avalanche breakdown in a SiPM can be triggered by a photo-generated carrier, when photons strike the detector, or by any free carrier generated inside, or near, the depleted region, even in dark condition. The pulses generated by these two processes are indistinguishable each other. The last one represents the intrinsic noise of the silicon photomultiplier and the frequency of such noise can be determined by counting the pulses occurring per second when the SiPM is in dark condition. The frequency of the noise is commonly named *Dark Counts* of the SiPM. The Dark Counts of a SiPM are due to the contribution of three components: the primary dark counts, the after pulsing and the cross talk.

A typical Dark Counts rate as a function of the threshold level of the readout electronics, normalized to the equivalent number of photo-electrons (p.e.), is shown in Figure 1.25 for a SiPM produced by Hamamatsu [37]. The rate of the dark pulses counted with a certain threshold corresponds to the number of pulses per second that have an amplitude larger than the threshold itself. The typical dark counts at room temperature (25°C) measured at a threshold of 0.5 p.e. range between 100 kHz to several Mhz per mm^2. The count rate

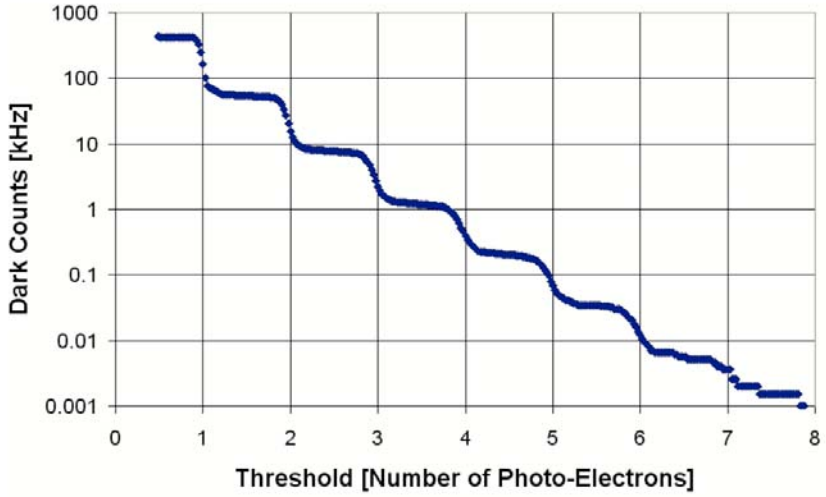

Figure 1.25: *Dark count rate as a function of the threshold level of the read out electronics, normalized to the equivalent number of the photo-electrons, of a MPPC S10362-11-050C produced by Hamamatsu (1mm^2 area) operated at a gain of 7.5·10^5 [37].*

decreases considerably increasing the threshold of the readout electronics. Each increase of the threshold by the equivalent of 1 p.e. typically reduces the noise rate by almost one order of magnitude (Figure 1.25). Dark events with amplitude larger than 1 p.e are mainly due to the crosstalk phenomenon as discussed later.

§ 1.4.3.1 Primary dark count

The primary dark count is mainly due to thermally generated e-h pairs. It is the same phenomenon that causes the reverse current in ordinary p–n junction diodes, well interpreted by the Shockley–Read–Hall (SRH) theory [38-39]. In particular, it is well known that in silicon p–n junctions the reverse current is dominated by the generation in the depletion layer, whereas the contribution due the diffusion of minority carriers from the neutral regions to the junction is much lower (see Appendix B). According to the SRH theory, electron–hole pairs are generated in sequence through generation–recombination (G–R) centers, that are local levels at about mid-gap (Figure 1.26 (a)). Depending on the electric field profile of the device, it would be necessary to include the contributions due to the Poole–Frenkel effect and to trap-

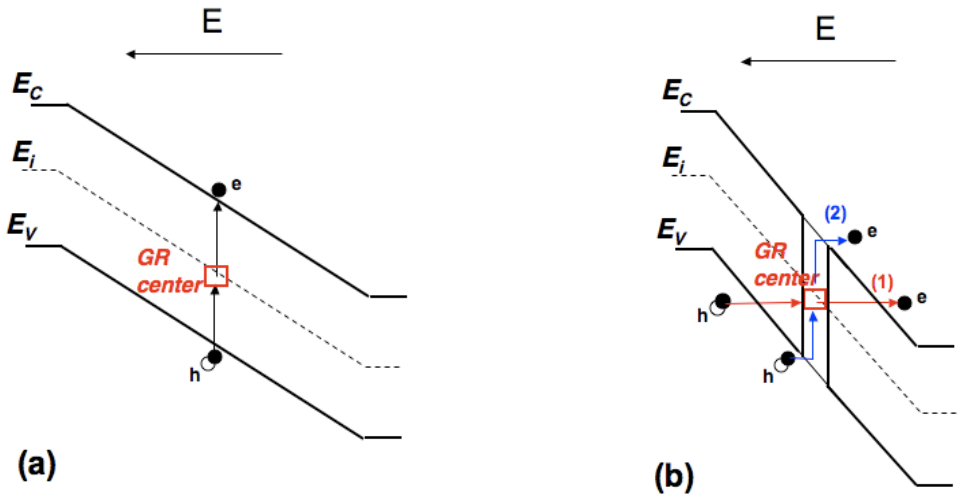

Figure 1.26: *(a) Thermally SHR generation of electron-hole pairs. (b) Field assisted generation: (1) TAT and (2) SHR generation with Poole-Frenkel effect.*

assisted tunneling (TAT) (Figure 1.26 (b)) [40]. The effect of TAT is to increase the emission rate of a G–R center. Similar considerations can be made for the Poole–Frenkel effect. In SiPM devices where the maximum electric field E is well below a critical value, these effects are estimated to be negligible.

The primary dark counts can be influenced by the SiPM production process aiming to minimize the number of generation-recombination centers (GR center), the impurity and crystal defects, wich give rise to the Shackley-Read-Hall effects.

§ 1.4.3.2. Afterpulsing

The afterpulsing is a detrimental component of the noise in a SiPM. In the silicon volume where the breakdown avalanche takes place, a high temperature (~1000 °C) plasma is created. The generated free carriers can be trapped by deep level impurity states present in the depleted volume of the junction [41]. These trapped carriers may be released after a certain time Δt, as illustrated in Figure 1.27 (a), causing a delayed avalanche in the same pixel where breakdown occurred, i.e. an *afterpulse* (Figure 1.27 (b)).

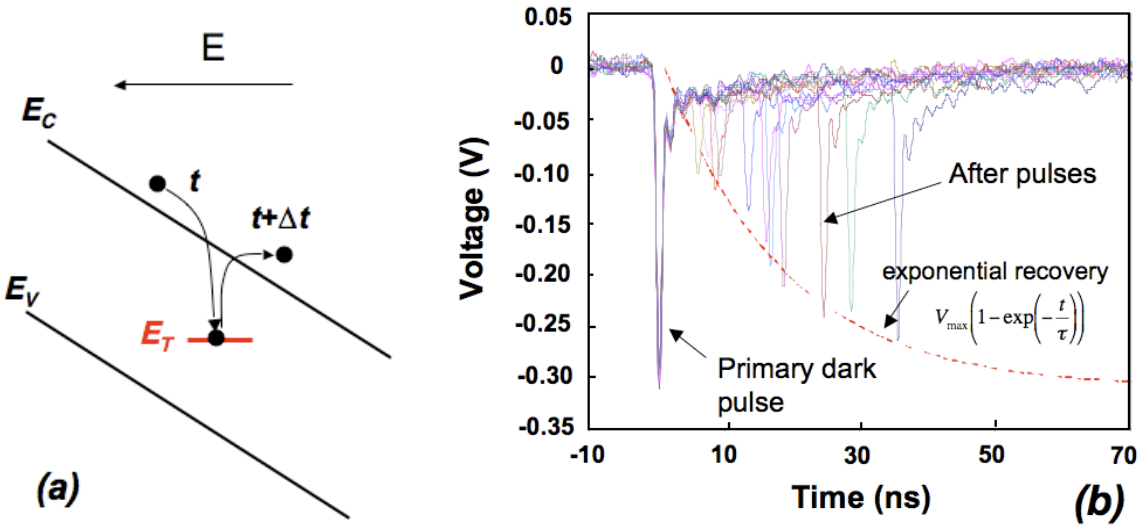

Figure 1.27: *(a) Trapping and delayed releasing of a free carrier produced during an avalanche breakdown by a deep level impurity in the depleted volume of the junction. (b) Primary pulse and afterpulses reprinted from [42]*

The typical timescale at room temperature is in a time ranging from 10 to 100 ns depending on the energy level of the impurity.

The afterpulsing probability P_{ap} depends on both the voltage and the temperature. An increment of the bias voltage produces an increase in the P_{ap} since the gain enhancement produces more electrons per avalanche, the triggering probability P_t increases and since the emissivity increases due to the Poole-Frenkel effect. Operations at low temperature elongate the delayed release reducing the afterpulsing probability.

Afterpulses can strongly enhance the total dark count rate of a SiPM. Moreover, since they are related to the primary avalanche, which previously filled the traps, they are not randomly distributed, as a white noise, but are correlated. Its effect is then troublesome in any photon correlation experiment.

A simple strategy to reduce the afterpulsing contribution is to increase the recovery time of the pixels with a larger quenching resistance, in order to have enough time to depopulate the filled traps. Afterpulses occurring during the recovery time have amplitudes lower then 1

p.e (see Figure 1.27 (b)). If the threshold level of the readout electronic is opportunely chosen the extra counts due to afterpulses can be drastically reduced.

§ 1.4.3.3. Cross-talk

The cross-talk is a noise contribution common in all pixelated devices. A pulse current produced by a pixel, due to a photon detection event or to a primary dark noise event, can induce one or more adjacent pixels to experience the avalanche breakdown. The corresponding output pulse current of the SiPM has then an amplitude peak proportional to the number of involved pixels in the single photo-detection and in the correlated cross-talk phenomena. This noise contribution is detrimental in all the applications where the single photon resolution is required.

The cross-talk noise has two different physical origins: optical and electrical.

The optical cross-talk is due to the photons generation by radiative emission from the hot carriers produced during an avalanche discharge. In an avalanche multiplication process, on average 3 photons, with energy higher than the silicon band gap (1.14eV), are emitted every 10^5 carriers [43]. These emitted photons can travel to a neighboring pixel and trigger a

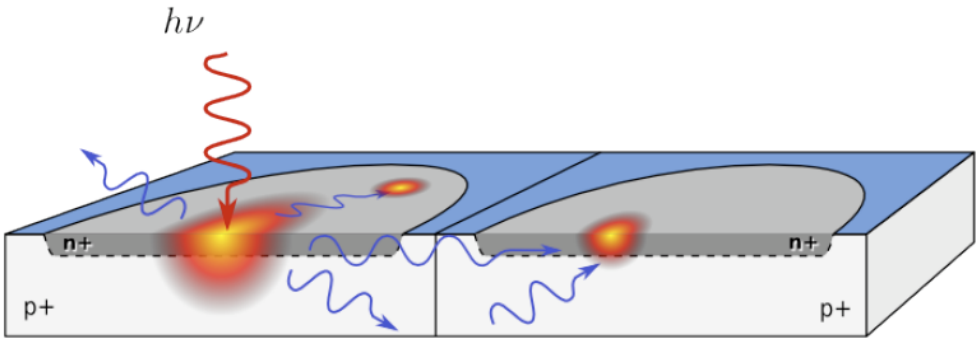

Figure 1.28: *Optical crosstalk between neighboring pixels. Secondary photons emitted during an avalanche discharge can reach adjacent pixels and trigger there an avalanche breakdown.*

breakdown there, as illustrated in Figure 1.28, as any external photon. Several models were suggested in the past to explain the light emission as, for example, the breemsstralhung and a multi-mechanism scenario, including indirect and direct inter-band and intra-band transitions [43-47]. Particularly critical are the emitted photons in the spectral range between 850 nm and 1100 nm, because the photons with higher energy i.e. lower wavelength are all absorbed within the same cell and the infrared photons with wavelength larger than 1100 nm travel over long distances without being absorbed [48].

The electrical cross-talk can occur when carriers, generated during the avalanche breakdown in a cell, can cross the junction reaching a close pixel. Traveling along the epitaxial layer, common to all pixels, these carriers can reach the neighboring pixels and triggering there a new avalanche breakdown [49-50].

Some strategies have been studied to reduce the cross-talk between neighboring pixels. The first is to increment the distance between adjacent cells. This approach has a detrimental effect on the geometrical fill factor of the SiPM and a consequent reduction in the PDE is. The second strategy consists in fabricating grooves, filled with optical absorbing material, all around each cell. These grooves, commonly named trenches, prevent from optical and electrical coupling between cells. The reduction of the geometrical fill factor with

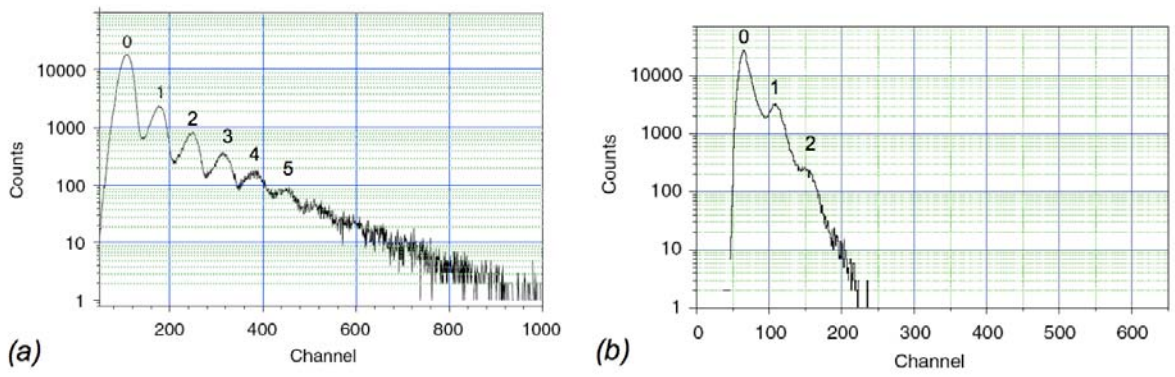

Figure 1.29: *Crosstalk for 1.1 mm^2 SiPM produced by MEPHI/Pulsar, measured as the pulse height distribution (a) without trenches and (b) with trenches. Modified from [51].*

such design is mild while the effect on the cross-talk noise is considerable, as shown in Figure 1.29 (a). Data of Figure 1.29 (b) evidence how the pulse height distribution is modified by the trenche presence: events with amplitude larger than the single pixel pulse amplitude are significantly attenuated.

The crosstalk noise has a strong dependence on the over-voltage and consequently on the gain, but it does not strongly depend on temperature. The increase of the bias voltage above the breakdown value is reflected in an increase of the cross-talk probability. A typical of the SiPM at 1.5 p.e. over the dark count at 0.5 p.e., for different temperatures is shown in Figure 1.30, for an SiPM produced by Hamamatsu with 1 mm^2 of sensible area.

over-voltage dependence of the cross-talk probability, measured as the ratio of the dark counts

A reduction of the crosstalk noise for the same cell area and fill factor can only be achieved by reducing the cell capacitance, i.e. increasing the width of the depleted volume, albeit with an increase of the total dark counts.

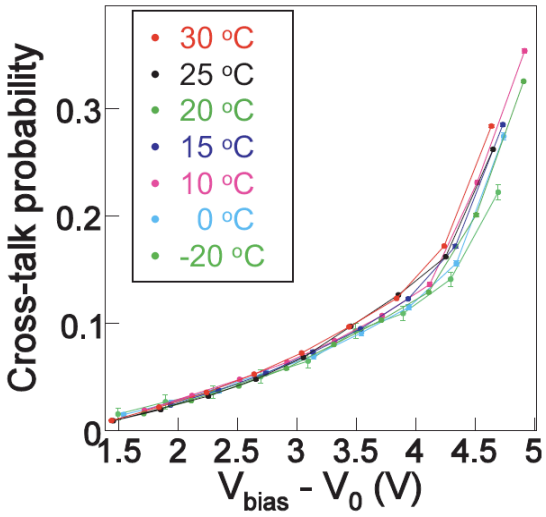

Figure 1.30: *Cross-talk probability measured as the ratio of the dark counts at 1.5 p.e over the dark counts at o.5 p.e for an the MPPC S1036-33-050C for different temperature. Cross-talk probability is strongly dependent on the over-voltage. Taken from[52].*

§ 1.4.4 Timing

The single photon timing resolution (SPTR) of a SiPM is the statistical distribution of the delays from the true arrival time of the photons at the device to the actual detection time marked by electrical output pulse of the detector. Since the active layer of a SiPM is very thin (typical 2÷4 μm) and the process of the breakdown development is fast, the SiPM demonstrates a very good timing property (typical 100÷400 ps).

A typical single photon timing resolution of a SiPM (Figure 1.31) presents a main peak due to the photon absorbed in the depleted region and a slow tail due to photon absorbed in the neutral region [53].

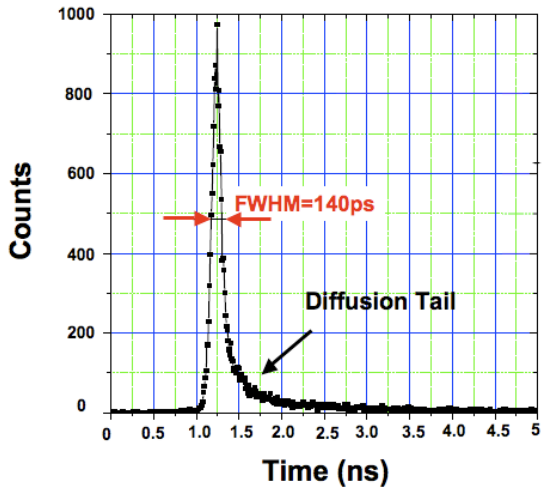

Figure 1.31: *Single photon timing resolution for a Mephi/Pulsar SiPM 1×1 mm² area and 576 pixels reprinted from [54].*

The main peak follows a Gaussian distribution and its full width at half maximum (FWHM) gives the time resolution of the SiPM (sometime the resolution time is quoted as the standard deviation σ of the Gaussian distribution). It is related to the fluctuation in the avalanche build up time and is improved by increasing the bias voltage applied to the device (i.e. the electric field applied to the junction). The avalanche development is due to a vertical build-up component and to a lateral spreading [55]. The vertical avalanche build-up is too fast and gives a small contribution to the overall avalanche fluctuation. The lateral spreading is the mainly responsible of the avalanche build-up fluctuation. It's due to the lateral diffusion of the multiplication process [56] and in minor via to the lateral propagation of the avalanche due to photon generation

and absorption in the same pixel (a phenomena similar to the optical cross talk) [57-58].

The slow tail of the SPTR is due to minority carriers, photo-generated, in the neutral region beneath the junction, that succeed in reaching the depleted layer by diffusion [59]. Accurate design of the neutral region is needed in order to reduce this effect. In the worst case the diffusion of the minority photo-generated carrier can degrade seriously the timing performance of the SiPM.

§ 1.4.5 Dynamic range

The dynamic range of a SiPM is defined as the maximum number of simultaneous photons that can be detected Due to the finite number of pixels, the dynamic range of the silicon photomultiplier is limited. The number of simultaneous pixels fired by the incoming photons depends on the total number of pixels of the detector according to the following expression [60]:

$$N_{fired\ pixels} = N_{pix} \cdot \left(1 - e^{\frac{Nph \cdot PDE}{N_{pix}}} \right) \tag{1.4.9}$$

where $N_{fired\ pixels}$ is the number of pixels that experience an avalanche breakdown, N_{pix} is the total number of pixels of the SiPM, *PDE* is the photon detection efficiency and N_{ph} is the number of incoming photons.

The response of the SiPM to a photons flux is linear for $N_{ph} \cdot PDE / N_{pix} << 1$, i.e. if the average number of photon per one pixel is small enough. In fact if more than one photon impinges at the same time in one cell, they produce a signal equal to the one of one photon. When the number of impinging photons times the *PDE* exceeds 50% of available pixels, the deviation from linearity is more than 10%. The finite number of the pixels results in the saturation of the SiPM signal with increasing light as shown in Figure 1.32.

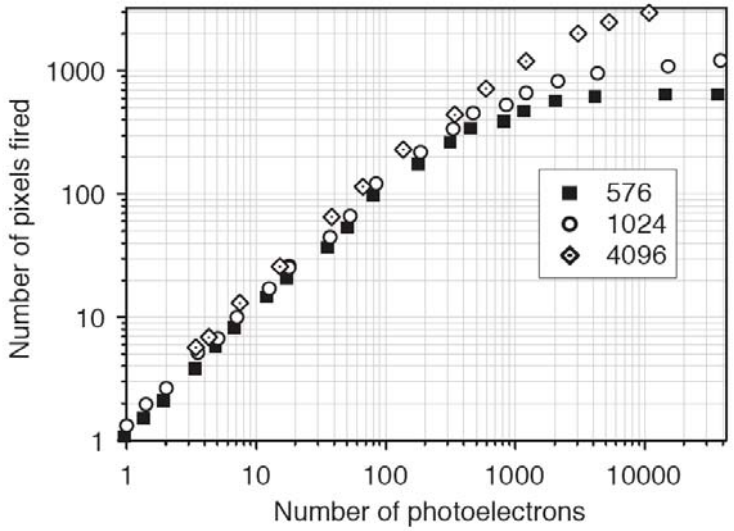

Figure 1.32: *Response of SiPMs with different number of pixels to a 40ps laser light [61]. The SiPM with a greater number of pixels has a larger linear response extension.*

§ 1.5 Applications

The SiPM can be used in many applications where extremely weak light signal, at the level of photon counting, must be detected. It provides all the performances needed in photon counting, as the high gain at low bias voltage, high photon detection efficiency, good time resolution, high count rate and a large spectral response. In addition, since the SiPM is a semiconductor device, it is not affected by mechanical stress and no additional cooling is required (photon counting can be performed at room temperature). These characteristics make the SiPM the perfect candidate to replace the traditional existing detectors used in photon counting and open the door to a wider scenario of future applications. Moreover, its insensivity to external magnetic field is of great interest in those applications where it is required to work in a magnetic environment.

The following list is only a brief overview of some fields of application and is far from being a complete one. Some fields have been intensively investigated for a long time while

others are nowadays unexplored. Moreover, since the SiPM is a relatively new device, most realized detectors using SiPMs are only experimental prototypes.

The SiPM is the ideal device in many field of application like fluorescence analysis, fluorescence lifetime measurement, bioluminescence analysis, biological flow cytometry, single molecular detection, DNA sequencing. Nowadays only few results are published in those fields [62-63], but some producers like Hamamatsu Photonique, Photonique SA, SensL, Newport and others, have recently commercialized compact modules that contain an SiPM and the suitable front end electronic for processing the SiPM output signal. This module can be directly connected to a personal computer or to standard electronic equipments like an oscilloscope as to provide a friendly interface for users. Several results are then expected in such fields of application in the next years.

In nuclear particle physics, high energy physics and astroparticle physics experiment, SiPM have been extensively used. The planar nature of SiPMs allow them to be closely coupled to a suitable scintillator materials, or in a system composed of a scintillator and a wavelength shifting (WLS) for particle detection (see Figure 1.33 (a)). When struck by anincoming particle or high energy electromagnetic radiation, scintillator materials absorb the energy and re-emit it in the form of a weak flash of light, typically in the visible spectrum. This weak flash of light is then detected by the SiPM. SiPMs are therefore suitable in particle physics experiments and a wide range of medical imaging equipment, for example in Positron Emission Tomography (PET) scanners.

The CALICE (Calorimeter for ILC, being ILC the International Linear Collider) collaboration, has started various R&D projects to design a calorimeter optimized for particle flow, to use in the International Linear Collider detector (ILC) [64]. Since high granularity on a large scale can be obtained with a scintillating tiles read out with a wavelength-shifting fiber and a SiPM and since the ILC detector has to operate in a 4 Tesla magnetic field, conventional PMT cannot be used. A large scale prototype equipped with SiPMs has been successfully designed, constructed and tested (see Figure 1.33 (b)).

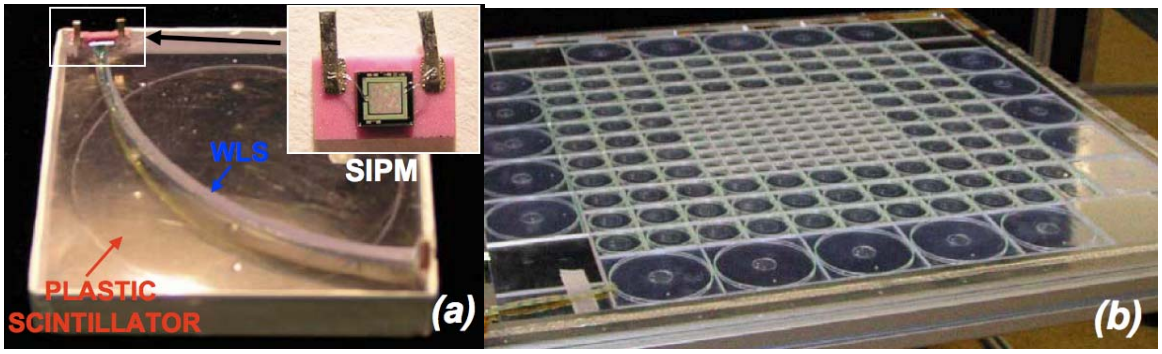

***Figure 1.33**: (a) System composed of a plastic scintillator, a wavelength-scinfting fiber and a SiPM red-out for CALICE calorimeter detector at ILC. (b)CALICE calorimiter prototypes[61].*

A similar concept detector, with plastic scintillator, wavelength shifter and SiPMs read-out, is the so called "*Near neutrino Detector of Tokai-to-Kamioka experiment*". The installation is started in January 2009 and 6000 SiPMs will be used [65].

It has been shown that Cherenkov light produced in air shower, wich are initiated by high energetic cosmic rays, can be detected by SiPM with high sensitivity [66]. A full-sized prototype camera for an imaging air shower Cherenkov telescope with SiPM (instead of traditional PMTs) is currently under construction [67]. An improved in sensitivity by a factor 2-3 is expected compared with traditional PMTs.

Finally, one of the most intriguing applications is the PET. It is a molecular imaging technique that produces three-dimensional images of functional processes in the body, e.g. the uptake of glucose that fuels metabolic activity. The PET system detects pairs of gamma rays (high energy electromagnetic radiation) originating from a radioactive tracer, a small amount of which is injected into the patient prior to the scan. To image metabolic activity, PET typically uses a radioactive derivative of glucose called fluorodeoxyglucose (FDG). This compound mimics the behavior of glucose in the body and can be detected by a PET scanner. When the radioactive tracer decays, it emits a positron e+ that, after a few millimeters, recombines with an e- of the absorbing material. This process of annihilation produces two

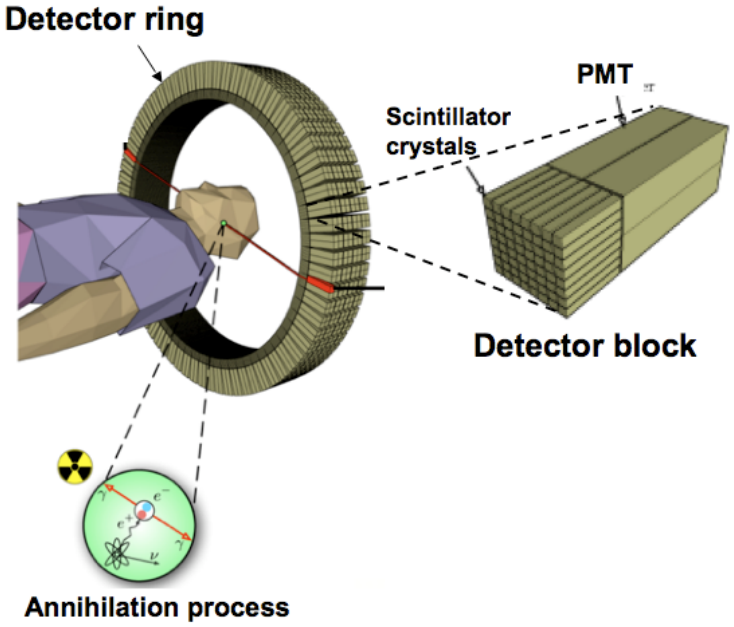

***Figure 1.34**: Conevntional PET scanner. The annihilation of positron emitted from radioactive tracer generates two photon with opposite direction at 511keV. The basic block of the detector ring is composed of a scintillator crystal and a photomultiplier.*

photons with energy of 511 keV with opposite direction. The emitted photon can be detected simultaneously by a PET scanners and a 3D images of tissues can be reconstructed.

Conventional PET scanner use PMTs as photodetector. The main drawbacks to use standard PMT are: the large physical dimension of a single PMT, that reduces the system sensitivity to the photon spatial position and the need to use many PMT to fabricate the detector ring (see Figure 1.34) that forms the instrument, with large costs involved. The use of SiPM coupled with a scintillator material would solve those issues. First results have been demonstrated the feasibility [60,68-70] hence the main PET producers (Siemens, Philips) already started research projects to use SiPM.

Chapter 2

Single Pixels:
Electrical and Optical Characterization

The single pixel is the basic building element of a Silicon Photomultiplier. In this chapter the fabrication details and the structural characterization of the pixels are reported All the devices described hereafter were fabricated by STMicroelectronics in Catania. Basic structural characterization was performed using scanning electron microscopy (SEM) and transmission electron microscopy (TEM) images and spreading resistance profiling (SRP). Simulations of electrical behavior, performed using a commercial simulator by Silvaco, allowed designers to optimize the structure in order to have a diode that breaks through an avalanche process.

Since the performances of the whole detector are closely related to the physics characteristics of its single components, a detailed experimental characterization was performed. It consisted of I-V measurement both in forward and reverse polarization in dark and under light illumination and as a function of the temperature. The devices gain has been determined using two independent characterization methods, named "Transient current Measurement Mode" and "Photocurrent measurement mode", since they use the dark current and the photocurrent, respectively, for the gain determination. The careful analysis of the data allow us to propose a physical model to explain both the temperature and voltage behavior in dark of the single pixels in the photon-detection bias voltage range. In particular, the model allowed us to conclude that the dark current is due to two concomitant processes: the

diffusion of electron from the p-bulk dominating at room temperatures and the thermal generation from midgap defects dominating at lower temperatures. The model, proposed in this chapter, well fits all the data collected.

§ 2.1 Single Pixels Fabrication Details

The single pixel described in this work has been produced by the R&D Sensor Team STMicroelectronics in Catania. It has a square shape with a 40×40 μm^2 active area. The top view of its layout is shown in Figure 2.1, where it is possible to identify the anode and the cathode contacts of the p-n junction, the quenching resistance surrounding the active cell area, and the trenches fabricated all around. In the whole detector the cathode bus, connected to the cathode of each p-n junction through the quenching resistance, and the anode bus realize the contacts between cells.

The pixel is fabricated in the standard silicon planar technologies [71,72] starting from a Float Zone (FZ) low doped n-type substrate with a resistivity of ~ $4 \cdot 10^3$ Ω·cm. The FZ n-type substrate has a very low impurity atoms concentration (the residual metal atoms impurity concentration is lower than 10^{12} cm^{-3} and the oxygen is present with a concentration lower than $5 \cdot 10^{16}$ cm^{-3}). A 2 µm p+ epitaxial layer doped with $9 \cdot 10^{16}$ cm^{-3} Boron atoms is grown on the substrate. This highly doped layer forms a low resistance path for carriers moving from

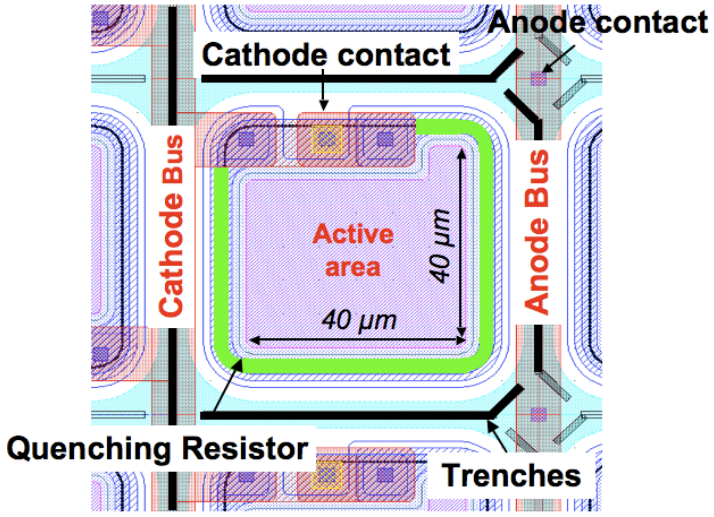

Figure 2.1: *Layout of a single pixel produced by ST Microelectronics in 2009.*

the active region to the distant anode contact and blocks the diffusion of carriers from the n substrate to the active volume of the p-n junction.

A 5 μm p epitaxial layer, with a Boron concentration of ~10^{15} cm^{-3}, is then grown on the p+ layer. In this layer is formed the p-n junction. Before the definition of the active region the p++ sinkers are created by a high boron implantation in order to reduce the contact resistance and provide a low resistance path to the avalanche current. An n-type ring, surrounding the active volume, is formed by Arsenic implantation in order to prevent later breakdown. This n-ring ensures a breakdown voltage higher than 60V. Then an implanted p+ layer realizes an enrichment region that defines the active area of the pixel and the breakdown voltage of the junction (~ 28V). The thin cathode is given by an n++ thin polysilicon layer doped *in-situ* with arsenic. A Rapid Thermal Anneal process allows the diffusion of the arsenic atoms in the p+ layer forming a shallow arsenic profile of ~0.2μm. The p-n junction or the active region of the pixel is so realized. The quenching resistor, made from low-doped polysilicon, is integrated on the cathode of the cell itself. Thin optical trenches filled with oxide and metal surround the pixel active area. This step has been included in the process flow of the device in order to reduce electro-optical coupling effects (crosstalk) between adjacent cells in the forthcoming production of large-area SiPM.

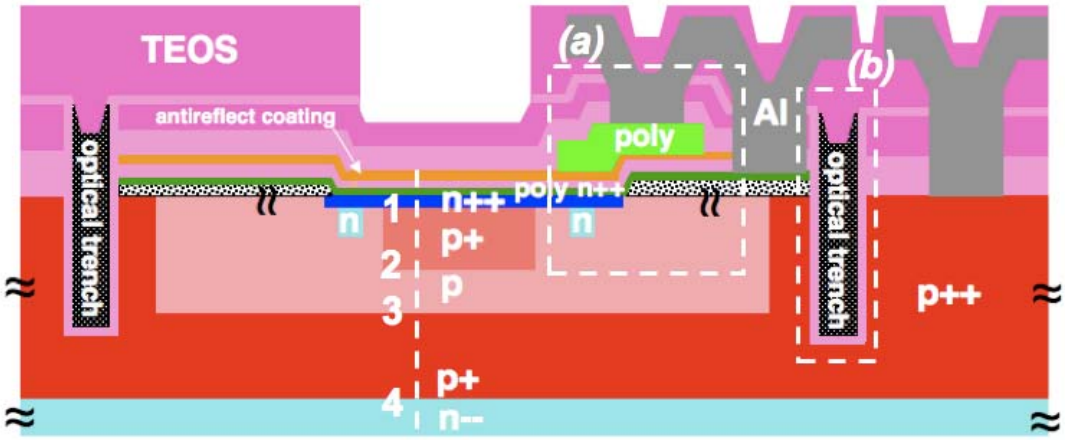

Figure 2.2: *Schematic cross-section of a single pixel produced by ST Microelectronics.*

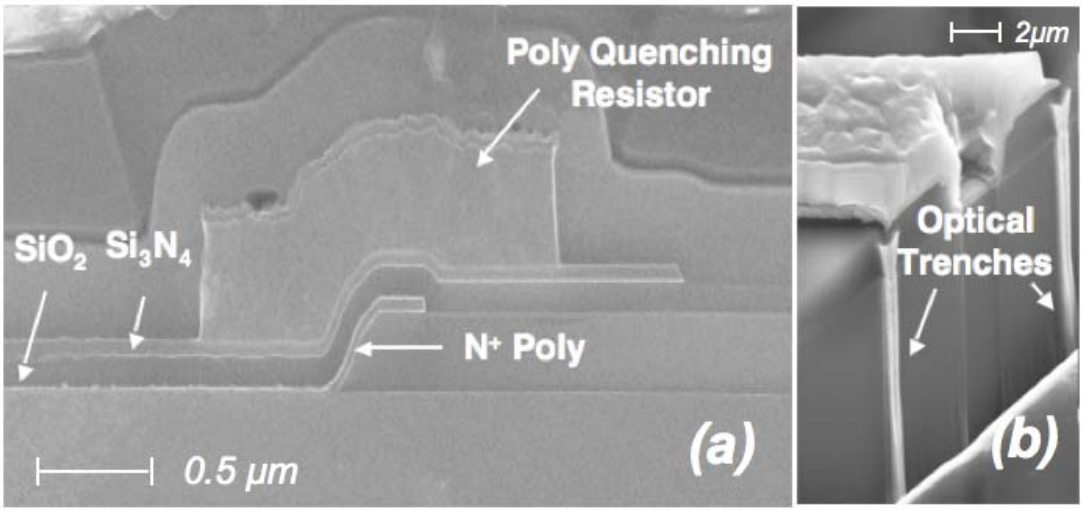

Figure 2.3: *(a) Scanning electron microscopy (SEM) image of the single pixel cross section, (b) Focused ion beam (FIB) image of the optical trenches.*

A double-layer made of silicon oxide and silicon nitride is deposited on the top of the active region acting as anti-reflection coating (ARC). Different oxide layers are finally deposited in order to passivate the surface and the metal contacts are created by sputtering deposition of Al, Si and Cu. A dedicated gathering process has been developed in order to reduce the defects concentration in the active volume.

A schematic cross-section of the final structure of the single cell is shown in Figure 2.2. The areas delimited by the dashed lines *(a)* and *(b)* are shown in Figure 2.3. In Figure 2.3 *(a)* it is shown the Scanning Elctron Microscopy (SEM) image of the device cross section, where it can be identified the poly-si quenching resistor, the n+ poly-si layer and the double anti-reflective coating of a real cell. In Figure 2.3 *(b)* it is shown the Focused Ion Beam (FIB) image of the optical trenches that surround the cell.

The final vertical doping profiles, along the dashed vertical line in Figure 2.2, obtained after the different thermal treatments performed in the fabrication process, have been measured by Spreading Resistance Profiling (SRP) technique and they are shown in Figure 2.4. Vertical dashed lines separate the different layers forming the cell. The numbers associated to the line correspond to the numbers shown in Figure 2.2. The shallow cathode layer has a maximum doping concentration of ~ $5 \cdot 10^{19}$ cm^{-3} and a depth of ~ 0.2 µm

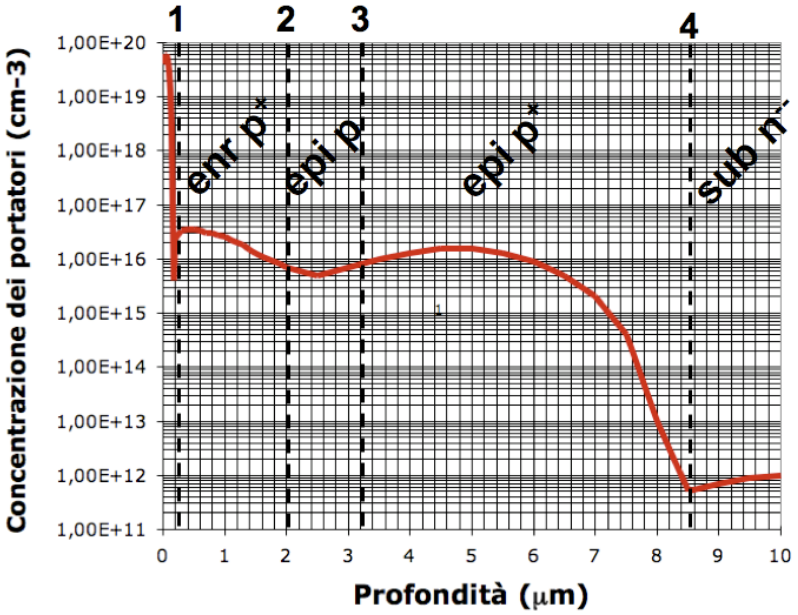

Figure 2.4: *SRP measurement of the final doping concentration of the single cell along the dashed vertical line in Figure 2.2*[3].

as previously reported. The depth was reduced with respect to the previous SPAD technologies [73,74] in order to improve the sensitivity of the detector in the blue and ultraviolet spectral range. The enrichment region is extended for ~ 2 μm and has a maximum doping concentration of ~ $3 \cdot 10^{16}$ cm^{-3} near the metallurgical junction setting the breakdown voltage equal to ~ -28 V. The original 2 μm wide buried epitaxial p+ layer has a final width of ~ 5 μm and a peak concentration of about $2 \cdot 10^{16}$ cm^{-3} of Boron atoms as a consequence of atom diffusion. The Boron atoms have diffused both in the substrate and in the epitaxial p layer causing the spred of the p+ epitaxy.

In Figure 2.5 (a) it is shown the final vertical profile concentration of the cell, along the vertical dashed line in Figure 2.2, in the first 2 μm layer below the Si/SiO_2 interface, in comparison with the simulated electric field for a reverse polarization of -30 V, i.e. 2 V above

[3] By courtesy of Markus Italia.

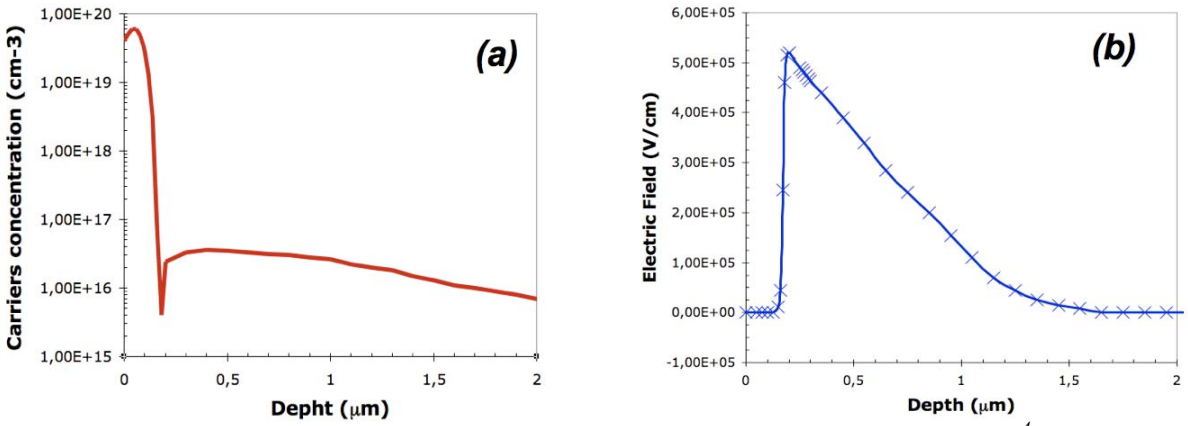

Figure 2.5: *(a) The SRP measurement of the final doping concentration*[4] *and (b) the simulated electric field, at reverse polarization of -30 V, of a single cell along the dashed vertical line of Figure 2.2*[5].

the breakdown voltage of the junction (Figure 2.5(b)). The maximum peak of the electric field is located at ~0.2 μm from the Si/SiO_2 interface, i.e. at the metallurgic junction. The metallurgic junction is formed at the final diffusion depth of Arsenic ions from the high-doped poly-silicon layer into the p+ enrichment layer (see Figure 2.5(a)). In the first 0.2 μm of thickness the electric field is negligible while it linearly decreases from its maximum value as a function of depth into the p+ enrichment layer. At about 1.5 μm depth from the interface surface it is again negligible. The final doping concentration profile along the vertical dimension, and its corresponding electric field, is uniform in the whole extension of the active area of the cell. In Figure 2.6 it is shown the 2D simulation of the electric profile performed at a bias polarization of -30 V. The electric field at the lateral border is well below its maximum value and is negligible with respect to the maximum value in the active region. The black continuous line in Figure 2.6 shows the metallurgical junction. At the border of the active area, the n implanted guard ring, that penetrates into the p enrichment region for about 2 μm depth, reduces the electric field to prevent from lateral breakdown. The corresponding ionization coefficients at the border are well below the value needed for ionization

[4] By courtesy of Markus Italia.
[5] G. Valvo, R&D Department STMicroelectronics, private communications.

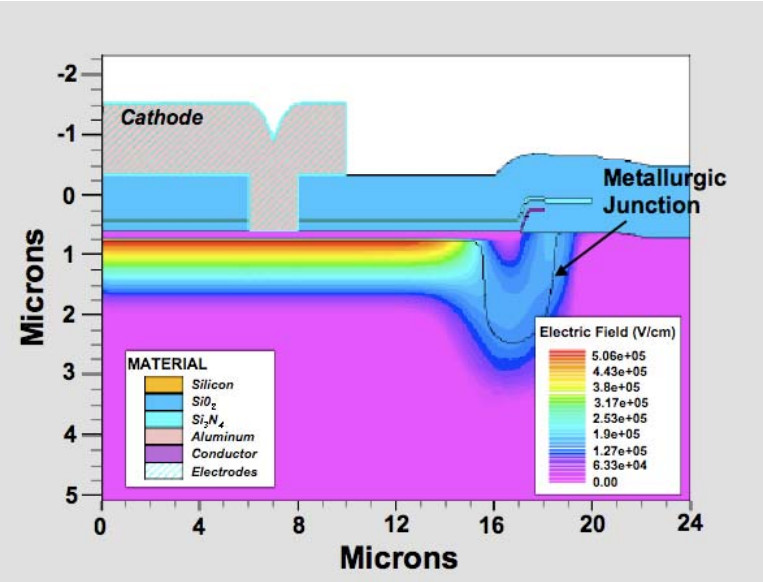

Figure 2.6: *2D simulation of the electric field in a single cell for a bias polarization of -30 V*[6].

under typical bias voltages operation (0÷20% OV). The lateral breakdown takes place at a bias voltage of ~ -70 V (~ 250% OV) at room temperature. The single cell structure fabricated by ST Microelectronics is then optimized to amplify the photo-generated carriers uniformly in the central region of the structure. Those carriers, thermally or photo-generated, that have the maximum probability to trigger an avalanche discharge are, in particular, electrons that start from the boundary of the depleted region at the p enrichment side below the active region. They have, in fact, enough space to increase their kinetic energies by the acceleration due to the electric field and produce other e-h pairs in the center of the depleted region where the impact ionization rate is the highest.

[6] G. Valvo, R&D Department STMicroelectronics, private communications.

§ 2.2 Single pixels static electrical characterization

The single pixels are basically p-n silicon diodes with a large resistor in series. Useful information on the device operation therefore can be obtained from the direct and reverse current voltage characteristics in dark condition.

The DC electrical characterization has been performed at wafer level using a Cascade Microtech Probe Station 11000. The probe was shielded from visible electromagnetic radiation by means of a dark plastic cover so as to provide the required dark condition. The samples were cooled using a Temptronic *TPO 3200A* ThermoChuck that provides a stabilized temperature between -60°C and 200°C. Current to voltage measurements were acquired using an *HP 4156B* precision semiconductor parameter analyzer with an integration time of 1s connected to the Probe Station by means of Kelvin Triaxial Cables. Kelvin connections eliminate the voltage drop caused by cable and probe contact resistance assuring an accurate measurement of the current. The integration time was set to 1s in order to reduce transient component.

§ 2.2.1 Forward current

The experimental measured forward current of a single pixel at 25°C is shown on a semilog plot in Figure 2.7. Three different regimes can be identified. The first one (see Figure 2.7) happens for $V_{BIAS} < 0.1$ V. A leakage current almost independent on the voltage in the range of 0.1 pA is measured. This component has the same polarity (negative) and the same value of the reverse leakage current. The nature of this leakage current is still unclear. It might be related to surface generation and recombination centers. To complicate the interpretation is its low value, really close to the minimum measurable current value imposed by the instrumentation (~0.01 pA), which suggests taking care about speculations. The second regime happens for $0.2V<V_{BIAS}<0.5V$. In this regime the experimental measured current approaches the current voltage dependence of an ideal p-n silicon junction, denoting that

currents are due to the diffusion of minority carriers from the quasi-neutral p region (see APPENDIX B). In this regime the current is expressed by the following relation:

$$I = I_0 \exp\left(\frac{qV}{nk_BT}\right) \tag{2.2.1}$$

where I_0 is the saturation current of the p-n ideal junction and is done by the Schokley equation (see APPENDIX B) , V the bias voltage and n the ideality factor of the pn junction. A plot of *log(I)*[7] versus V, as the case of Figure 2.7, yields a straight line for 0.2V < V < 0.5V. Extrapolating the line to V = 0 gives I_0. The slope of the *log(I)* versus V gives the experimental ideality factor n [75]. At 25°C the saturation current of the p-n junction is 10^{-15}A and the ideality factor n is equal to 1.05.

The third regime happens for $0.5V<V_{BIAS}<1.5V$. In this regime the current deviates significantly from the ideal diode regime. A linear behavior of the *log(I)* versus V is again observed, but the slope is drastically reduced. This strange trend is attributed to a parasitic Schottky formed at the anode contact. The contact between the metal and the high-doped p sinker forms a parasitic Schottky junction. When the single pixel is forward polarized, the parasitic Schottky junction results in reverse polarization. For $V_{BIAS}<0.5V$ the voltage drop through the parasitic Schottky is negligible and the current follows the ideal diode current-voltage law. For $V_{BIAS}>0.5V$ the drop voltage through the Schottky diode is no longer negligible, and the parasitic Schottky results in reverse polarization causing an abrupt reduction of the current.

This behavior of the forward current versus voltage as here described was observed in all the studied cases.

[7] We will generally use the logarithmic to base 10, written as "*log*", instead of the logarithmic in base e, written as "l*n*", because experimental data are plotted on "l*og*", not "*ln*", scales.

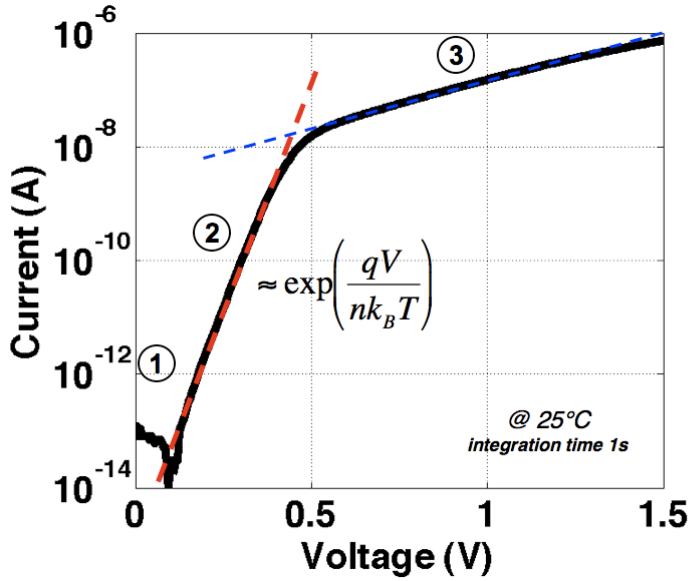

Figure 2.7: *Measured forward current at 25°C of a single pixel. Three different current regimes with respect to the applied voltage are identified.*

It is interesting to study the operation of the single pixel as a function of the temperature with a particular attention on the ideal diode regime because in this regime useful information about the p-n junction can be found.

In Figure 2.8 the experimental forward I-V curves current measured at different temperatures starting from -10°C to 100°C are shown. As previously discussed, the log(I) versus V is a straight line in the ideal region, where all the bias voltage drops essentially across the p-n junction. This happens at 25°C for $0.2V<V_{BIAS}<0.5V$ as already said. At higher temperature the cut-off of the current provided by the parasitic Schottky diode take place at lower voltage, while at lower temperature the first regime is extended at higher voltage. The ideal regime, when the p-n junction works as an ideal diode, is then shifted to lower voltage and it is shrunk as the temperature increases.

The extrapolated values at V=0 of the linear fit of the log(I) versus V (dashed lines of Figure 2.8), in the ideal regime, shown as circles in Figure 2.8, are the saturation currents I_0 of

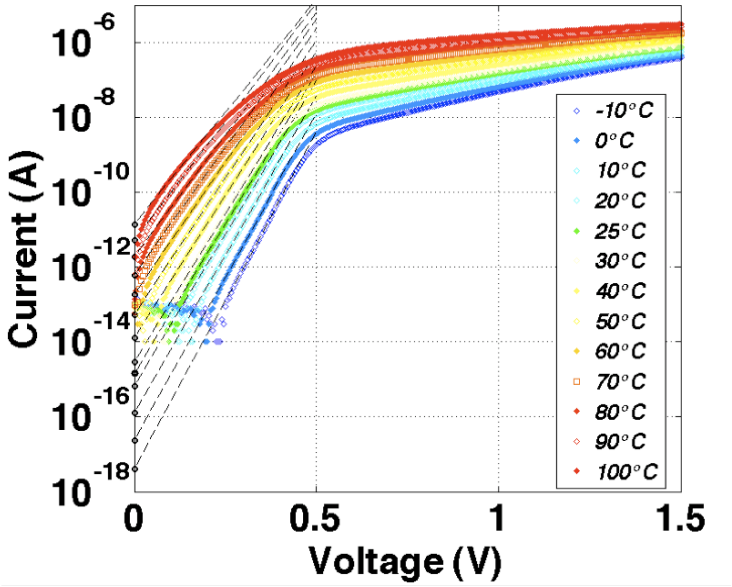

Figure 2.8: *Measured forward current of a single pixel at different temperature Green diamonds are the currents measured at 25°C. Dashed lines are the fits of the log(I) in the ideal region. The projection of the fit to V=0 is the saturation current I_0.*

the p-n junction at different temperature. The slope of a plot of $\ln(I_0)/T^2$ versus $1/k_BT$ is expected to be the energy gap E_G of Si [76], as reported in Figure 2.9 (a).As this is indeed the experimental, it confirms result that the forward current of the p-n junction is totally due to the diffusion of minority carrier from the quasi-neutral region for the investigated all temperatures and that the generation-recombination centers in the depleted region have a very low concentration.

A further confirmation is done by the values of the experimental ideality factor *n* of the p-n junction. Figure 2.9 (b) shows the ideality factor as a function of the temperature, extrapolated from the slope of the linear fit of the l*og(I)* versus *V* in the ideal region of the forward currents of Figure 2.8. The ideality factor *n* is equal to 1.05 from -10°C to 50°C while for higher temperature has a weak increase mainly due to the cut-off of the current performed by the parasitic Schottky.

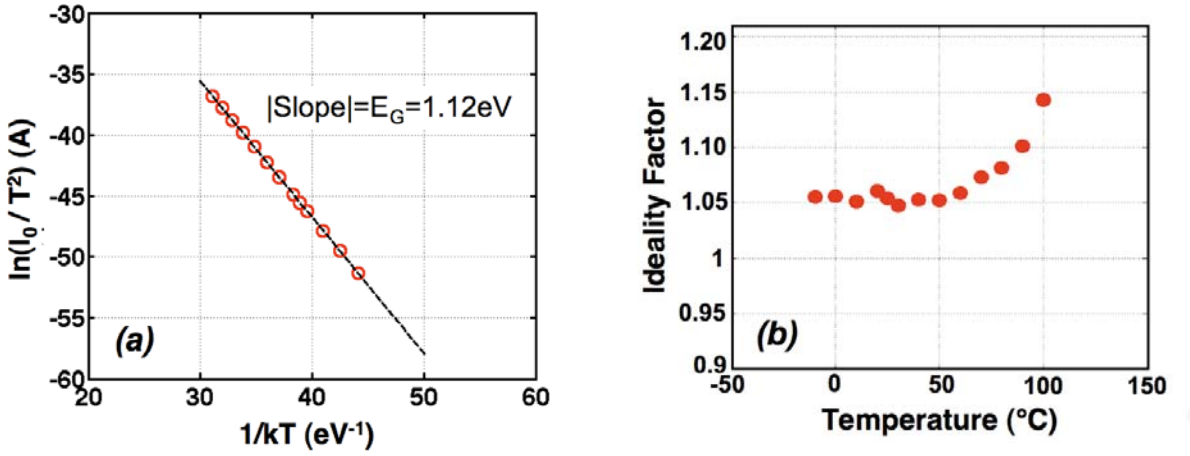

Figure 2.9: *(a) Arrhenius plot of the saturation currents I_0 at different temperature. (b) Experimental ideality factor at different temperatures.*

The last consideration on the forward current concerns the quenching resistance. At voltages above ~2 V, (not shown in Figure 2.7 and Figure 2.8), the voltage drop trough the quenching resistance can't be neglected. In fact, the high current circulating through the single pixel, determines a voltage drop trough the quenching resistance greater than both the voltage drop trough the diode and the parasitic Schottky. Then above ~ 2 V the current grows linearly with respect to the voltage following the well known ohmnic law, $I=R_Q \cdot V_{BIAS}$, allowing the measurement of the quenching resistance. However we preferred measuring the quenching resistance, R_Q, in a special single cell structure with three contacts (shown in the insect of Figure 2.10(a)), which provides the possibility of polarizing directly the quenching resistance contacts. Figure 2.10 (a) shows the current flowing through the quenching resistance with respect to the bias voltage, ranging from 0 to 5 V, and the temperature, ranging from -25°C to 85°C. The inverse of t he slope of the current measurement with respect to the voltage is R_Q.

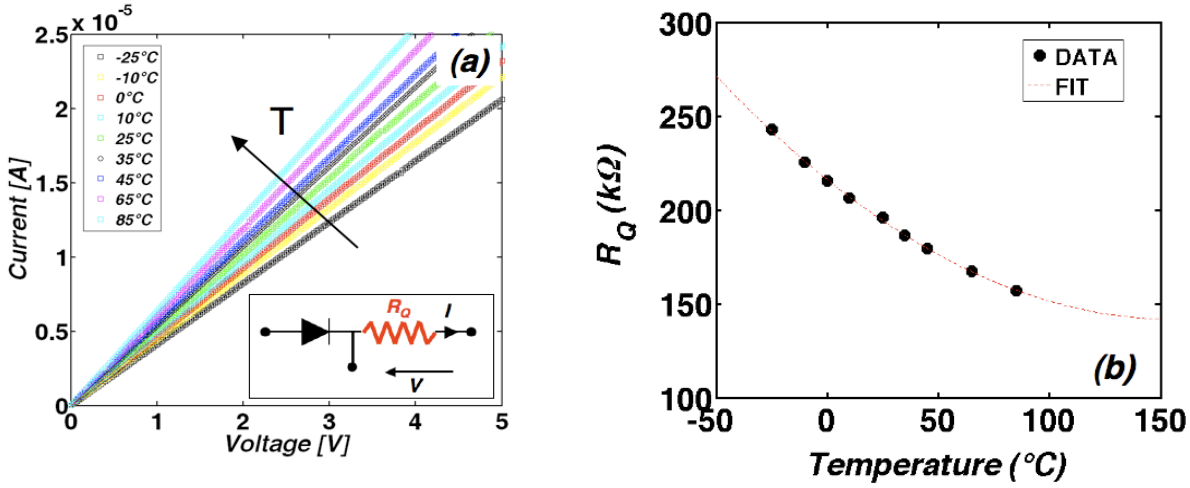

Figure 2.10: *(a) Current as a function of the Bias voltage and the temperature for the quenching resistance measured in the three pad single pixel structure shown in the inserct. (b) quenching resistance values as a function of the temperature. The red dashed line is a quadratic fit of the data.*

Figure 2.10 (b) reports the measured R_Q values as a function of the temperature. R_Q decreases with temperature with a quadratic law (dashed red line in Figure 2.10 (b)) as expected by a polysilicon layer resistance [77]. The R_Q value is 220 kΩ at 25°C and varies of about 100kΩ in the temperature range between -20 and 100°C as shown in Figure 2.10 (b).

§ 1.2.2 Reverse current

The reverse characteristics contain useful information on the functionality of the single pixels. Typical current-voltage characteristics (I-V) of a single pixel in reverse polarization measured at 25°C are shown in Figure 2.11. The breakdown voltage (BV), as clearly visible, is about -28 V. The I-V presents three separate regions. The first is extended from 0 V up to BV and the corresponding characteristics is depicted with green markers in Figure 2.11. The current in this region, which will be referred to as "*leakage current*" in the following, is of the order of ~ 10 fA at 25°C, close to the instrument sensitivity. From BV to about -34 V, i.e from 0 to % 20 of the over-voltage (OV), it is extended the second region. The corresponding

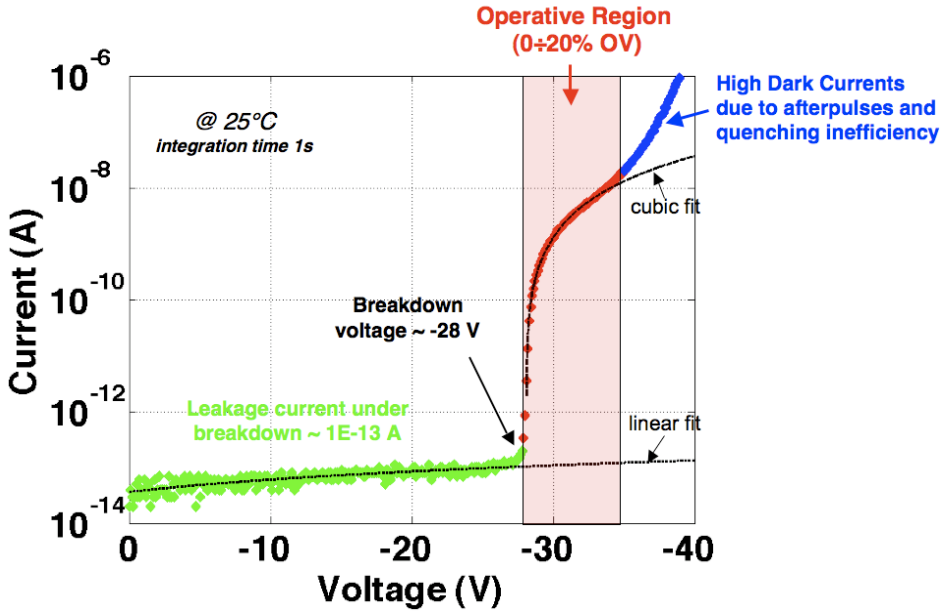

Figure 2.11: *Reverse current-voltage characteristic of a single pixel at 25°C. Three different regions are shown.*

characteristic is depicted with red markers in Figure 2.11. The current in this region has an abrupt increase with respect to the voltage and follows a cubic trend. We will refer to the current in this region as "*dark current*" in order to distinguish from the leakage current. Finally, in the third region, for voltage above -35 V, depicted with blue markers, the current deviates from the cubic behavior and increase steeply with the voltage.

The leakage current has a linear trend with respect to the voltage as shown in Figure 2.12. It consists theoretically of different geometrical components [78]: the area component I_A, the perimeter leakage current I_P, and a possible corner contribution I_C. The area component I_A depends both on diffused carriers and generated carriers in the bulk, while the perimeter leakage I_P consists of peripheral diffusion, a peripheral bulk generation and a surface recombination current at Si-SiO2 interface [79]. The leakage current in such device seems to be dominated by the peripheral current I_P, as confirmed by the fact that the dark current values are orders of magnitude lower than the values predictable from the leakage current

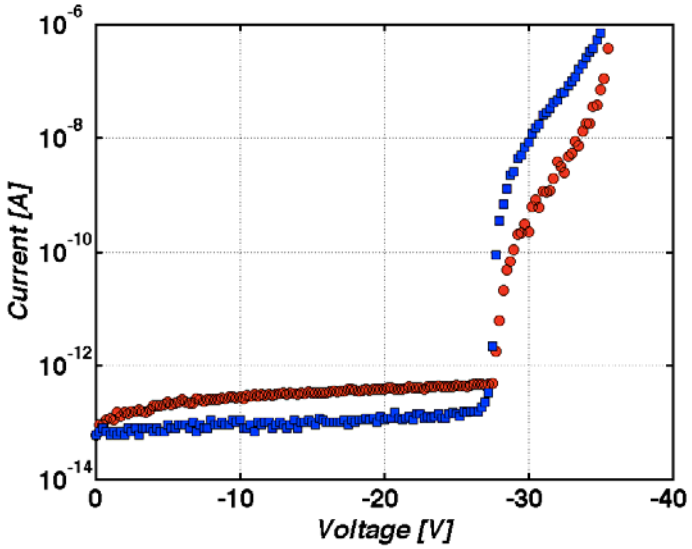

Figure 2.12: *Reverse current-voltage characteristic of two single pixels. The pixel with lower dark currents (red squares) has a greater leakage current.*

levels. In fact, the peripheral current component, when the device operate above breakdown in Geiger Mode, has a negligible probability to multiple ionize, because the peripheral electric field is smaller that than in the active area. Whatever the nature of the leakage current is, we can assure that it has no correlation with the dark counts. As a demonstration, Figure 2.12 shows the reverse current-voltage characteristics of two different single pixels. The device with higher leakage current, red squares, above the breakdown manifest the lower dark current, while the single pixel with lower leakage current, blue circles, has a greater dark current.

The second region, is the real interesting voltage range for the single photon detection application. As already said, it is extended from -28V to -34V, at room temperature, that corresponds to 0÷20% of the OV. It is interesting to note that the dark current as a function of the bias voltage is characterized by a cubic growth (see Figure 2.11). This law is maintained up to about -34V then the current starts increasing at a much higher rate. The behavior of the dark current can be explained considering the device operation above BV. The static current-voltage characteristics in this region can be modeled as the mean charge (Q) delivered per

pulse times the number of pulses in 1s. The former divided by elementary charge q is the mean gain ($G=Q/q$), while the leatter is the dark count rate (DC) of the single pixel. The static current is then given by the relation:

$$I = Q \cdot DC = q \cdot G \cdot \tilde{f} \cdot A_d \tag{2.2.2}$$

where $\tilde{f}$ is the frequency of the dark count rate per unity area ($s^{-1}cm^{-2}$) of the device and A_d is the active area of the device. The DC is obviously the product of $\tilde{f}$ time A_d. Depending on both the mean gain and the dark count rate (or equivalently $\tilde{f}$) versus voltage behavior, the static current-voltage characteristics show a well defined shape. In the device produced by ST, as we will discuss in the following, the mean gain has a parabolic dependence on the bias voltage while the DC is linear. Therefore, the product of this two terms explains the cubic dependence of the current with respect to the voltage.

At bias voltages greater than-35V the current increases more rapidly than a cubic law. This is mainly due to the increase of the afterpulsing and the inefficiency of the quenching mechanism. At higher voltage secondary carriers generated during the primary avalanche cascade are able to trigger new avalanche phenomena, due to the high electric field in the depleted region, before the voltage across the junction is restored to the bias voltage. This phenomenon produces above -35V a further increase in total DC. Moreover the quenching mechanism at higher voltage may not be totally efficient. At higher voltage the time to quench the avalanche increases and the avalanche current is self-sustaining for a larger period [16], producing a distorted pulse and a higher mean charge. This implies an increase of the mean gain, more than parabolic with the bias voltage.

Figure 2.13 shows the current-voltage characteristics in reverse polarization of all single-pixel test sites on a wafer (31 devices) of a typical pre-production lot of SiPM realized by STMicroelectronics at room temperature. In order to monitor the uniformity of the devices over the area of the whole wafer, the breakdown voltage and the dark current at V_{BIAS}=-30V

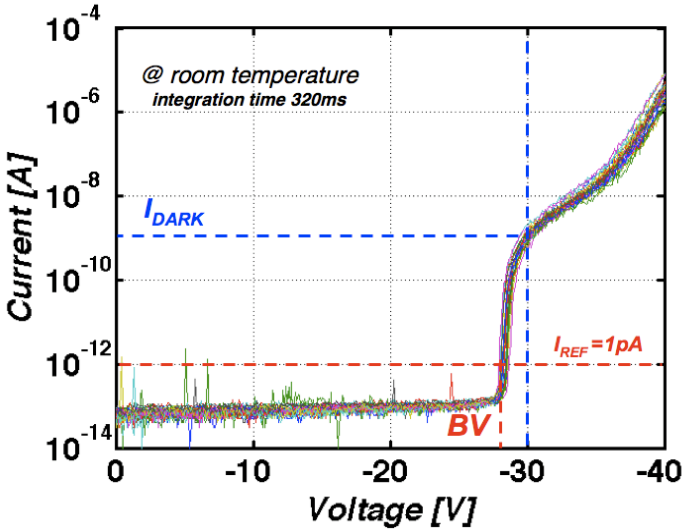

Figure 2.13: *Reverse current-voltage characteristic at room temperature (~27°C) of 31 single pixels fabricated in a wafer.*

have been measured as shown in Figure 2.13. The resulting histograms and the normal distribution are shown in Figure 2.14 (a) for the *BV* values and in Figure 2.14 (b). for the dark currents. The BV distribution has a mean value of -28.35V and standard deviation of 195 mV while the dark current distribution has a mean value of 1.1nA and a standard deviation of 0.3nA.

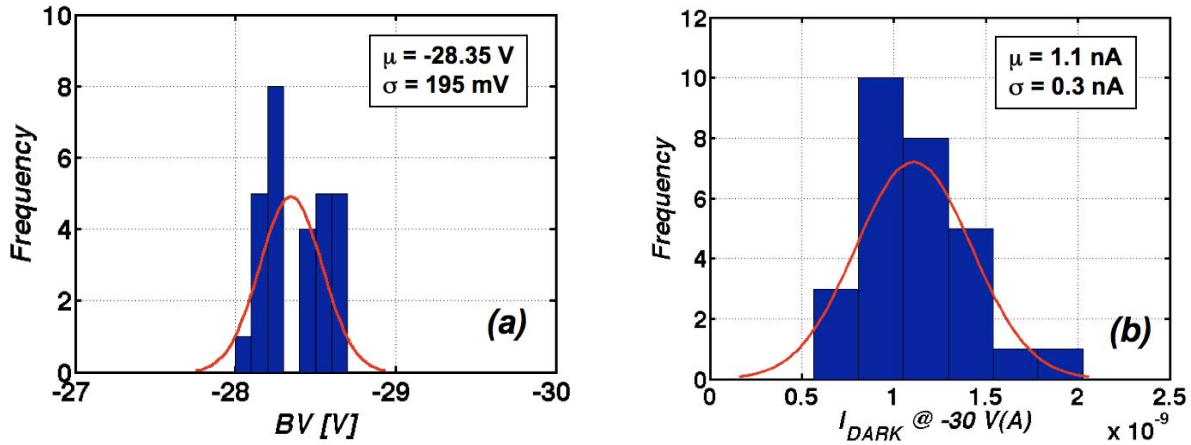

Figure 2.14: *(a) Breakdown Voltage distribution and (b) dark current distribution at -30V for single pixel in a wafer measured at room temperature (~27°C).*

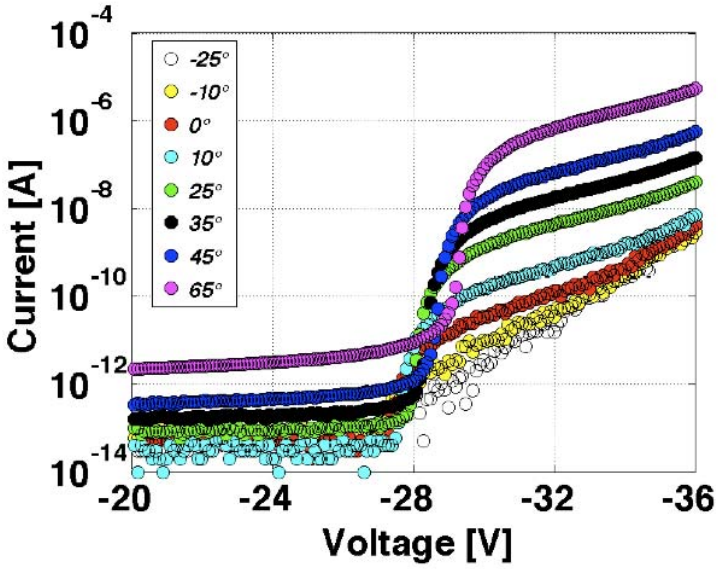

Figure 2.15: *Reverse current-voltage characteristic at different temperatures of a single pixel.*

As in the case of the forward current, it is interesting to observe the temperature dependence of the reverse current-voltage characteristics. Figure 2.15 shows the current of a single pixel for bias voltages from -20V to -36V at different temperatures ranging from -25°C to 65°C. The first consideration concerns the breakdown voltage. The *BV* increases with the increasing of the temperature. The breakdown voltage variation with respect to the temperature is described by the expression:

$$BV(T) = BV_0 + (T - T_0)\frac{dBV}{dT} \tag{2.2.3}$$

where BV_0 is the breakdown voltage at 25°C and T_0 is the room temperature (25°C).

Figure 2.16 reports the measured *BV* as a function of temperature. The *BV* at -25°C is ~ -26.5 V and it linearly increases up to ~ -29V at 65°C with a temperature coefficient, *dBV*/*dT*, of -29mV/°C as experimentally determined by fitting Equation 2.2.3 (dashed line). It has to be

note that the BV value at 25°C, -28 V, is in perfect agreement with the universal expression [75] for abrupt junctions, as the case of the single pixel where $N_D >> N_A$, given by the following equation:

$$BV \cong -60 \cdot (E_G/1.1)^{3/2} \cdot (N_B/10^6)^{-3/4} \quad (2.2.4)$$

where E_G is the room –temperature bandgap in eV and N_B is the ionized background impurity concentration of the lightly doped side. For E_G = 1.12 eV (Si bangap at room temperature) and $N_B = N_A = 3 \cdot 10^{16}$ (cm^{-3}) Equation 2.2.4 gives a BV value equal to -27.77 V.

The variation of the BV with the temperature is of great interest because many characteristics of the photon detector, as an example the gain, depend on the over-voltage applied ($V_{OV} = V_{BIAS} - BV$) and consequently on the temperature.

The explanation of the increase of the BV at higher temperature is that the carriers passing through the depletion layer under the high field and becoming hot lose their energy in the collision with optical phonons after traveling on average an electron-phonon-mean free path λ. The value of λ

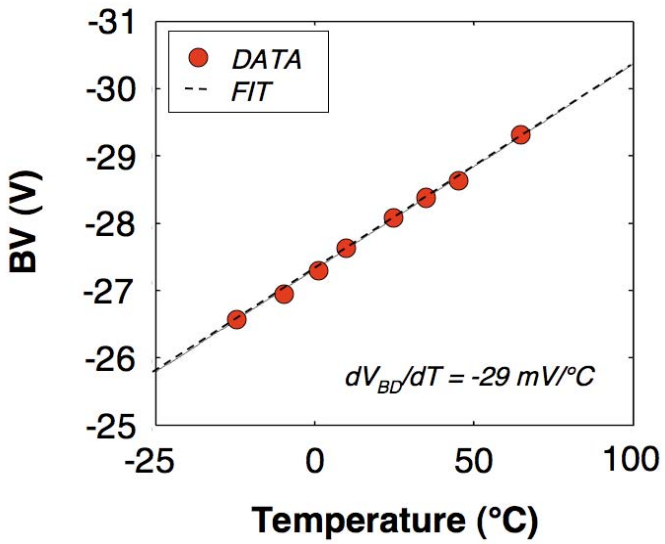

Figure 2.16: *Breakdown voltage as a function of the temperature of a single pixel.*

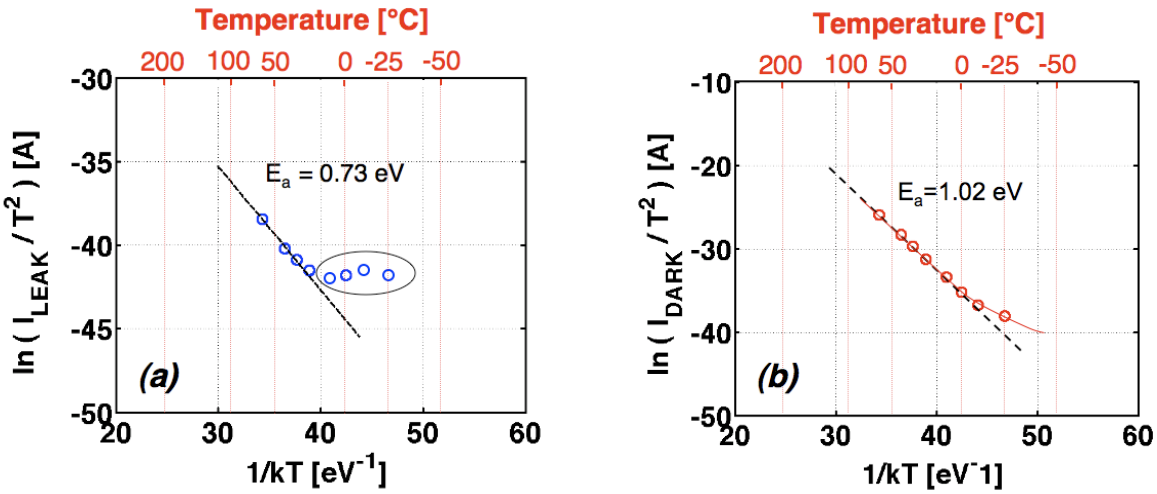

Figure 2.17: *Arrhenius plots of (a) the leakage current at V_{BIAS}=-20V.and (b) the dark current at a constant OV of 2 V.*

decreases with temperature [80]. Therefore, the carriers acquire less energy on each electron-phonon impact for the same external voltage. Hence the carriers must pass trough a greater potential difference, or higher voltage, before they can acquire sufficient energy to generate an electron-hole pair by impact ionization.

Concerning the leakage and the dark current dependence on temperature, useful insight on the mechanisms of diffusion or generation of free carriers in reverse polarization has been given by the slope of the Arrhenius plots. The activation energy (E_a) of reverse currents is close to the silicon energy band gap (E_G = 1.12eV) when the reverse current is dominated by the diffusion current and close to half the silicon energy band gap (E_G/2 = 0.6 eV) when dominated by generation [81]. Figure 2.17 shows the Arhhenius plots of the reverse leakage current at V_{BIAS} = -20V (a) and of the dark current at a constant OV = 2V (b). The leakage currents for temperature below 25°C are constant likely because close to the minimum sensitivity of the instrumentation (enclosed in the ellipse data in Figure 2.17 (a)). Therefore, the Arhhenius plot of the leakage current doesn't provide information at lower temperatures. However, at higher temperatures, above 25°C, the activation energy is 0.73 eV, between E_G and E_G/2. This evidences that the leakage current is governed by both diffusion and

generation processes, probably peripheral as discussed before, giving the same contribution to the overall current even at higher temperature. Concerning the dark current, the activation energy provided by the Arrhenius plot (Figure 2.17 (b)) is close to the energy band of silicon for temperature above 0°C, evidencing that the diffusion of carriers is the dominant process. At lower temperature the deviation of the data from the linear fit is clearly evidence that another concurrent process occurs, as explained in the following paragraph.

§ 2.3 Gain

The gain, as discussed in Chapter 1, is an important parameter of a SiPM. It depends both on the voltage and on the temperature of operation.

In this paragraph we discuss about the experimental gain of a single pixel measured with two independent methods. The former one consists in integrating the pulse transient of the dark current measured with an oscilloscope, and we will refer in the following as the gain obtained by the "*transient current measurement mode*". The latter consists in measuring the photocurrent of the single pixel under a known constant illumination, as explained later. We will refer to the results obtained with this approach as the gain obtained by the "*photocurrent measurement mode*". Measurements are performed at different temperatures and at different voltages, as to obtain the gain dependence with respect to both these two parameters.

§ 2.3.1 Transient Current Measurement Mode

The first method we discus, used to measure the gain of the single pixel as a function of the voltage and the temperature, is the transient current measurement mode. Figure 2.18 shows the schematic of the adopted measurement setup. The pixel is reverse polarized applying a constant negative voltage greater than the BV to the anode contact. The constant voltage is provided by an *HP 4156B* precision semiconductor parameter analyzer in constant stress mode. The current flowing trough a 50Ω series resistance, R_S, connected to the quenching

resistance, has been measured as the voltage drop trough R_S, V_{OUT}, with an *Agilent Infiniium MSO8064A* digital oscilloscope with 600 Mhz bandwidth and 4Gsa/s. A 50Ω coaxial cable (RG59) realizes the connection between o-scope and sample. The data registered by the o-scope are then stored into a personal computer, using the GPIB protocol, for further analysis. The measurements are performed at wafer level using a *Cascade Microtech Probe Station 11000*. The probe, as already discussed, was shielded from visible electromagnetic radiation by means of a dark plastic cover so as to provide the required dark condition. The samples were cooled using a Temptronic *TPO 3200A* ThermoChuck that can provide a stabilized temperature between -60°C and 200°C.

The measured V_{OUT} is a replica of the dark current pulse flowing trough the single pixel $I=V_{OUT}/R_S$. The signal coming from the single pixel, as discussed in paragraph §1.3, is expected to show a very fast (hundreds of ps) leading edge, determined both by the avalanche spreading and by the discharge of the diode capacitance C_D through the diode series resistance R_D (that includes the resistance of both the neutral regions of the semiconductor and the space-charge of the avalanche junction, and the series resistance produced by the poor Schottky contact at the metal/p^+/Si anode junction), and a slow exponential decay due to the

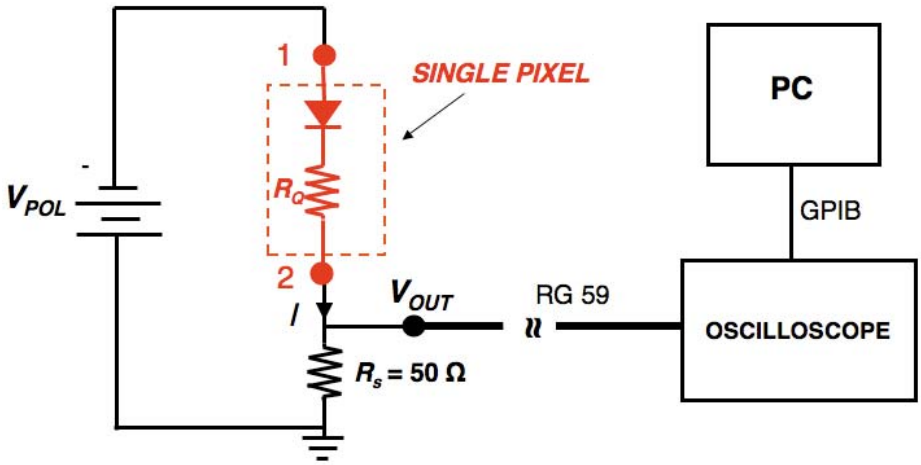

Figure 2.18: *Schematic setup of the dark pulse transient current measurement.*

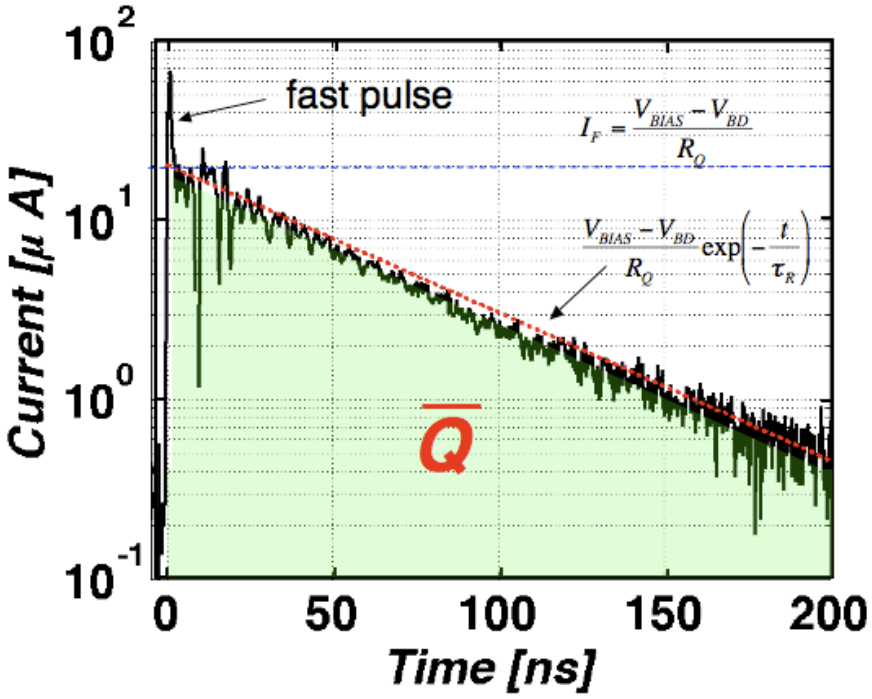

Figure 2.19: *Dark Pulse of the single pixel at 25°C and at V_{BIAS}= -32V .*

recharging of the C_D trough R_Q, determined by the time constant τ_R=$R_Q C_D$. R_Q is ~220 kΩ at 25°C and C_D is ~170 fF as determined by C-V measuremnts, giving τ_R~37 ns.

Figure 2.19 is shows in a semilog scale the average of 1000 dark current pulses stored by the oscilloscope at 25°C and at V_{BIAS} = -32V. The shape is different from what expected since it presents a very fast pulse (with a duration of few ns) followed by a low slow tail. This behavior has been reported by other groups [82-83]. It can be explained adding to the equivalent circuit of the single pixel (see Figure 2.20 (a)) a parasitic capacitor C_Q in parallel to the quenching resistance R_Q. This parasitic element is physically related to the fact that the polysilicon quenching resistance lays on top of the junction area, as shown in Figure 2.20 (a), thus a direct capacitive coupling is present between the resistor itself and the diode. During the avalanche process C_Q discharge through the diode series resistance R_D giving the fast pulse governed by the time constant $R_D C_Q$. At 25°C R_D is estimated to be at least 500 Ω or more, the quenching capacitance, estimated considering two parallel plates with an area

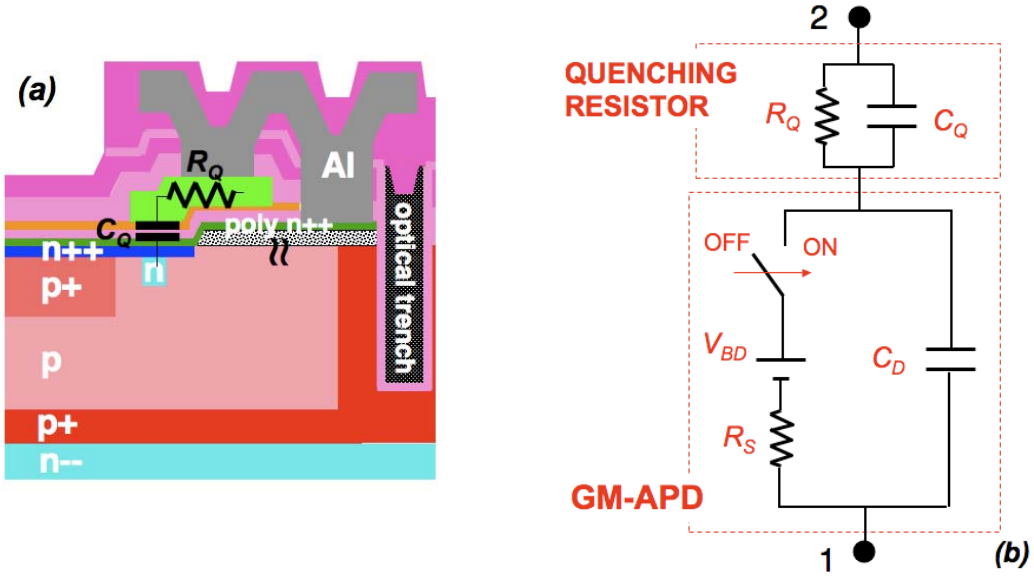

Figure 2.20: *(a) Schematic cross section of the single pixel showing the physical origin of the parasitic quenching capacitance C_Q. (b) Schematic of the equivalent electric circuit of the single pixel.*

of 356 μm^2 at a distance of 1400 Å with a SiO_2 dielectric layer interposed, is $C_Q \sim$ 80 fF. The time constant of the fast pulse is then of the order of at least of 40 ps or more. For the lower limit this is a too fast phenomenon to observe with accuracy with our instrumentation (the maximum resolution of the oscilloscope at 4GSa/s is 250ps/pt). Furthermore the amplitude of such fast pulse is expected to be attenuated by the coaxial cable and the connection [84]. But the initial peak is clearly visible, thus suggesting that likely C_Q and R_D are larger than estimated.

When the current reaches the level $I_F=(V_{BIAS}-V_{BD})/R_Q$, blue dashed line in Figure 2.19, the avalanche process is quenched and the pixel capacitance starts recharging trough R_Q with the time constant $\tau_R = (C_D+C_Q)\cdot R_Q \sim 55ns$ [82]. Figure 2.19 also shows (dashed red line) the theoretical recharging current I_R, given by the equation:

$$I_R(t) = \frac{V_{BIAS} - V_{BD}}{R_Q} \exp\left(-\frac{t}{\tau_R}\right). \qquad (2.3.1)$$

The subtended area of the measured mean dark current pulse is the mean charge $\overline{Q}$ released in a pulsing event (see Figure 2.19). It is to be noted that in this experimental condition the avalanche process is triggered by a free carrier generated in dark condition. We expect that the mean charge $\overline{Q}$ is the same if the free carrier triggering the avalanche process is photo-generated.

The mean gain $\overline{G}$ of the single pixel is then given by:

$$\overline{G} = \frac{\overline{Q}}{q} \tag{2.3.2}$$

where q is the elementary charge.

In a first approximation, ignoring the initial fast pulse, the charge delivered during the dark current pulse is due to the recharge of the pixel capacitance through the quenching resistance. Then the theoretical gain, referring to Figure 2.21 is given by:

$$G_{Theo} = \frac{Q_{Theo}}{q} = \int \frac{(V_{BIAS} - V_{BD})}{q \cdot R_Q} \exp\left(-\frac{t}{\tau_R}\right) dt = \frac{(V_{BIAS} - V_{BD})}{q}(C_D + C_Q) \tag{2.3.3}$$

To obtain the gain dependence with respect to the bias voltage, the dark current transient has been measured for a fixed temperature at different V_{BIAS}. Figure 2.21 shows the dark current transients at 25°C for a bias polarization ranging from -30V to -34V. In the same plot the recharging current (dashed line curves) at different V_{BIAS} as given by Equation 2.3.1, are reported.

The area subtended by the dark current has been integrated with respect to the time $\bar{t}$. Figure 2.22 (a) shows the resulting gain as a function of V_{BIAS} and the integration time $\bar{t}$. Increasing the integration time the mean gain increases. For small integration time (<50ns) the gain varies linearly with respect to the voltage. For integration time $\bar{t} > 4\tau_R$ it saturates showing an over-

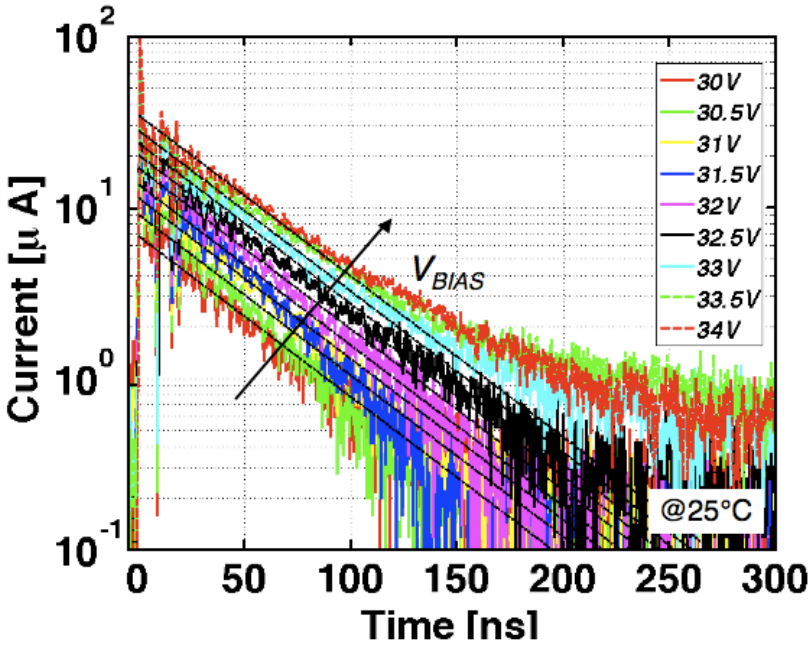

Figure 2.21: *Dark current pulses of a single pixel at 25°C and at different bias voltage conditions.*

linear behavior. In the same plot the theoretical mean gain G_{Theo} given by Equation 2.3.3 is shown as dashed red line. It could be noted the perfect agreement between the theoretical gain G_{Theo} and the experimental mean gain for $\bar{t} > 4\tau_R$ at lower voltage. However at higher voltage it increases more than linearly. A reasonable explanation for such behavior can be attributed to the afterpulsing. At higher voltage the afterpulsing increases [73] and the tail of the measured current transient is affected by this contribution (see Figure 2.21). This leads to a more than linear increase of the mean gain. Because we are interested, as clear in the following, to know the mean gain due to the primary dark or photon event, this contribution is quite welcome.

In Figure 2.22 (b) is shown the experimental gain at 25°C for an integration time $\bar{t} = 4\tau_R =$ 220 ns as a function of the over-voltage. In the following we refer to the experimental gain as the one obtained for an integration time $\bar{t} = 4\tau_R$. In the same figure is shown the G_{Theo} given by Equation 2.3.3 (red dashed line). As already said $\overline{G}$ shows an over-linear behavior with respect to the voltage, in fact rather than by the linear expression of Equation 2.3.3 the experimental data

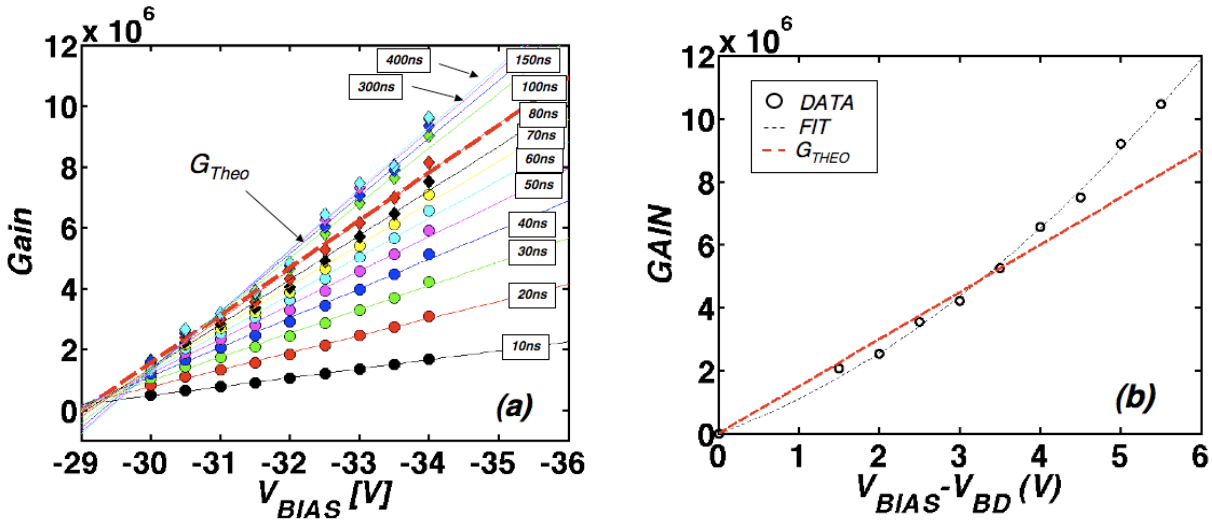

Figure 2.22: *(a) Experimental gain of the single pixel at 25°C as a function of the bias voltage and of the integration time. The red dashed line is the theoretical gain given by Equation 2.3.3 (b) Experimental gain of the single pixel at 25°C for an integration time* $\bar{t} = 4\tau_R \sim 220$ *ns as a function of the over-voltage.*

are better fitted by the quadratic function:

$$\overline{G} = A(V_{BIAS} - V_{BD})^2 + B(V_{BIAS} - V_{BD}) \tag{2.3.4}$$

where V_{BIAS}-V_{BD} is the applied over voltage OV and A=1.77·10^5 (V^{-2}) and B=9.24·10^5 (V^{-1}).

The same measurement has been repeated at different temperatures ranging from -25°C to 65°C. Figure 2.23 shows the dark current transient measured at different temperatures and at a V_{BIAS}= -31V. Increasing the temperature the slope of the current during the recharging event increases. This is explained by the lowering of the quenching resistance with increasing temperature, as discussed in § 2.2.2, and therefore by the decrease of the time constant $\tau_R = (C_D + C_Q) \cdot R_Q$. The values of τ_R for different temperatures are reported in Table 2.1. The dashed lines of Figure 2.23 are the recharging currents calculated according to Equation 2.3.1, using the correct values of τ_R, R_Q and V_{BD} at each given temperature.

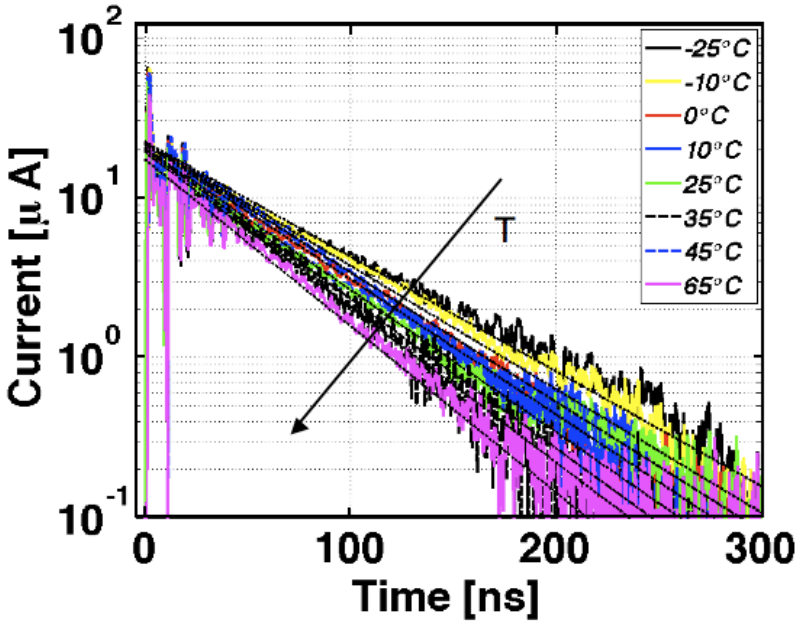

Figure 2.23: *Dark current pulses of the single pixel at different temperature and at V_{BIAS} = - 31V. Dashed lines are the recharge current given by Equation 2.3.1.*

Figure 2.24 shows the mean gain evaluated by the transient current mode as a function of the voltage and the temperature. For the same bias voltage the gain decrease with temperature since high energy is required for impact ionize. Dashed lines are the gain quadratic function of Equation 2.3.4 providing the correct V_{BD} at each temperature. The gain shift versus voltage for the increasing temperature is equal to the breakdown voltage variation.

T (°C)	τ_R (ns)
-25	68
-10	64
0	61
10	58
25	55
35	52
45	50
65	45

Table 2.1: *Recharging time constant, τ_R, versus temperature.*

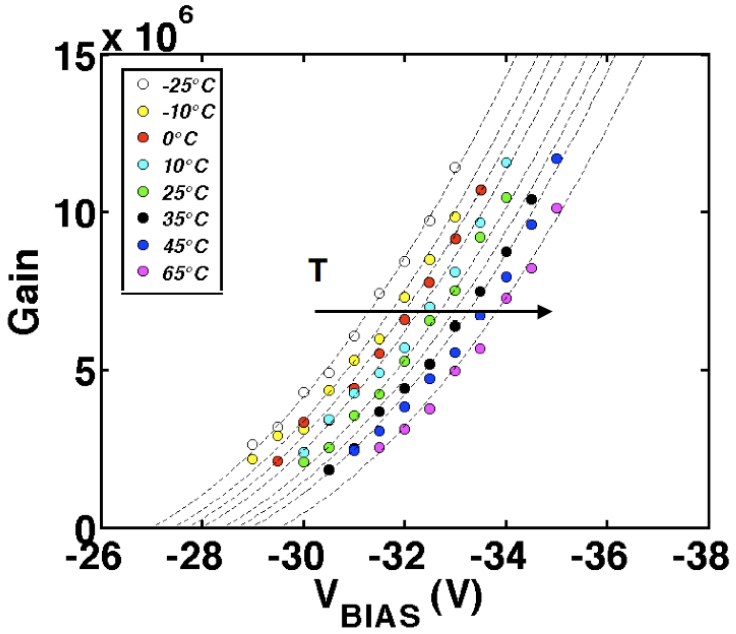

Figure 2.24: *Experimental gain of the single pixel as a function of the voltage and of the gain. The dashed lines are the gain function given by Equation 2.3.4.*

§ 2.3.2 Photocurrent Measurement Mode

The non-linear behavior of gain is an important feature of SiPMs and we have investigated this issue in further detail. In particular we have measured the gain by an alternative, independent method, hereafter proposed.

From Equation 2.2.2 it is easy to estimate the photodetector current under illumination I_{Light}, in the operative V_{BIAS} range, i.e. for $|V_{BD}| < |V_{BIAS}| < |V_{BD}|+0.2\ OV$ ($28.5V < |V_{BIAS}| < 34V$ at room temperature). In fact one expects that:

$$I_{Light} = q \cdot G \cdot \left(\tilde{f}_{DC} + QE \cdot \tilde{f}_{Phot} \right) \cdot A_d \qquad (2.3.5)$$

where q is the electron charge (C), G the pixel gain, $\tilde{f}_{DC}$ is the dark count rate ($s^{-1}cm^{-2}$), $\tilde{f}_{Phot}$ the

photon flux incident on the pixel ($s^{-1}cm^{-2}$), QE is the corresponding external quantum efficiency and A_d the pixel active area (cm^2). If we are in a condition where $\tilde{f}_{Phot} >> \tilde{f}_{DC}$, G can be evaluated as:

$$G = \frac{I_{Light}}{\tilde{f}_{Phot} \cdot QE \cdot A_d}. \tag{2.3.6}$$

It is then clear that by measuring the pixel photocurrent it is possible to evaluate the gain of the device in the interested bias voltage range.

Figure 2.25 shows a schematic of the experimental setup used for the photocurrent measurement. A CW (continuous wave) laser, with 659 nm wavelength, produced by Coherent (*Cube 660-60C*) has been used to produce the photon flux The output beam was accurately defocused with a plane-convex lens and then attenuated using different filter as to obtain the desired low photon flux. A mirror was used to guide the beam on the sample active area. The photon source so obtained was accurately measured with the Coherent Laser Power Meter *FieldMate* before starting with the current acquisition. The photocurrents were registered with the *HP4156B* analyzer using an integration time of 1s.

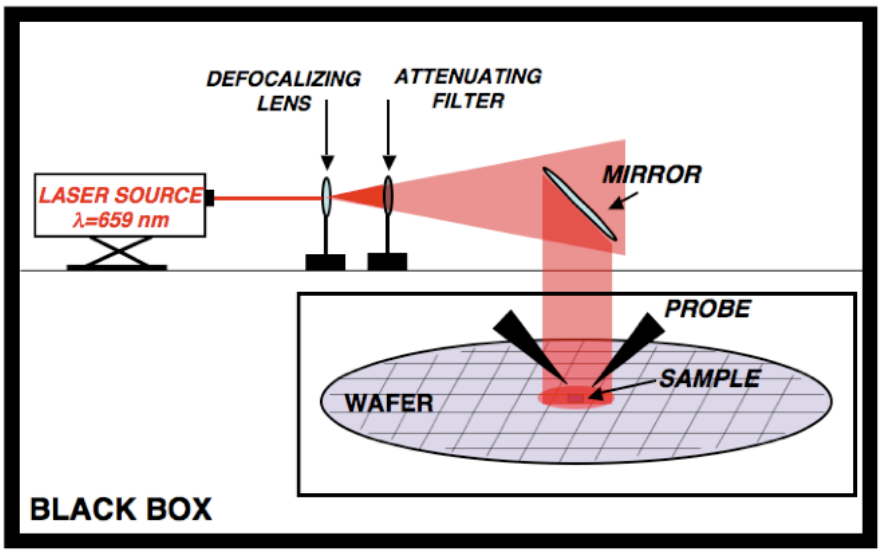

Figure 2.25: *Schematic setup of the photocurrent measurement.*

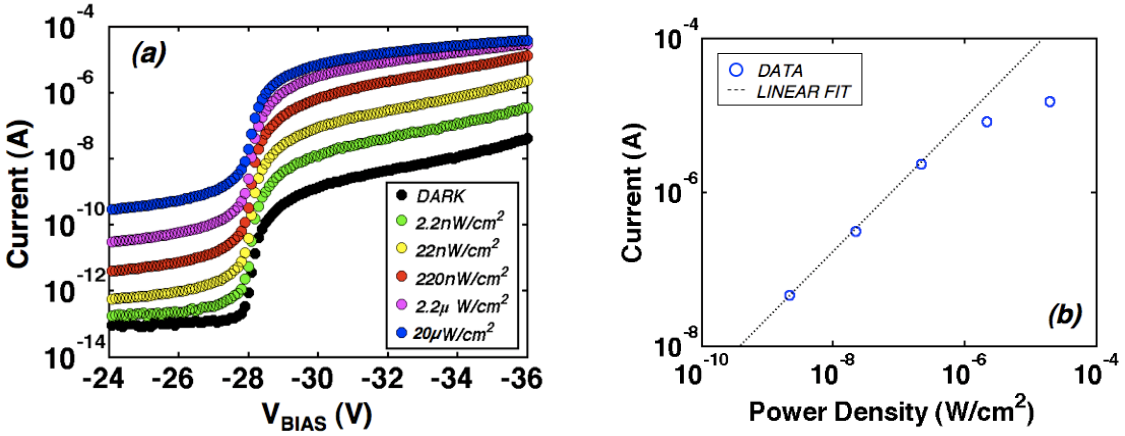

Figure 2.26: *(a) Dark and photo-current of a pixel at room temperature and for different photon fluxes. (b) Photocurrent of a pixel at room temperature for V_{BIAS}=-32V versus photon flux.*

Even in this case, measurements were performed on wafer level using a Cascade Microtech Probe Station *11000*. The whole experimental system was shielded from visible external electromagnetic wave by means of a dark plastic cover.

Figure 2.26 (a) reports an example of I-V characteristics of a SiPM pixel under illumination with laser light at flux levels ranging from 2.2 nW/cm^2 up to 22 μW/cm^2 at room temperature. Above the breakdown voltage the pixel operates linearly up to about 200 nW/cm^2, and a tendency to signal saturation is evident above such intensity. This conclusion is confirmed by Figure 2.26 (b), where the photocurrent-current for V_{BIAS}=-32 V as a function of the optical power density is reported. The data perfectly follow a linear trend up to 220nW/cm^2, while they deviates for higher values. The saturation above 220 nW/cm^2 is well explained by dead time effects, of the order of 200 ns as shown in Figure 2.21, where it is clear that the fully recharge of the device is obtained for times of 200 ns or above.

Data such as those of Figure 2.26 (a) allowed us to evaluate *G* by using Equation 2.3.6. By assuming a *QE* value of 0.15 at the 659 nm laser wavelength [71] we determine *G*. A further evidence of the signal saturation when the photon flux is too high is provided by the results of Figure 2.27, where the gain versus voltage at the different optical power densities is shown.

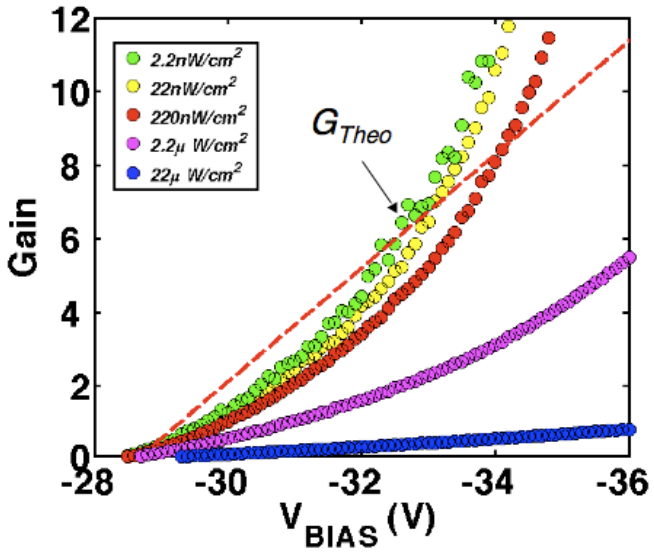

Figure 2.27: *Gain of a pixel at room temperature as a function of the photon flux. The dashed red line is the theoretical gain of Equation 2.3.3.*

At low fluxes (up to 220nW/cm2) all the curves collapse into one, it is the maximum gain achievable from the device. Increasing the flux the gain decreases, similarly to what we observed for short integration times in the transient current mode. Low gains exhibit an approximately linear trend, while the maximum gain shows a quadratic behaviour, as already observed in the previous section for a fully independent method of measurement.

The same trend was measured as a function of temperature, as shown in Figure 2.28. The breakdown voltage, V_{BD}, increases with temperature, hence a rigid shift of the gain curve with temperature is observed going from -27V at -25°C up to -30 V at 65°C.

Finally, in Figure 2.29 the comparison between the results obtained with the two methods are shown. Once again, the dashed line is the theoretical gain evaluated at 25°C, given by Equation 2.3.3. It is evident a surprisingly good match between G and G at high voltage, while a small difference is observed at low voltages, while small difference are observed at low voltage. The small differences at low voltage in the gain are probably due to differences in the triggering probability P_t. In fact the gain measured with the transient current mode does

not takes into account the triggering probability, because the current is measured only when the avalanche takes place, i.e. Pt=100%. On the other hand, in the photocurrent measurement mode, the probabilities involved in the physical phenomenon, the probability for a photon to generate an e-h couple and the triggering probability, are included in the *QE* term. The gain is then the real device devices gain. At high voltages the gain obtained with the two methods has the same value because the triggering probability tends to 100%.

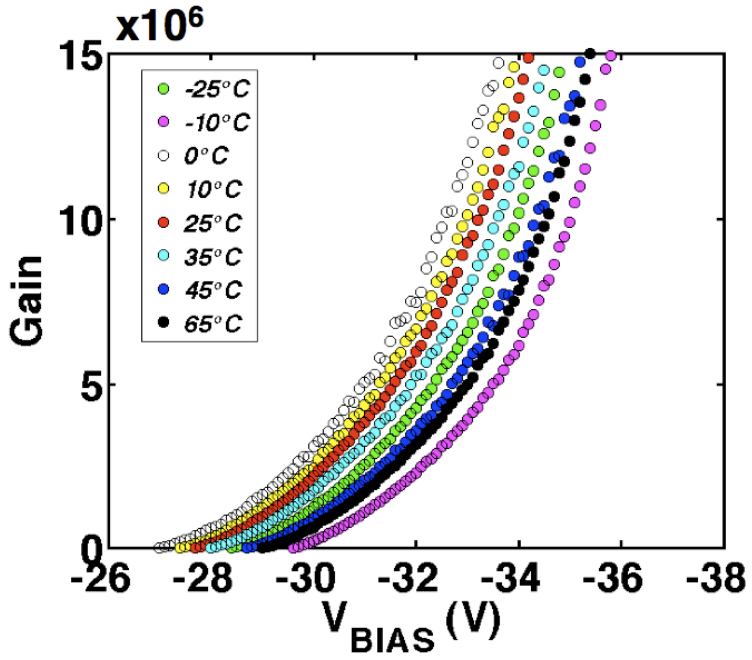

Figure 2.28: *Gain as a function of the voltage and temperature of a single pixel measured in accordance with Equation 2.3.6.*

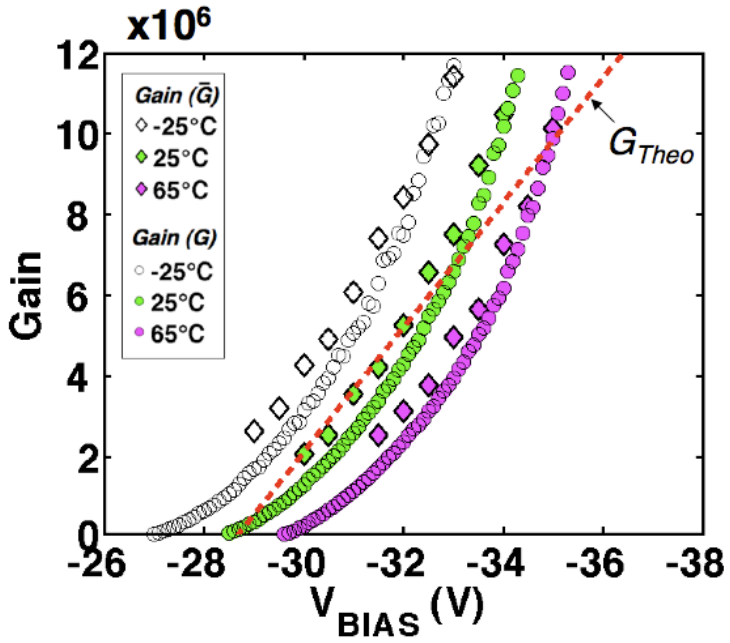

Figure 2.29: *Comparison between the gain* $\overline{G}$ *measured from the transient current and the gain G measured from the photocurrent at -25°C, 25°C and 65°C. Dashed red line is the* G_{Theo} *given by Equation 2.3.3.*

§ 2.4 Dark Currents

We now proceed in our analysis by discussing the dark count frequency f_{DC} of a single pixel. In § 2.2 we showed that dark current above 0°C is dominated by the diffusion physical mechanism (see Figure 2.17 b). This implies that there are no SHR centres in concentration such to dominate the dark current. Ideally, when there are no SRH centre generating free carriers in the detection volume, the dark count frequency per unity are, $\tilde{f}_{DC}$, should at least be equal to the frequency (per unity area) of free carrier injection from the quasi-neutral boundaries. In an n^+p junction it is given by the well known expression:

$$\tilde{f}_{Diff} = \frac{D_n n_{p0}}{L_n} = \frac{n_i^2 D_n}{N_A L_n} = \frac{n_i^2}{N_A}\sqrt{\frac{D_n}{\tau_n}} \qquad (2.4.1)$$

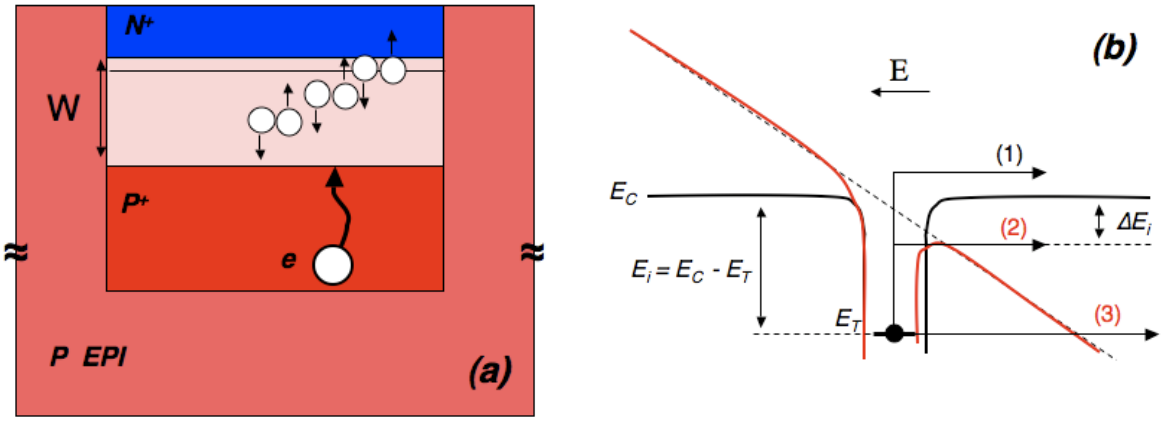

Figure 2.30: *(a) Diffusion of an electron into the depleted region. (b) (1) Thermal generation of an electron from a SHR centre, (2) Thermal generation from a SHR centre assisted by Poole-Frenkel effect, (3) tunneling of an electron from a SHR centre.*

where $D_n = \sqrt{L_n \tau_n}$ is the diffusion constant of the minority electron carrier in the p side, given by the square root of the diffusion length L_n time the lifetime τ_n of electron, n_{p0} is the electron densities at the depletion layer boundary $\sim n_i^2/N_A$, n_i is the intrinsic carrier concentration, N_a is the dopant concentration at the depletion layer boundary of the enrichment. A schematic of the physical mechanism is shown in Figure 2.30a.

As previously mentioned, the data already discussed in Figure 2.17 indicate that at temperatures above 0°C the current follows the diffusion model, with an activation energy equal to the Si band gap. Below 0°C the data differ from the model, hence to fit such temperature range, other physical phenomena must be introduced. If we also assume the presence of defects, the related emission frequency per unity area could be due to:

(1) SHR thermal generation (Equation 2.4.2),

(2) SHR thermal generation assisted by the Poole-Frenkel effect (Equation 2.4.3)

(3) Tunneling (Equation 2.4.4).

$$\tilde{f} = N_{def} \cdot W \cdot \gamma \cdot \sigma \cdot T^2 \cdot \exp\left(-\frac{E_i}{kT}\right) \tag{2.4.2}$$

$$\tilde{f} = N_{def} \cdot W \cdot \gamma \cdot \sigma \cdot T^2 \cdot \exp\left(-\frac{E_i - \Delta E_i}{kT}\right) \tag{2.4.3}$$

$$\tilde{f} = N_{def} \cdot W \cdot \frac{q\mathrm{E}}{4(2m^* E_i)^{1/2}} \cdot \exp\left(-\frac{4}{3}\frac{(2m^*)^{1/2}(E_i)^{3/2}}{q\hbar\mathrm{E}}\right) \tag{2.4.4}$$

where N_{def} is the defect concentration, W the depletion layer width, γ an universal constant, σ the defect cross-section, E_i the defect ionization energy, $\Delta E_i = q^2\mathrm{E}/\pi\varepsilon_{Si}$ the lowering of the barrier height due to the high field effect E, T the temperature, q the electron charge, m* the electron mass, k the Boltzmann constant, and $\hbar$ the Planck constant /2π. The different phenomena are summarized in Figure 2.30 b.

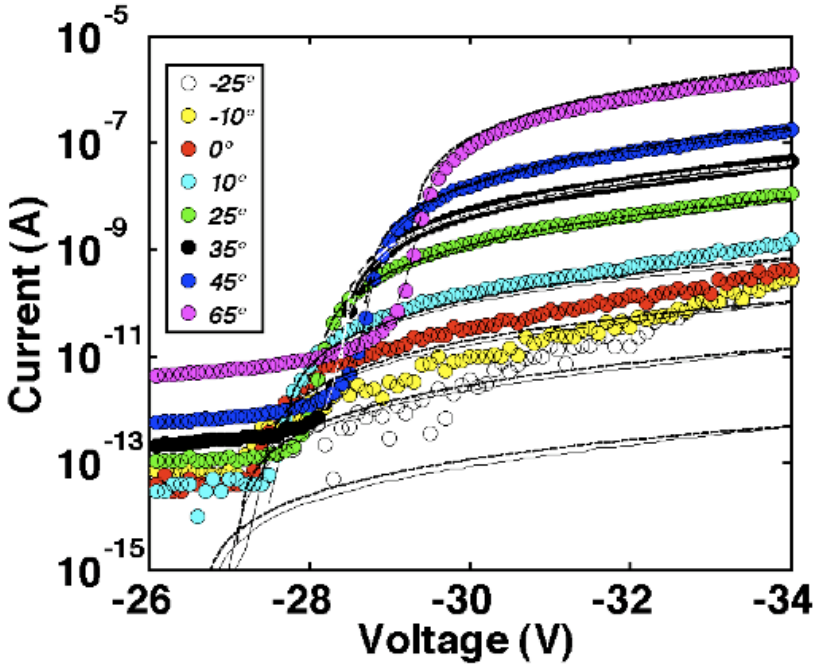

Figure 2.30: *Dark current versus temperature (circle) and simulated dark current using Equation 2.2.2 and Equation 2.4.1 (diffusion of minority carrier) with the gain given by the transient current mode (dashed line) and by the photocurrent mode (solid line).*

If we assume that the current is due only to the diffusion mechanism, the data will be well fitted above 0°C, as shown in Figure 2.31 (data points from 10°C light blue, up to 65°C, data in magenta) where the experimental data are compared to the simulation result.
Simulations were performed using Equation 2.2.2 assuming for G the values obtained with the transient current method (dashed line) and the photocurrent method (solid line) already reported in Figure 2.29 and the frequency calculated from Equation 2.4.1 using τ_n as fit parameter

Data below 10°C need the introduction of a different physical mechanism to be fitted. The data analysis of the device discussed in this thesis allow us to conclude that the dark current in this temperature region is ruled by the combination of the diffusion term (Equation 2.4.1) and the SHR thermal generation assisted by Poole-Frenkel (Equation 2.4.3). In particular the data are well fitted by using the SHR thermal generation for the slowest process between electron and hole generation. Figure 2.32 reports the comparison between the experimental IV (data

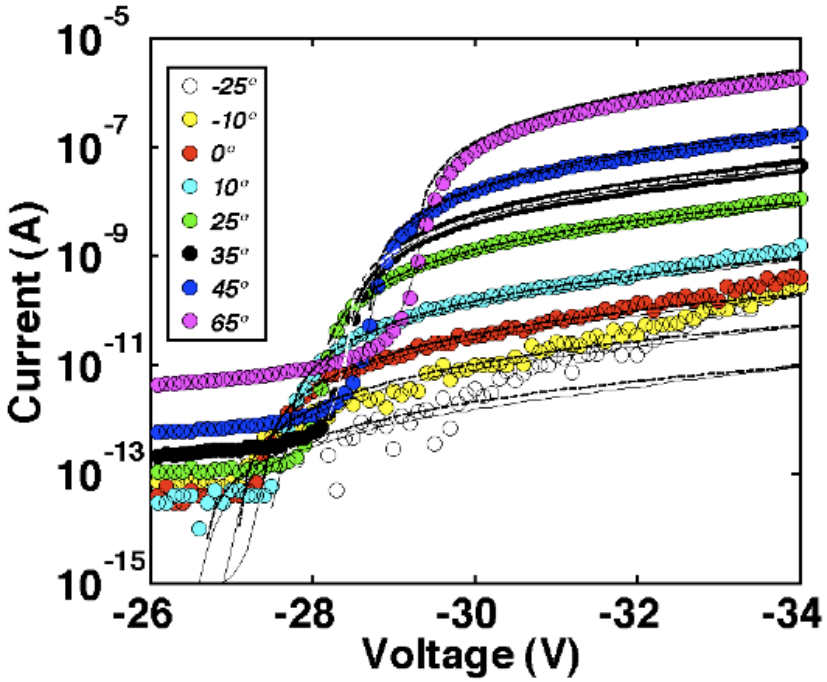

Figure 2.32: *Dark current versus temperature (circles) and simulated dark current using Equation 2.2.2 and with the gain given by the transient current mode (dashed line) and by the photocurrent mode (solid line).*

points) and the simulation performing using the to mechanism previously introduced. The agreement between data and model is extremely good. We fit the data both as a function of voltage and as a function of temperature by assuming the well known relationship between carrier diffusivity and mobility, and τ_n = 3.4·10^{-8} s, μ_n=1100 cm^2/Vs, and N_A= 1.5e16 cm^{-3} in Equation 2.4.1, while for thermal generation with Poole-Frenkel effects Equation 2.4.3 we have assumed N_{def} = 1·10^9 cm^{-3}, E_i = 0.57 eV, σ = 1.6·10^{-15} cm^2, with the universal constant γ = 1.78e21 cm^{-2}s^{-2}K^{-2} as reported in [85]. The remarkable agreement between data and model is obtained by assuming quite reasonable values of the fit parameters, and this suggests that the present model catches quite well the behavior of the device. We also note that these devices present a dark current only limited by carrier diffusion already at quite low temperatures, essentially almost at 0 °C, indicating a remarkably low SRH defect concentration (of the order of 1·10^9 cm^{-3}) as clearly summarized in Figure 2.33 where the dark

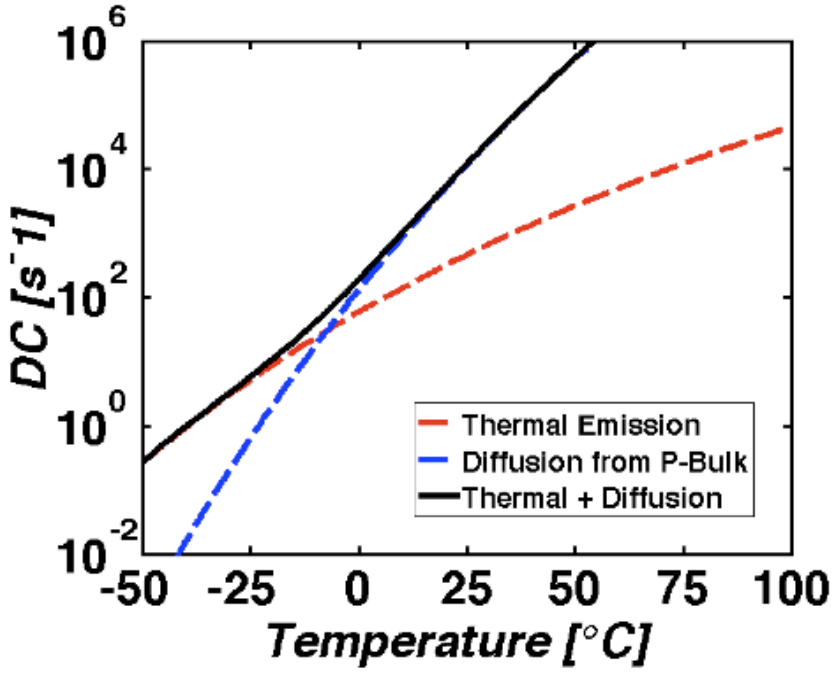

Figure 2.33: *Dark count at 10% OV as a function of temperature given by simulation results.*

count ($f_{DC}=\tilde{f}_{DC}\cdot A_d$) as a function of the temperature at 10%OV is shown. In Figure 2.33 thermal generation with Poole-Frenkel effect is red dashed line, diffusion from bulk is the blue dashed line while black solid line is the combination of the two mechanisms.

§ 2.6 Conclusion

In this chapter we reported on the fabrication of Silicon Photomultipliers. A brief description of the fabrication details for the devices produced by STMicroelectronics is reported in section. 2.1. We performed electrical measurements on SiPM single cells. The gain was determined using two independent methods: monitoring the charge and monitoring the current under a known light flux. Interesting results were obtained. The gain, determined with two independent methods exhibits similar behaviour as a function of the overvoltage, showing a superlinear trend. The gain value at a given OV is strongly dependent on the acquisition window in the transient current method, while it depends on the photon flux in the photocurrent method, reaching its maximum in the transient current mode at 4τR, 220 ns in our case. The maximum photon flux to obtain the maximum gain is 220 nW/cm2. Both values are determined at room temperature. Using the experimental results, described in section 2.2 (I-V curves) and 2.3 (gain determination), we proposed a physical model on the dark count rate of SiPM single pixels. The model suggests that the two main causes of dark count are the carrier diffusion from the bulk and the SHR thermal generation assisted by Poole-Frenkel effect. The model was compared to the experimental data. It fits nicely the data and demonstrates that state-of-the-art SiPM can have at room temperature a dark current rate limited only by carrier diffusion.

Chapter 3

SiPM characterization

In the previous chapter, the basic characteristics of the single pixel were detailed studied and a simple model, well fitting the data in the operation region, was proposed. Aim of this chapter was the study of the full device, a matrix having 64x64 cells connected in parallel. Since the pre-commercial device is quite complex, the study was preformed in steps of increasing difficulty. SiPM with 5x5, 10x10, 20x20 and, finally, 64x64 pixels were electrically characterized following the same flow followed in Chapter 2 for the single cell characterization. Moreover, since the devices were fabricated on 6 inches wafers, a particular attention was devoted to the study of the fabrication issues, such as uniformity on the wafer. This last study is fundamental for a commercial product, since the yield must be as high as possible.

§ 3.1 Fabrication Details

As already mentioned for the single pixels, the SiPMs were produced by the R&D Sensor Team of the STMicroelectronics site in Catania. The wafer has two main features: six stripes in light gray in Figure 3.1, and 31 square regions (dark gray in Figure 3.1). The stripes contain all the test devices, where the single pixels and the small area SiPMs sit, while the square regions are the SiPMs 64×64 pixels.

The test pattern contains the single pixels (center of the multicell), and a full set of small area SiPMs. In Figure 3.2 an enlarged picture of the test pattern, designed by STMicroelectronics, is shown. In particular, on the up right and on the down left corners the 5×5 pixels SiPM devices are fabricated. The difference between the two devices is the presence (up) or absence (down) of the optical trenches (see later). The 10×10 pixels SiPM devices are on the center left (without trenches) and right (with trenches) of the test pattern,

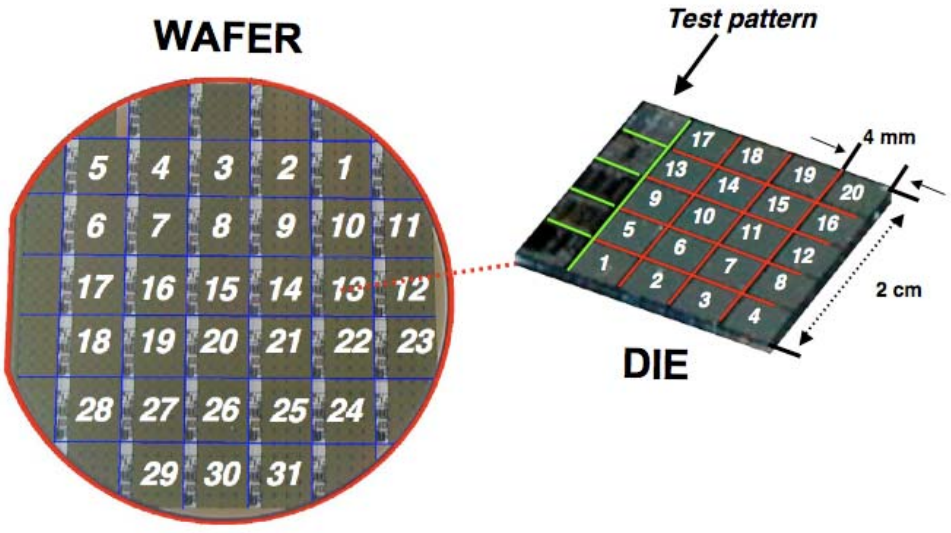

Figure 3.1: *Picture of a wafer. The SiPM have been indicated with progressive numbers to facilitate the analysis*

while the 20×20 pixels SiPMs are on the up left (without trenches) and down right (with trenches) corners. The presence of devices with an increasing number of pixels is helpful to infer on statistical issues, i.e. more frequent in devices with a larger number of cells, while the two sets of devices, with and without trenches, are needed to understand if the trenches presence is needed for all sizes. It should be reminded that the trenches fabrication implies a reduction of the fill factor and an increase in the fabrication costs (more masks and fabrication steps). On the other hand the trenches presence may reduce cross talk issues.

The wafer area is filled with the 64×64 SiPM devices. On a single wafer, only 31 devices are fabricated (due to their large area), hence it is fundamental that their characteristics are the

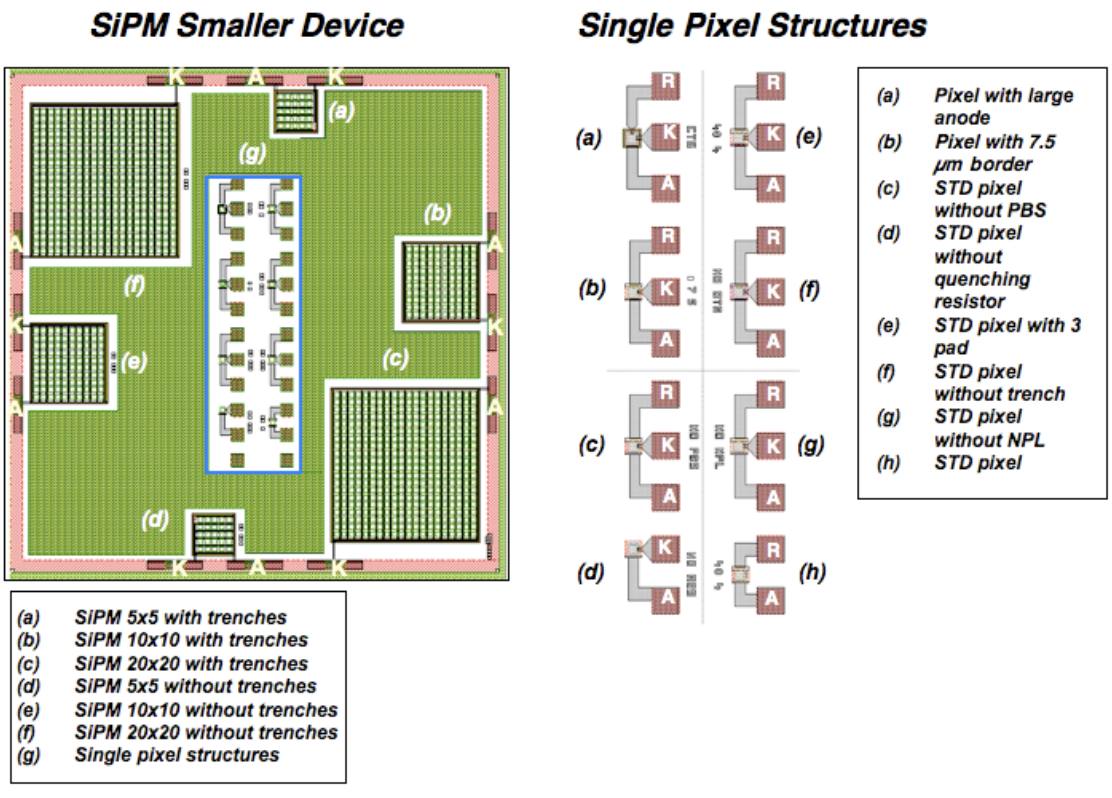

Figure 3.2: *Layout of the test pattern produced by ST Microelectronics, the different arrays are indicated.*

same within a low error. Their active area is ~6.5 mm^2, the pad size is 450µm×60µm and the pad pich is 650µm. A picture of the SiPM is shown in Figure 3.3.

Finally, three single cells are also fabricated in each SiPM (top left of Figure 3.3). One is a standard cell, as those described in the previous chapter, one is a standard cell without the quenching resistance, and the third is a standard pixel with a thick metal layer on top (blind cell). They are useful tests to validate the fabrication process.

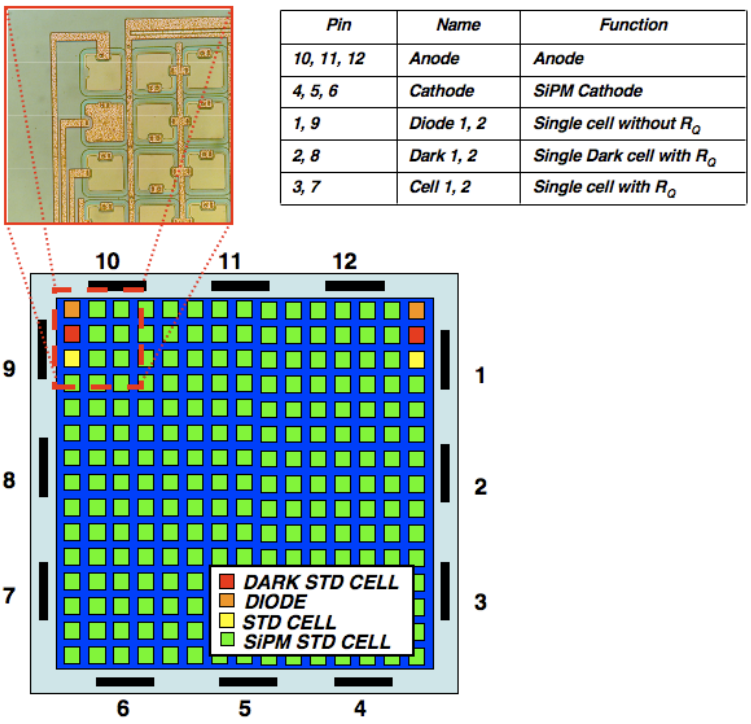

Pin	Name	Function
10, 11, 12	Anode	Anode
4, 5, 6	Cathode	SiPM Cathode
1, 9	Diode 1, 2	Single cell without R_Q
2, 8	Dark 1, 2	Single Dark cell with R_Q
3, 7	Cell 1, 2	Single cell with R_Q

Figure 3.3: *Layout of a preproduction SiPM. On the right the picture of a device corner is reported. It shows the single cells region.*

§ 3.2 Small SiPM array electrical characterization

The devices are n (n=25, 100, 400) p-n silicon diodes with a large resistor in series, connected in parallel. As already justified for single pixels, useful information on the device operation are obtained from the basic current-voltage (I-V) characteristics in dark condition. The static electrical characterization was performed, also in this case, on wafer level using the same instrumentation described in § 2.2.

— 3.2.1 Forward Current

All the different devices sitting in the test pattern were fully characterized. In this section I will briefly describe the measurements preformed on the 5x5 arrays without trenches and I'll show the results for all the devices stressing compare and contrast for each set.

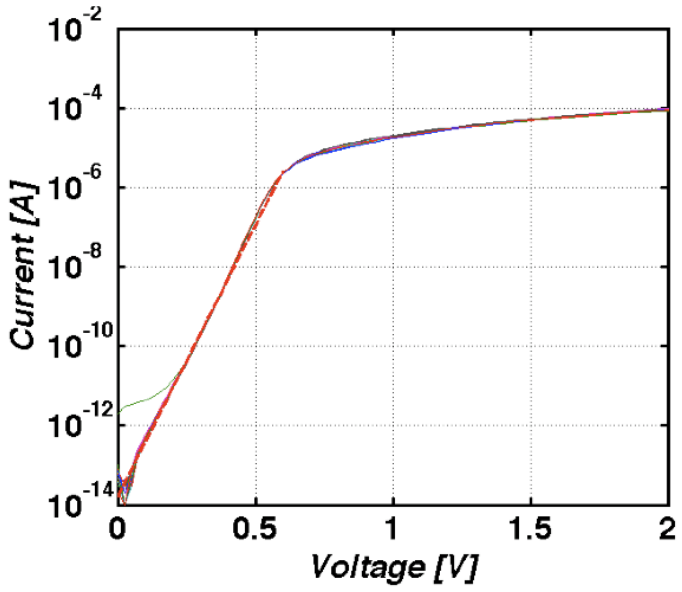

Figure 3.4: *Measured forward current at 25°C of a 5x5 array without trenches. Two different current regimes with respect to the applied voltage are clearly identifiable.*

The forward IV measurements on all the 5x5 devices of the test patterns belonging to the same wafer are reported in Figure 3.4. Two main results can be carried out from this set of measurements: the ideality factor value (and its error bar) and the uniformity on the wafer. The forward current trend is the same already observed for the single cell and the three region can be identified: the first, where the instrumentation sensitivity is the real limit, is smaller than for the single cell; the second, where the ideality factor can be calculated ranges up to 0.5 V; and the third, where the diode resistance effect is visible, ranges from 0.6 up to 2 V. The ideality factor has a value of 1.35, as determined using the same procedure reported in —2.2.1 The third region, has a trend probably due to a parasitic Schottky sitting at the anode metal contact (see —2.2.1 for a full explanation).

The second interesting information that can be inferred from the data is the uniformity of the behavior on the full wafer.

To this purpose, the *n* values of all the devices measured are reported in an histogram in Figure 3.5 (a) . To better clarify the uniformity issue, the results are also reported in Figure 3.5 (b), where the sites are shown using false colors to represent the different *n* values (red is

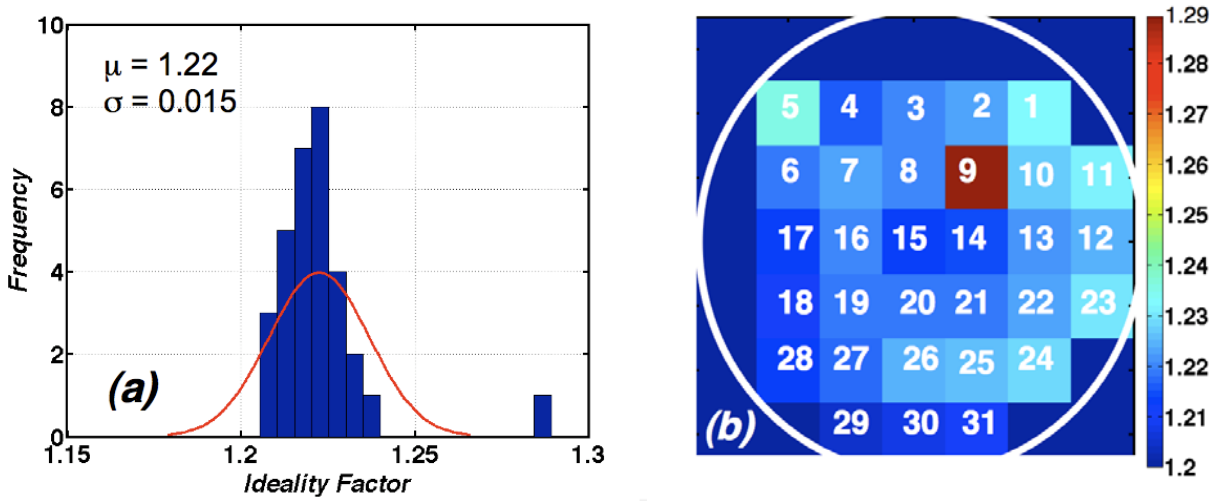

Figure 3.5: *Ideality factor distribution: (a) histogram; (b) Distribution on the wafer. The n value is reported in false colors, being the lowest value in dark blue (1.2) and the highest value in dark red (1.29).*

The highest, blue the lowest). The data clearly indicate that the most lateral devices have an ideality factor higher, suggesting an uniformity issue during the fabrication process. This analysis is quite important if it is considered that the yield on the wafer must be as high as possible in a commercial device.

As already mentioned, similar analysis were performed on all the devices and the results are shown in Figure 3.6.

The ideality factor is almost the same for all the arrays with trenches, suggesting two main results: *i*. increasing the number of devices in the cell the devices physics remains the same, *ii*. there is no big technological issue, since the devices characteristics are the same even if the number of component progressively increases.

Finally, the current voltage data for all the devices with trenches in the test pattern are summarized in Figure 3.7. In the same figure the IV of the single cell is also reported for

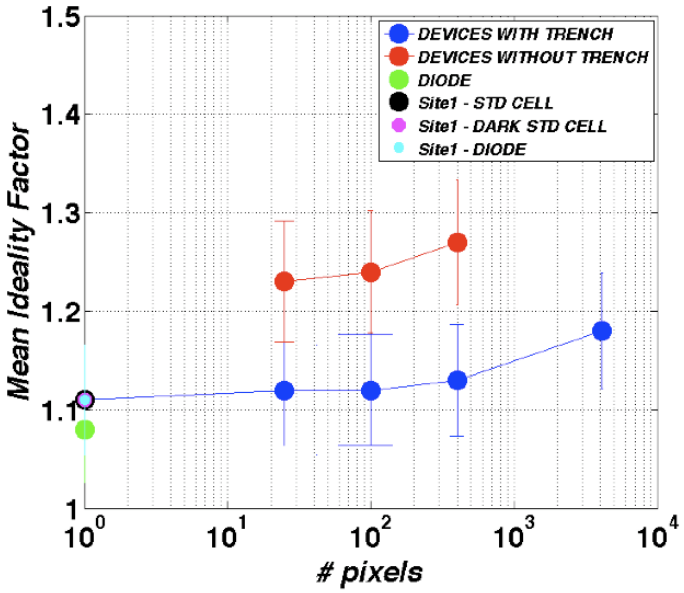

Figure 3.6: *Ideality factor as a function of the pixel number of the single pixel (black, magenta, and yellow points) and the arrays (blue points) up to the full SiPM.*

comparison (blue line). The forward current increases as a function of the number of cells going from $1.2x10^{-8}$A (@ 0.5V) in the single cell, to $5x10^{-7}$ V, 1.8×10^{-6} V, 6.2×10^{-6} V, 2.7×10^{-5} V for the 5×5, 10×10, 20×20 and 64x64 devices, respectively.

It is interesting to observe the difference in the forward current of devices with and without trenches. The most striking difference is in the region where the parasitic resistance takes place. It is more evident in the 20×20 arrays, hence the comparison for 20×20 arrays with (green lines) and without (red lines) trenches is shown in Figure 3.8. The Figure clearly shows that at high voltages, in the region where the Schottky diode presence is evident, the devices without trenches have a larger spread in the values. We believe this difference is due to the better electrical insulation that is obtained in devices where the cells are optically insulated by the trenches.

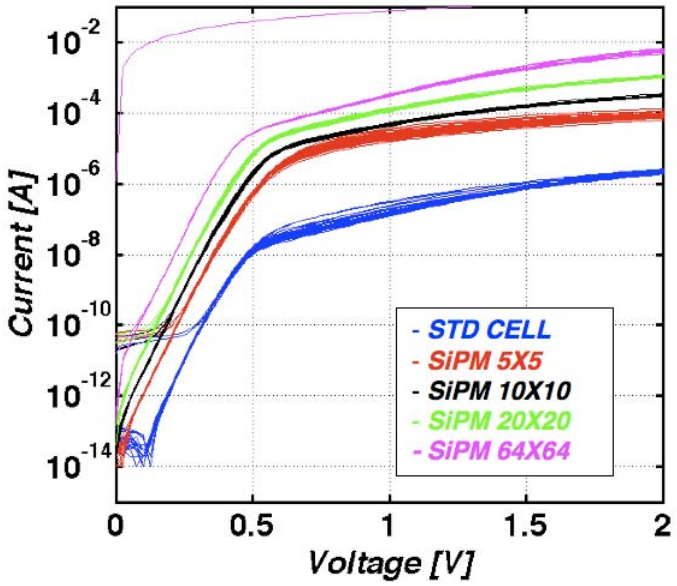

Figure 3.7: *Measured forward current at 25°C of the standard cell (blue lines), the arrays 5×5 (red lines), 10×10 (black lines), 20×20 (green lines) and the full SiPM (64×64 magenta lines) with trenches.*

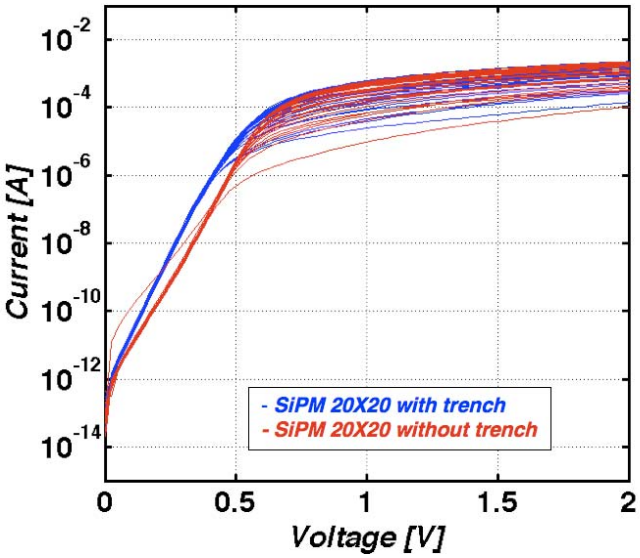

Figure 3.8: *Measured forward current at 25°C of the 20x20 arrays with (blue lines) and without (red lines) trenches.*

— 3.2.2 Reverse Current

More important was the characterization in reverse current of the same devices. Using the same procedure already reported in § 2.2, the reverse current from 0 up to -40 V was measured. The results for all the devices with trenches are shown in Figure 3.9. In the same figure the standard cell results are also reported (blue lines). As expected, the reverse current below breakdown increases with the number of cells connected in parallel, hence with the array dimensions.

The data allowed us to make interesting conclusions: the breakdown voltage does not change with the array dimensions, as expected if all the cells within the array are correctly working.

A more careful analysis was performed and, as already described for the forward currents, the breakdown voltage was measured for all the testing devices within the wafer. The results obtained for the 5x5 array without trenches are reported in Figure 3.10. The data indicates a

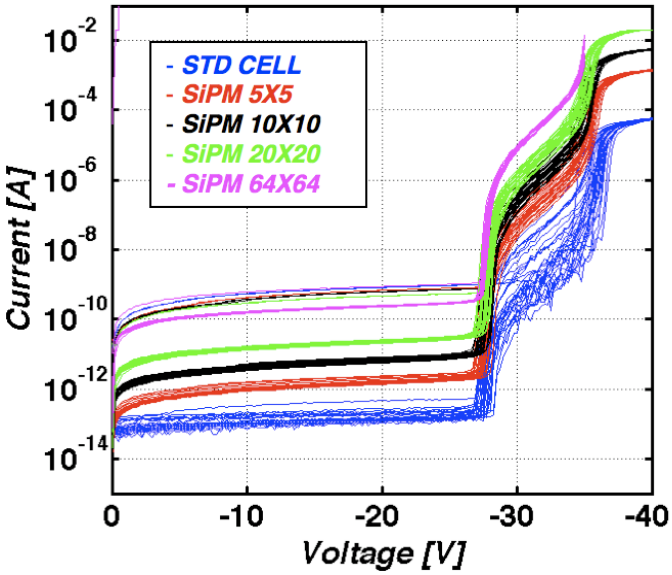

Figure 3.9: *Measured reverse current at 25°C of the standard cell (blue lines), the arrays 5×5 (red lines), 10×10 (black lines), 20×20 (green lines) and the full SiPM (64×64 magenta lines) with trenches.*

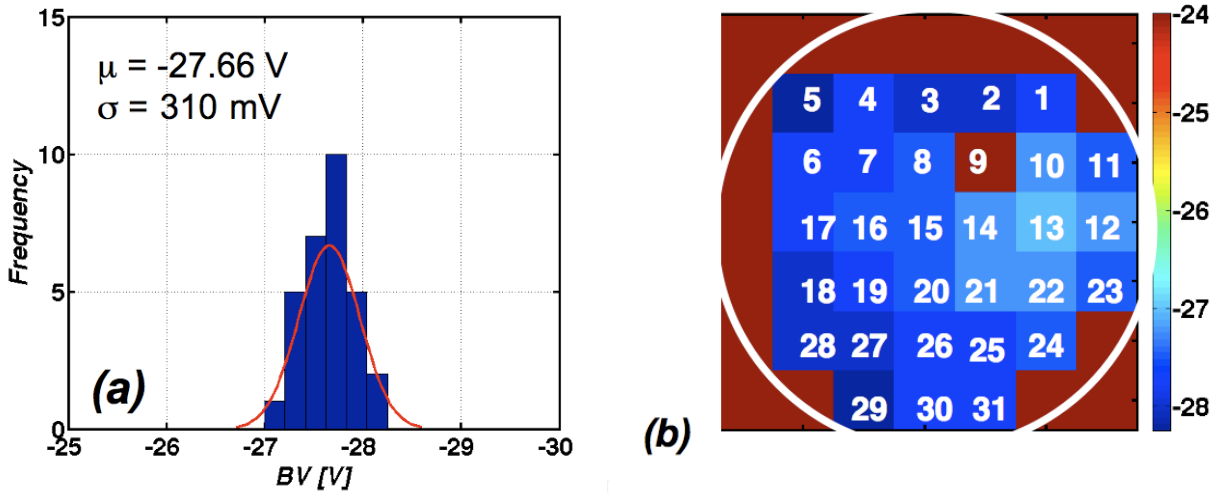

Figure 3.10: *Breakdown voltage distribution: (a) histogram; (b) Distribution on the wafer. The n value is reported in false colors, being the lowest value in dark red (~-24.0V) and the highest value in dark blue (~-28.0V).*

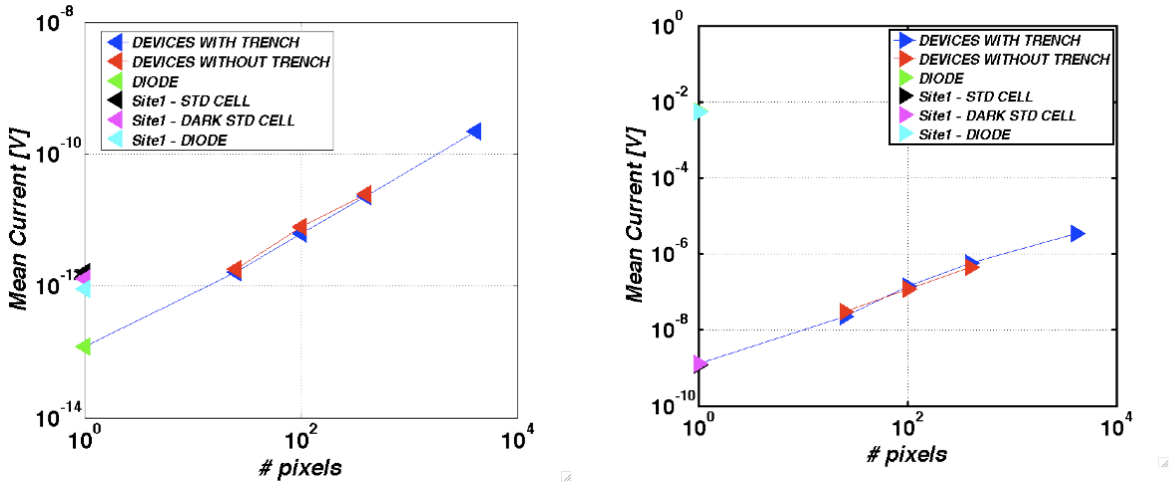

Figure 3.11: *(a) leakage current and (b) dark current distribution as a function of the pixel number of the single pixel (black, magenta, and yellow points) and the arrays (blue points) up to the full SiPM.*

spread around the average voltage of -27.7V. Both the histogram (Figure 3.10 (a)) and the distribution in the wafer (Figure 3.10 (b)) are reported in the same figure.

In particular, a comparison between the various devices can be made by considering the reverse current below breakdown (leakage current), i.e. at -20V, and above breakdown (dark current), i.e. -30V. The data for all the devices are summarized in Figure 3.11.

It is interesting to observe that both the leakage and the dark current increase with the device dimension, as already observed from the row data (Figure 3.9). A more detailed description of the results is provided in the next section, where the model developed for the single cell is applied to the arrays.

The most intriguing difference is between devices with and without trenches: as an example the I-V curves of the 20x20 devices with (red lines) and without (blue lines) trenches are compared in Figure 3.12.

As already observed in Figure 3.11, the leakage current for the two sets of devices is the same within the errors, and the dark count up to 30V is roughly the same as well. The most interesting part of the comparison is the voltage range between -30V and -40 V, that is the

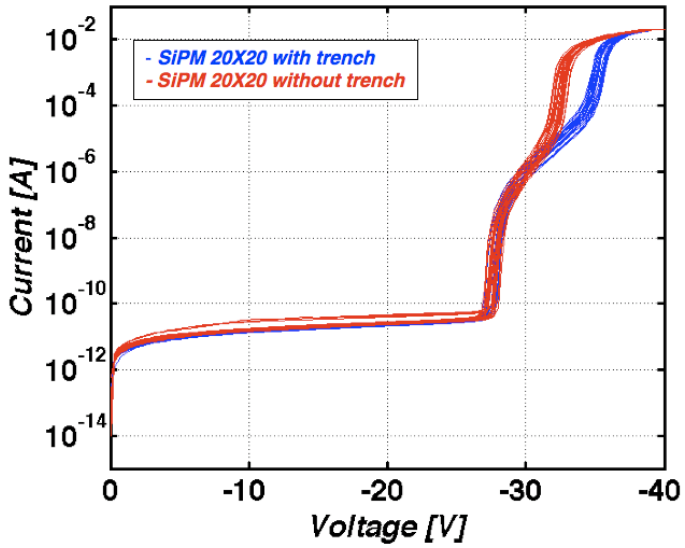

Figure 3.12: *Measured reverse current at 25°C for the 20x20 arrays with (blue lines) and without (red lines) trenches.*

region of operation. Devices without trenches exhibit a dark current much higher than the devices with trenches, almost two order of magnitude at -32 V (operating voltage). It is due to the crosstalk effect: when a single pixel goes in breakdown optical photons are generated and they will cause the breakdown of adjacent pixels, thus strongly increasing the dark count rate.

A nice confirmation of this hypothesis is provided by emission microscopy (Em.Mi) measurements performed on both devices. The Em.Mi results for a device opportunely designed are shown in Figure 3.13. The devices were fabricated with trenches only on the horizontal lines and each two lines. The image is the sum of two different images: the picture of the device and a false color images indicating the hot points. Where current flows (breakdown point) the point is hot and the image is red. The explanation of the results is obvious: where the trenches insulate the cells, the hot points do not propagate, while where there are no trenches each time a point becomes hot, also the adjacent cells go in breakdown.

Finally, Figure 3.14 summarizes the breakdown voltages for all devices, from the single cell up to the full device (64x64). The breakdown voltage deceases only for the full SiPM

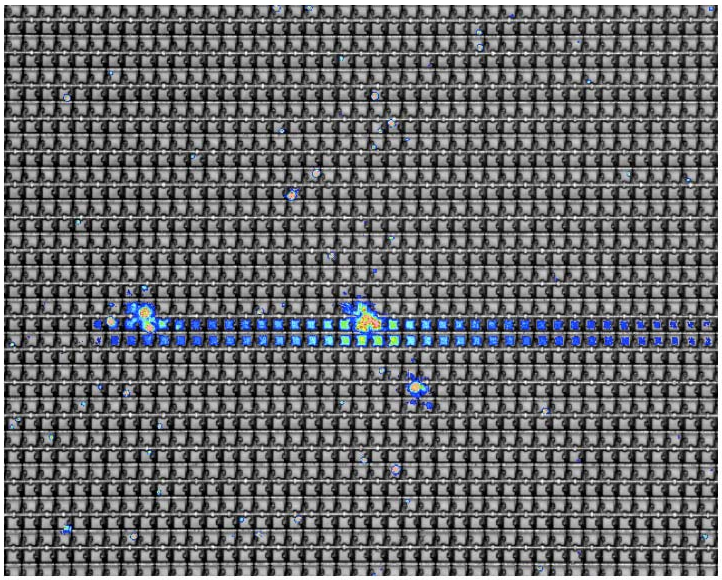

Figure 3.13: *Emission microscopy measurements at 25°C for the 20x20 arrays with (a) and without (b) trenches at V_{BIAS}=-32V.*

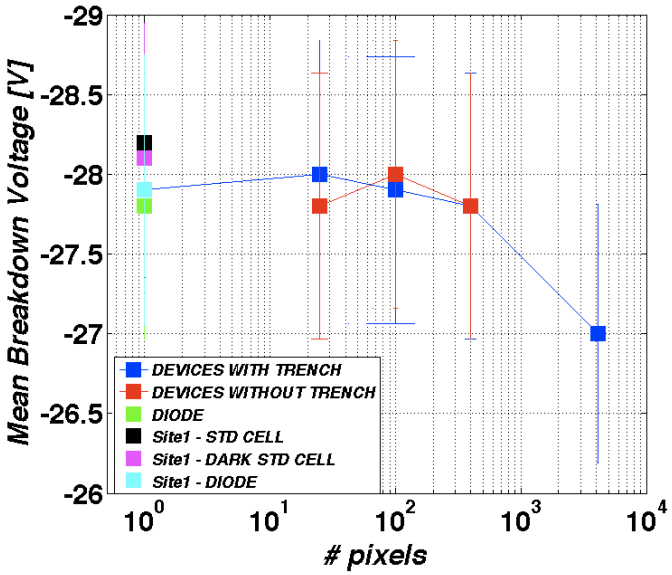

Figure 3.14: *Breakdown voltage as a function of the pixel number of the single pixel (black, magenta, and yellow points) and the arrays (blue points) up to the full SiPM.*

(64x64). The “early” breakdown experienced by the full array can be due to statistical issues. In fact, being the number of cells quite high, the probability that a single cell does not work properly increases, thus producing a reduction in the full device BV value.

§ 3.3 Dark current model: from single pixel to SiPM

The main conclusion of Chapter 2 is the definition of a model that succeed in explaining the voltage dependence of the dark count as a function of the device temperature. The results, data point and fit based on the model, are reported in Figure 2.32.

As already mentioned, the data are fitted assuming that the current is given by the Equation 2.2.2 here reported for clarity:

$$I_{DC} = q \cdot G \cdot \tilde{f} \cdot A_d \tag{3.3.1}$$

G is the gain measured using the two methods reported in Chapter 2 (transient current and photocurrent), $\tilde{f}$ is the dark count rate per cm^2 and A_d is the device effective area. Just to remind, the dark count frequency is provided by the combination of two physical phenomena: diffusion of minority carriers ($\tilde{f}_{Diff}$)from the bulk and SHR thermal generation assisted by Poole-frenkel effect ($\tilde{f}_{SHR-PF}$). In symbols:

$$\tilde{f} = \tilde{f}_{Diff} + \tilde{f}_{SHR-PF} \tag{3.3.2}$$

The model proposed well fits the single cell experimental data.

In this section we propose two simplified models, to extend the model described in Chapter 2 to full SiPM arrays. The first one, only assumes that the SiPM behaviour is provided by the same Equation 2.2.2 where the dark count frequency is the product of the frequencies of the 4096 cells. In symbols

$$I_{SiPM} = I_{DC} \cdot n_{pix} = q \cdot G \cdot \tilde{f} \cdot A_d \cdot n_{pix} \tag{3.3.3}$$

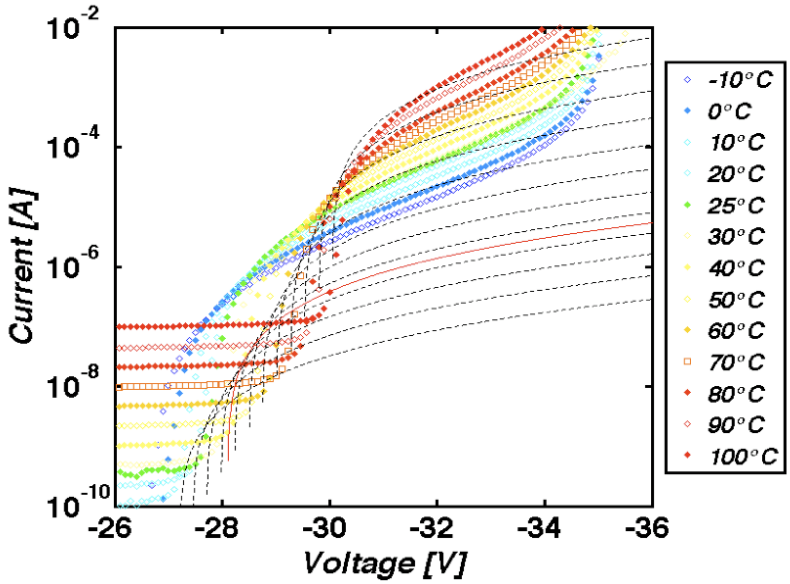

Figure 3.15: *Dark current versus temperature (circles) and simulated dark current using Equation 3.3.1 with the gain given by the transient current mode (dashed line)*

Where all the symbols have the same meaning already discussed. Figure 3.15 provides the comparison between the experimental data with this very simple model. The figure clearly shows that the experimental data (points in figure) are not well fitted by this model, suggesting that a more complex behaviour must be assumed.

It should be mentioned that the G was determined using the transient current mode, but the same results are obtained if the photocurrent mode is used (see § 2.3 for a more detailed discussion).

An improvement of the model is proposed suggesting that other phenomena take place. The main is the crosstalk probability, i.e. when a pixel goes trough the avalanche process triggers adjacent cells, others can be statistical defects fluctuation in the different cells. It should be reminded that the average defects concentration is very low, 1×10^{9} cm-3. It means that the single pixel, having a volume of 40x40x1 μm^3 has in average 1.6 defects. It is obvious that the differences between one and two defects will produce huge variation in the dark count rate. This effect should be considered by introducing a rare events statistics and a

Monte Carlo simulation. Further studies are in progress to correctly model these effects. Finally, even more than two cells can be simultaneously excited by the breakdown of a single cells (as an example see Figure 3.13).

In the simplified approach discussed hereafter it has been assumed that the crosstalk (every effect that causes the concomitant breakdown of two cells) introduces a probability of 10% to be added to the single cell dark count rate. Moreover, in this simplified model it is assumed that only a maximum of two pixels can breakdown at the same time. In symbols:

$$I_{SiPM} = q \cdot (G \cdot f \cdot A_d \cdot n_{pix} + 2 \cdot G \cdot PC) \tag{3.3.4}$$

Where PC is what we called crosstalk probability. The fit results are compared to the data in Figure 3.16. Still, the experimental data cannot be fully described by this model, suggesting

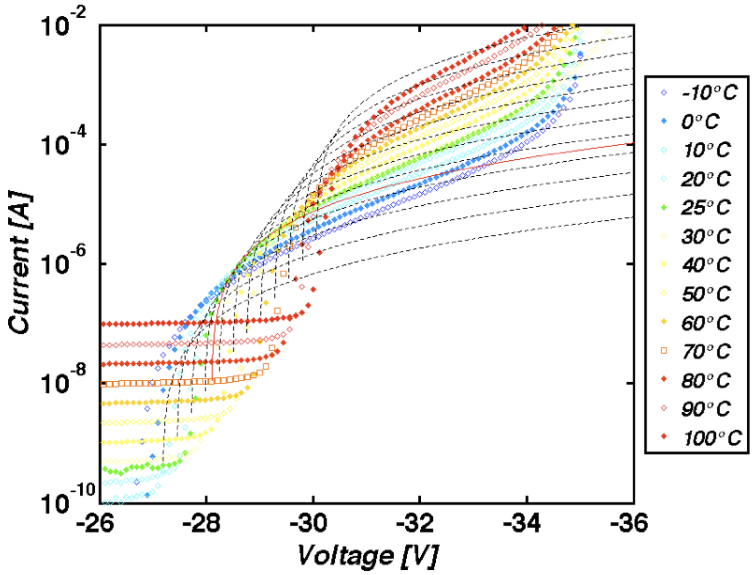

Figure 3.17: *Dark current versus temperature (circles) and simulated dark current using Equation 3.3.4 with the gain given by the transient current mode (dashed line. The green data points are and the solid red line refers to experimental data and simulation at room temperature, respectively.*

that the more complex model must be implemented, nevertheless the simulation results are closer to the experimental data than the previous model. In particular, room temperature data (green data points) are successfully fitted by the simulation (red solid line) up to -31V.

§ 3.4 Technological issues

As previously mentioned, the SiPM fabrication process needs a full control of the fabrication flow and of a high yield over the full wafer area. In order to have a properly working full array, all the single components forming it need to work exactly in the same way, i.e. they must have the same breakdown voltage, leakage and dark currents, etc. The importance of it becomes clear from the inspection of Figure 3.16. Figure 3.16 (a) shows the I-V curves in reverse voltage of single cells (blue lines), 10×10 (red lines), and 64×64 SiPM on a single wafer. Single pixels exhibit a breakdown voltage of -28.9 V with a standard deviation of 200mV. 10×10 and 64×64 SiPM exhibit a strong current increase with a

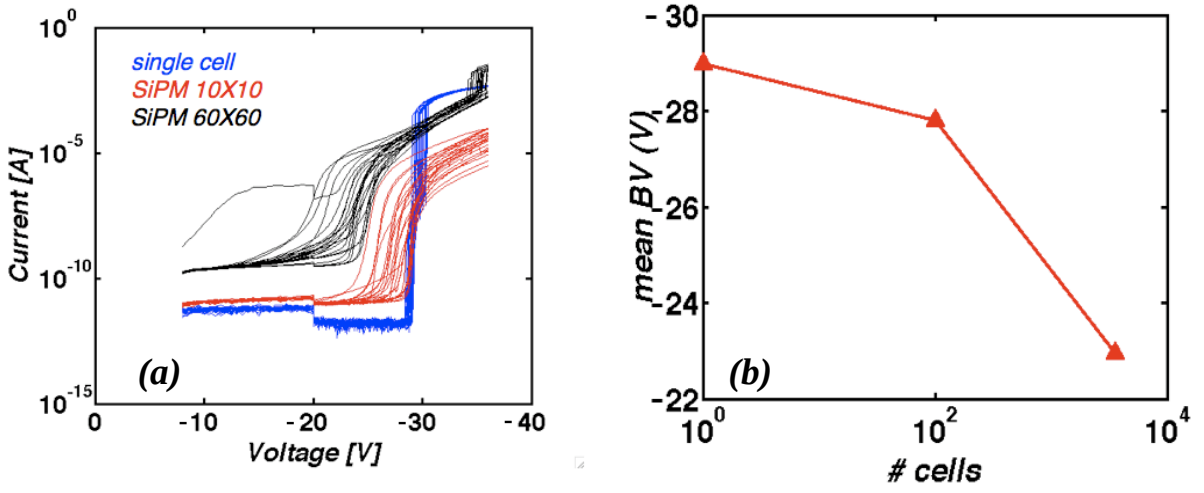

Figure 3.16: *(a) Reverse voltage characteristics of single cells (blue lines), 100 pixel (red lines) and 3600 pixel (black lines) SiPM on the same wafer. (b) Average value of the breakdown voltage as a function of the pixel number.*

breakdown voltage of -27.3V and -22.8 V, respectively. Also the standard deviation increases with the number of pixels going from 1.3 V up to 3V for the largest devices. Figure 3.16 (b) shows the average breakdown voltage as a function of the pixel number.

In order to understand this anomalous behaviour the SiPM working principle must be reminded. A schematic of the simplified circuit is shown in Figure 3.17. n single cells are connected in parallel, each one with its quenching resistance in series. The device current is the sum of the currents coming from the n branches of the circuit. Now, if a cell (the *k* one) has a fabrication defect, i.e. a lower breakdown voltage, the BV of the full device (BV_{SiPM}) will be driven by the breakdown voltage of the single cell (BV^{k}_{cell}) that will behave as a resistor for voltages above its breakdown voltage, i.e. $BV_{SiPM} = BV^{k}_{cell}$.

The total current (I_{SiPM}) will be the sum of the currents of the working pixels and the defective pixel. In symbols:

$$I_{SiPM} = I_k + \sum I^{i}_{cell} \tag{3.4.1}$$

The proposed model was been verified by studying the I-V of a wide number of single cells and arrays of all dimensions. The results for the single cells are shown in Figure 3.18.

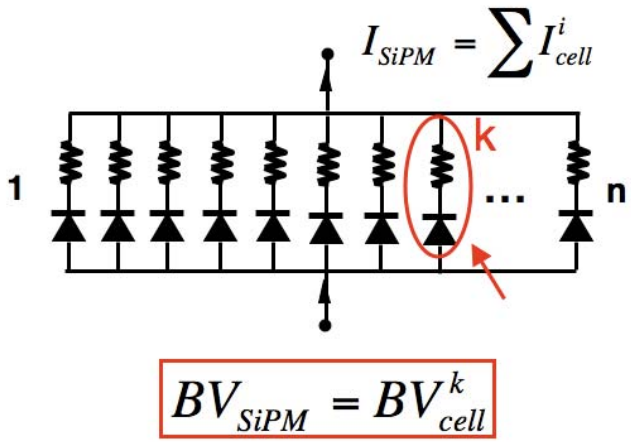

Figure 3.17: *Simplified schematic of the SiPM circuit and proposed physical model.*

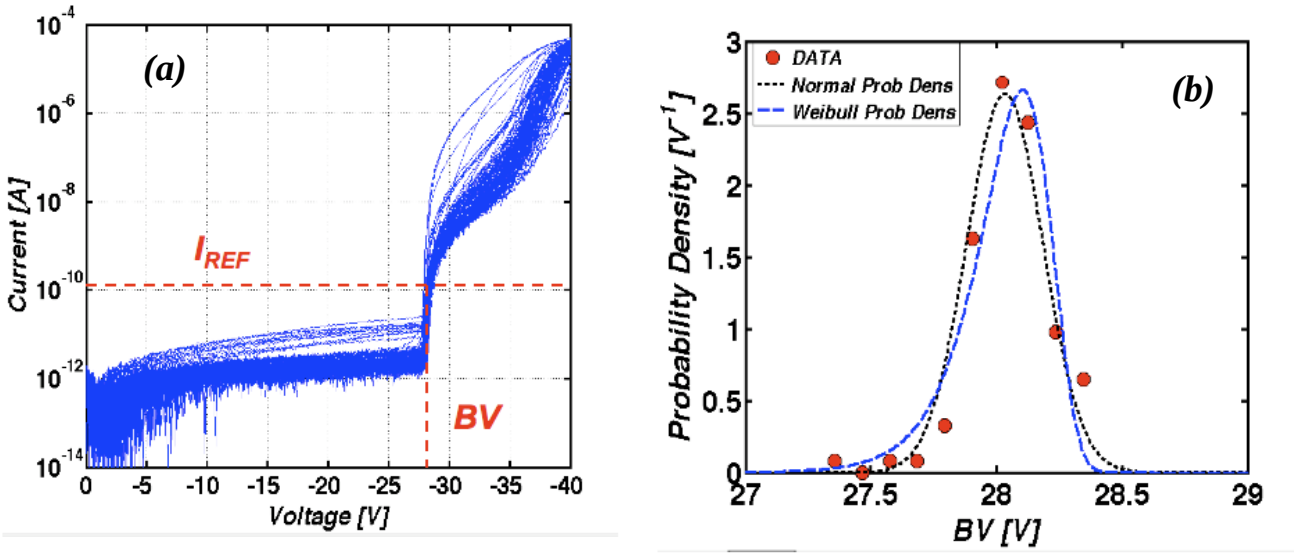

Figure 3.18: *(a) Reverse voltage characteristics of 200 single pixels at room temperature (b) Probability density of the breakdown voltage and statistical fit. The black line is a normal distribution having an average value μ=28.03 V and standard deviation σ=15mV while the blue line is a Weibull distribution having parameters: α=20.01 V and β=203 V^{-1}.*

In particular, Figure 3.18 (a) shows the I-V curves, acquired at room temperature, of 200 single cells belonging to the same wafer. In this case, the breakdown voltage is almost the same, as summarized in Figure 3.18 (b) where the breakdown probability as a function of the voltage is reported

The data points indicate an average breakdown voltage of -28.0V and the experimental points range between -27.4V and -28.4V. The experimental data (red dots in Figure 3.18 (b)) have been compared to two different Monte Carlo distributions: a normal distribution having an average value of μ=28.03 V and standard deviation σ=15mV (dashed black line); and a Weibull distribution having parameters α=20.01 V and β=203 V^{-1} (dashed blue line). Both statistics well fit the experimental data, but the error is lower for the normal distribution, suggesting this is the best way to represent the data.

A similar comparison (experimental data *vs* statistical distribution) has been performed as a function of the increasing number of cells, up to the full SiPM device. The experimental

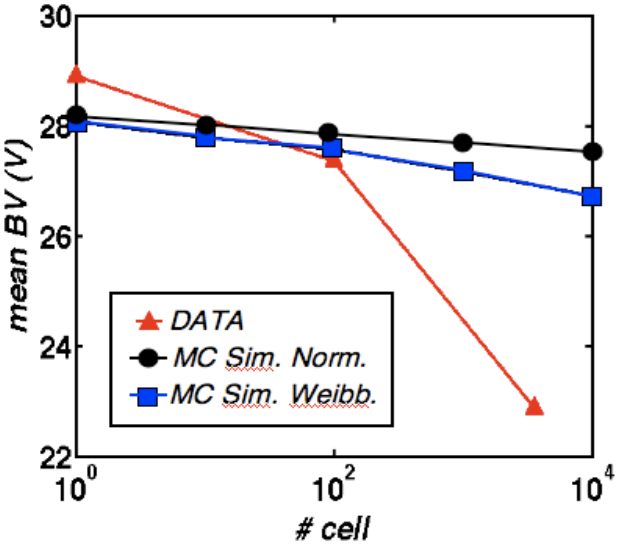

Figure 3.19: *Mean break down voltage as a function of the number of cells (red triangles) compared with Monte Carlo simulations: normal (black dots) and of Weibull (blue squares). The solid line are only guide to the eye.*

breakdown voltages (red triangles) as a function of the pixel number are summarized in Figure 3.19 and compared to both distributions: normal (black dots) and Weibull (blue squares). The data clearly indicate that the statistics well fit the experimental data up to 100 pixels (10×10 arrays) while they fail for larger devices.

In order to understand the large difference between the experimental data and the simulation results for large devices, Em.Mi. measurements were carried out. I-V characteristics of the full SiPM (64×64 pixels) were performed and the results are shown in Figure 3.20 (a).

Even if the I-V curve is similar to those already observed for single cells, it exhibits a breakdown voltage of -18V, much lower than expected. The single cell BV (-28.5 V) is reported as a vertical dashed line in the same figure. Em.Mi analysis were performed using a reverse voltage of -25V (red dot on the I-v curve of Figure 3.20 (a)) that causes a leakage current of 44 μA, lower than the single cell value at breakdown. Em.Mi. images clearly

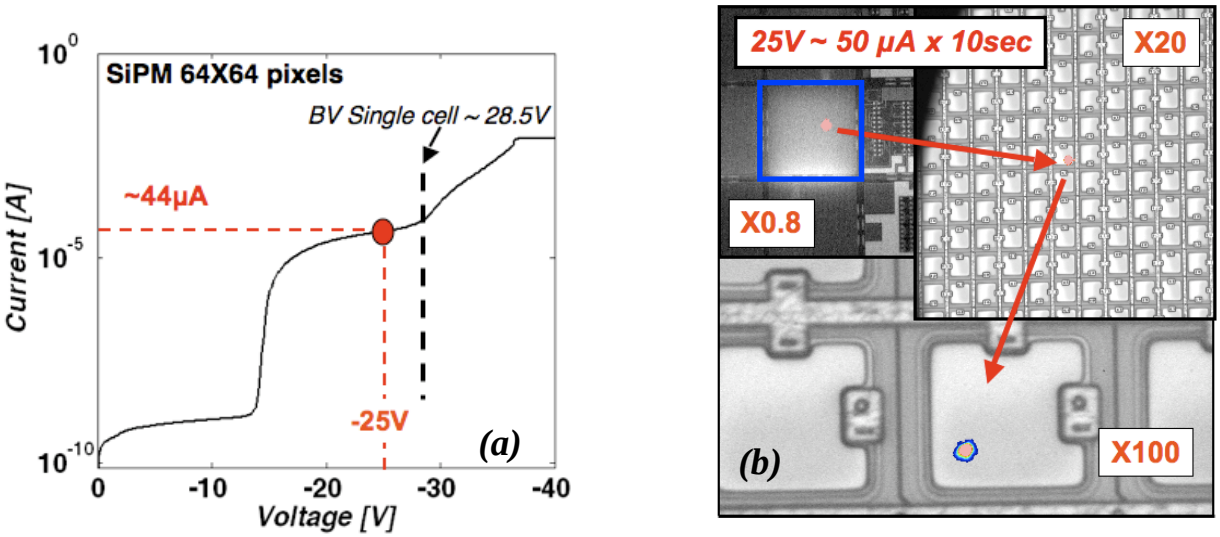

Figure 3.20: *(a) reverse voltage characteristic at room temperature of a SiPM having 64×64 pixels with an area of 40×40 μm². The red dot in figure shows the bias voltage used for the Em.Mi measurements, the dashed black vertical line is the average breakdown voltage for single pixels. (b) Em.Mi. images of the sample described in (a) for a reverse bias of -25V and an acquisition time of 10 s, using three enlargements (×0.8, ×20, ×100): the first (blue square) describes the SiPM area and allows to define a single hot point. The other enlargements clearly show that the hot point is within a single pixel.*

indicate the presence of an hot point (see Figure 3.20 (b) ×100), i.e. all the current flowing through the device is localized in that point, within the active area of a single pixel. The results strongly suggest that the spread observed in the BV of large arrays could be due to the failure of a single pixel within the device array.

A confirmation of this hypothesis is provided by the results shown in Figure 3.21, where the breakdown voltage probability density for arrays of different dimension (5×5, 10×10, 20×20), belonging to the same wafer, is reported. In particular, Figure 3.21 a shows the probability density of breakdown voltage for SiPM with 25 (blue histogram), 100 (red histogram), 400 (green histogram) pixels within a single wafer and Figure 3.21 (b) the probability density normalized to the number of pixels of breakdown voltage for the same devices. The data clearly indicate a progressive reduction of the breakdown voltage when the

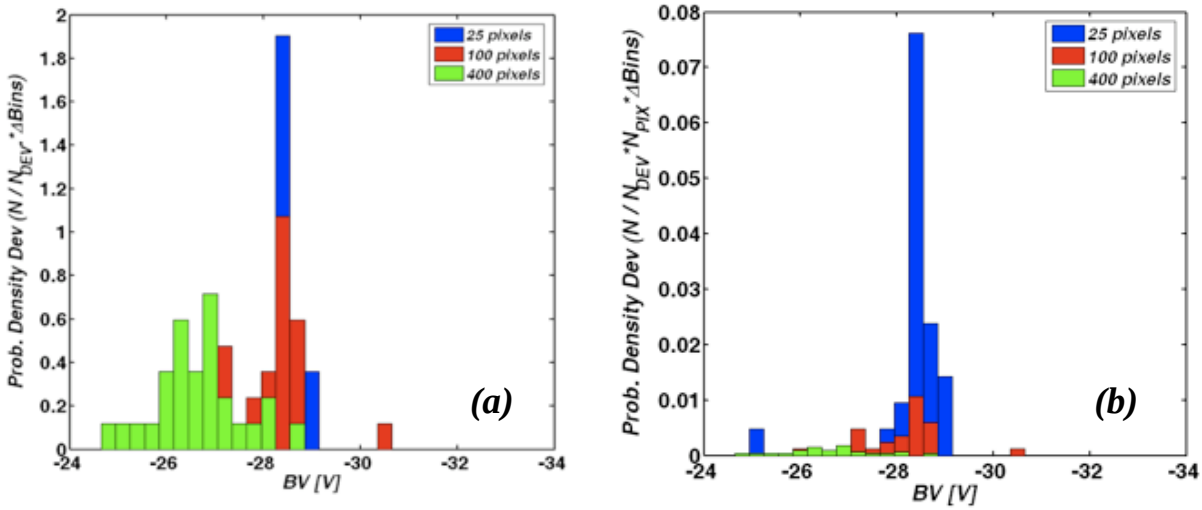

Figure 3.21: *(a) Probability density of breakdown voltage for SiPM with 25, 100, 400 pixels within a single wafer. (b) Probability density normalized to the number of pixels of breakdown voltage for the same devices of (a).*

number of pixels increases. The inspection of Figure 3.21 (b) suggests that all data can be explained using the same physical mechanisms. Nevertheless, as already observed, the early breakdown of a single pixel within the array is not enough to fully explain the large devices behaviour. Our hypothesis is that the defects causing single pixels early breakdown are originated during the fabrication process of large devices. In fact, is could explain why Monte Carlo simulations discussed earlier in this section, fail in the description of large arrays breakdown behaviour.

In order to understand the failure mechanism, dark current and current under illumination measurements were carried out on both the best and the worst device for each array dimension (5×5, 10×10, 20×20 pixels). Some of the results are compared in Figure 3.22. In particular, Figure 3.22 (a) shows the I-V characteristic of a good 5×5 array (i.e. with a BV close to the single cell BV value) in dark (magenta line) and under illumination (red line) at room temperature. Light presence modifies the I-V characteristics only above breakdown, i.e. in the device operative region. Quite different is the situation in a bad device. The BV in this case in -25 V, quite lower than the single cell and there is no visible difference between dark

and light conditions (green and blue lines, respectively). Figure 3.22 (b), shows the dark currents are acquired with the oscilloscope at a reverse voltage of -32V for both devices: the good one (magenta line) and the bad one (green line). The Figure inspection allowed us to conclude that:

1. The maximum peak height with respect to the offset is the same for both devices, 40 μA, suggesting that both devices experience the same overvoltage, hence both devices behave as they both had the same breakdown voltage.
2. the offset is strongly different in the two cases. In fact, the bad device exhibits an offset current of 40 μA. It implies that the devices experience a constant current flow (leakage) over imposed of the dark current spot-like events.

Similar results were obtained for all the arrays studies. As an example in Figure 3.22 (c) and d, the same analysis just discussed is reported for a 20×20 device. The devices behave exactly in the same way: the worst device exhibits a constant current flowing regardless of the dark count rate. The only difference with the 5×5 arrays is the offset current value. In this case it is of 70 μA, almost double than the current recorded in the 5×5 devices. The higher current could be due to an increase in the hot points number, i.e. more pixels have an early breakdown, or to the presence of the same number of hot points that allow a larger current flow.

Full devices, arrays having 64×64 pixels, exhibit a more complex behaviour since it was not possible to find a "best" device. A typical I-V characteristic is shown in Figure 3.23. It shows a breakdown voltage below -25V. The comparison between dark current (magenta line) and current under illumination (red line) shows, at -28V, a slight difference, enhanced in the inset of the same figure, where a zoom of that region is shown. The two curves perfectly overlap in the range -25V ÷ -28V.

The technological issue was solved introducing two main innovations. The substrate doping: it was n-type in the technology described in this section , while it is p-type in the best technology (described in the rest of this chapter). The second innovation was the

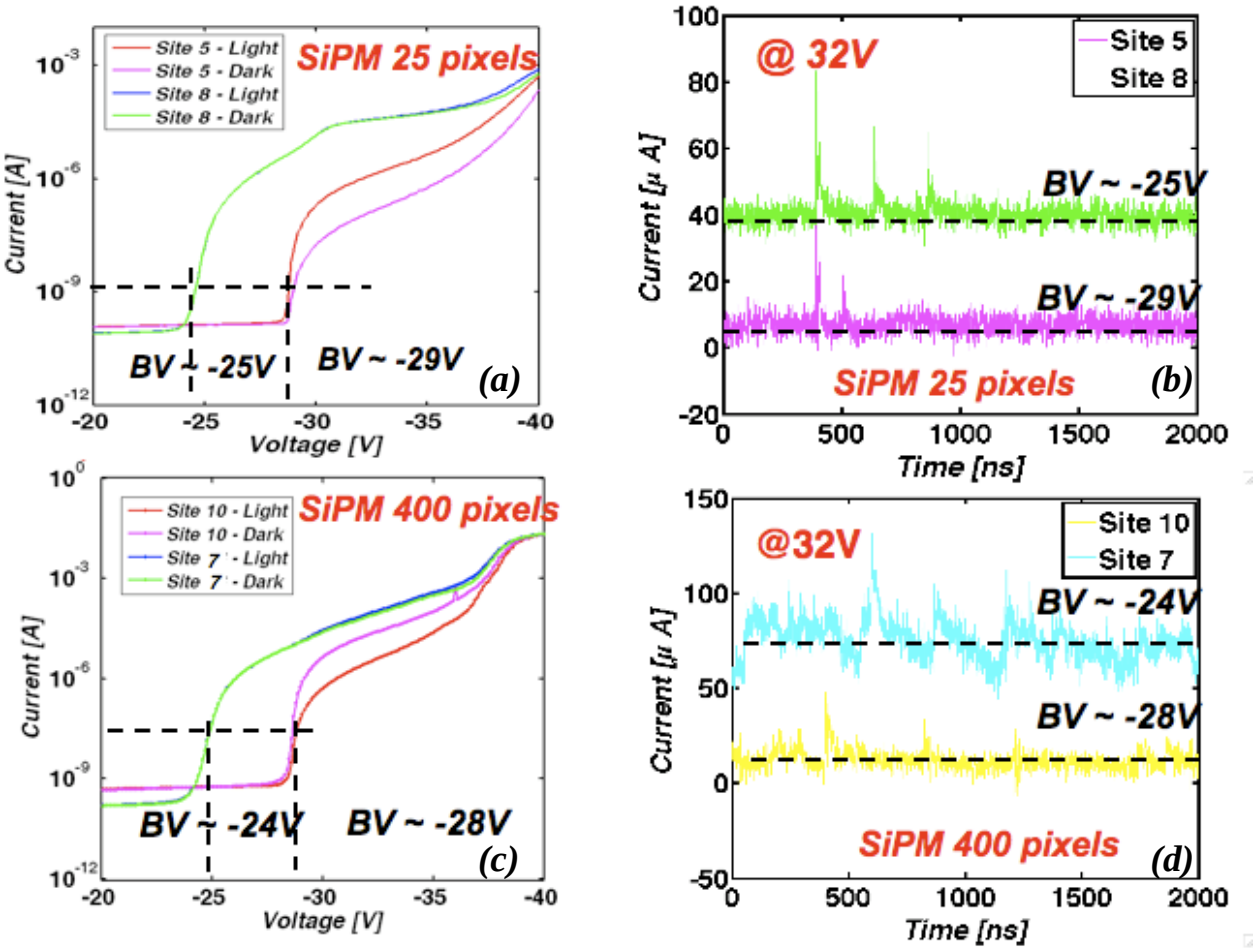

Figure 3.22: *(a) Reverse current characteristics in dark and under illumination of two SiPMs with 5×5 pixel having different BV. The site 5 is the best device, while site 8 is the worst one. (b) Current versus time acquired under a constant bias of -32V for the same devices described in (a). (c) reverse current characteristics in dark and under illumination of two SiPMs with 20×20 pixel having different BV. The site 10 is the best device, while site 7 is the worst one. (b) Current versus time acquired under a constant bias of -32V for the same devices described in (a).*

implementation of trenches all around each cell. It completely optically insulates each pixel. The results are shown in § 3.2 and § 3.3.

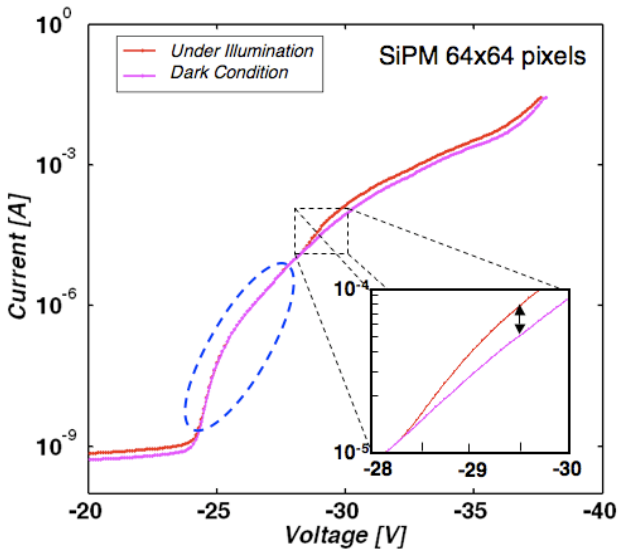

Figure 3.23: *Reverse current characteristics in dark (magenta line) and under illumination (red line) for a SiPM having 64×64 cells.*

§ 3.5 Other devices: the Hamamatsu MPPC

As mentioned in Chapter 1 STMicroelectronics is not the only SiPM producer. The first producer in the world is the Hamamatsu Photonics. For this reason Hamamatsu commercial SiPM were bought and characterized.

The Hamamatsu devices, named Multi-Pixels Photon Counter (MPPC) exhibit an avalanche breakdown at -69V, a voltage much higher than the devices already characterized (SiPM by ST). Both contact in these devices are on the front and the single pixels are p+n junctions (ST junctions are n+p). Figure 3.24 (a) shows a Hamamatsu MPCC having a full area of 9mm2 within its package. In order to understand the device dimension, it is placed on a 1€ Cent coin. Figure 3.24 (b) shows a closer picture of the same device with an enlargement showing the single pixel. The image inspection shows that the layout is much simpler than ST SiPMs one.

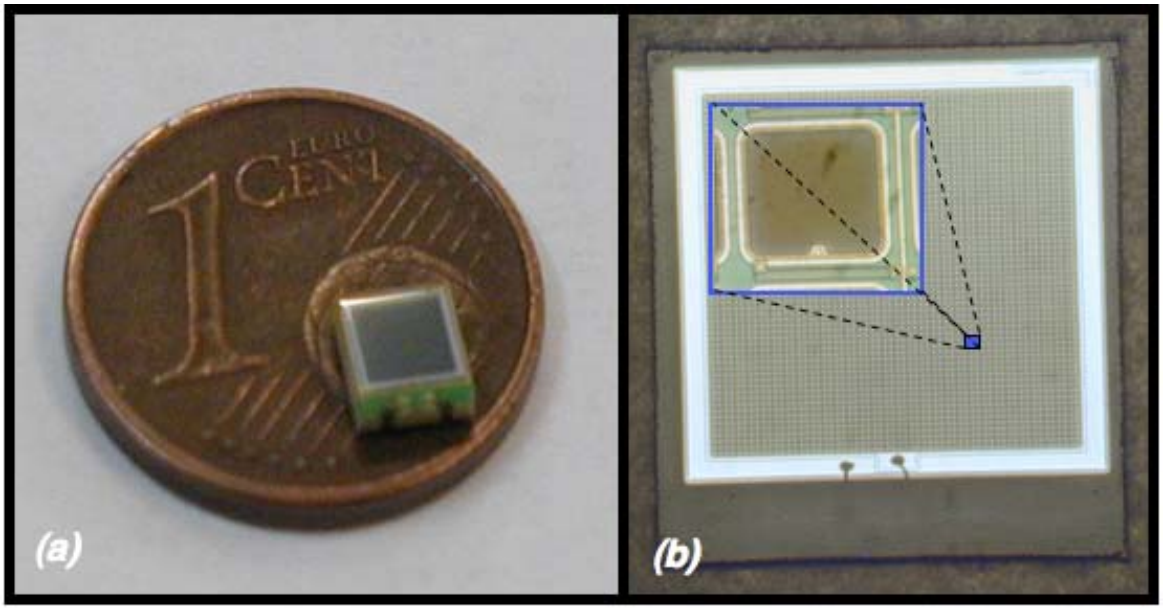

Figure 3.24: *(a) Picture of the Hamamatsu Multi-Pixels Photon Counter (MPPC) S10931-050P. the devices is given by the parallel of 3600 pixels having an area of 50 μm × 50 μm each, thus providing a total active area of 9mm^2. (b) Picture of the device described in (a) and enlargement of one pixel.*

The CNR-IMM bought three different devices:

1. the MPCC **S10931-050P** is the largest, it is a multi-pixels having an active area of 9mm2. It is composed by 3600 pixels having an area of 50 μm × 50 μm each.
2. The device **S10362-050P** has an active area of 1 mm2, provided by 400 pixels having an area of 50 μm × 50 μm each
3. the device **S10362-025P**, has an active area of 1 mm2 provided by 1600 pixels having an area of 25 μm × 25 μm each.

Figure 3.25 shows the I-V characteristics of the three multi-pixels just described. In particular, Figure 3.25 (a) shows the forward voltage and Figure 3.25 (b) the reverse voltage characteristics of the three devices.

The data inspection reveals that currents does not linearly increase with the devices area. Breakdown voltage is -69 V for all the devices. The leakage and dark current values are

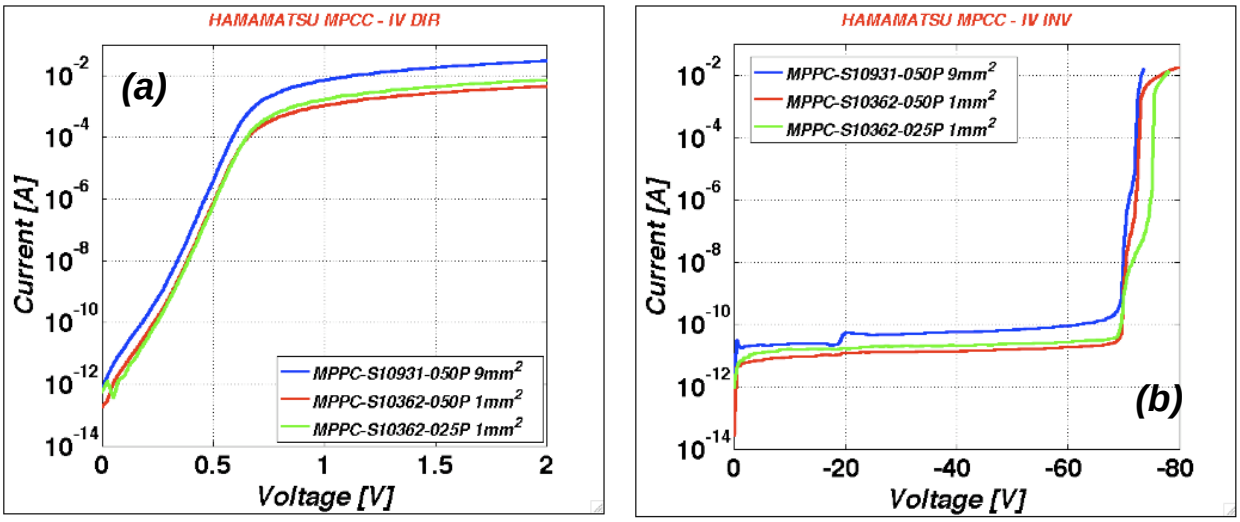

Figure 3.25: *Current voltage characteristics in (a) forward, (b) reverse polarization in dark at room temperature for three kinds of MPPC produced by Hamamatsu. They have different area and layout. The S10931-050P device has and active area of 9mm^2 and is formed by 3600 pixels having an area of 50 μm × 50 μm. The S10362-050P and S10362-025P have the same active area, 1mm^2, but different pixels number and dimensions: 400 pixel with an area of 50 μm × 50 μm and 1600 pixels with an area of 25 μm × 25 μm, respectively.*

similar to those measured for the ST devices having similar pixel active area: ≈ 5e-9 A below breakdown and ≈ 2e-6 A just above breakdown for SiPM with a total area of 6.5mm^2.

The analisys of the data, as already reported in Chapter 2, allowed the determination of the electrical parameters thus providing more insight on Hamamatsu devices.

The break down voltage clearly shows that the Hamamatsu pixels have a lower doping concentration than the counterpart produced by ST. In order to have a BV of about -69V the n-type region must have a dopant concentration of about 8×10^{15} atoms/cm3, higher than the 6×10^{16} atoms/cm3 of ST pixels. The higher doping of ST devices allowed they to have a lower operative voltage.

Figure 3.26 (a) shows the reverse voltage characteristics close to breakdown as a function of the device temperature in the temperature range -25°C – 65°C for the MPCC S10362-050P. the same figure reports, with black dots, the lowest current values producing the avalanche multiplication. The voltage value corresponding to the points are the BV values. By increasing the temperature, BV voltages increase in absolute value, as expected (Figure3_26

(b)). In fact a higher electrical field is needed to transfer enough energy to the carriers to produce the avalanche. The interaction with the crystalline reticule increases with temperature because atoms oscillations around their position increases in amplitude and so does the cross section for carrier impact, thus reducing the mean free path and the carrier average velocity. Breakdown voltage variation is linear for the three devices inspected and is has a value of -50mV/°C. Also the breakdown voltage change with temperature is lower for the ST devices (29mV/°C), suggesting an easier employ of these last devices for those application where an increase in the operation temperature may occur.

Figure 3.27 (a) reports the forward I-V characteristics as a function of temperature in the range from -25°C to 65°C for the same device shown in Figure 3.26 (a) (S10362-050P). the interpolation of the current values to voltages higher than 1.5V allowed us to determine the device resistance as a function of temperature. Being the number of pixels connected in parallel known (N_{PIXEL}) , it is possible to determine from the full device resistance (R_{MPPC}) the

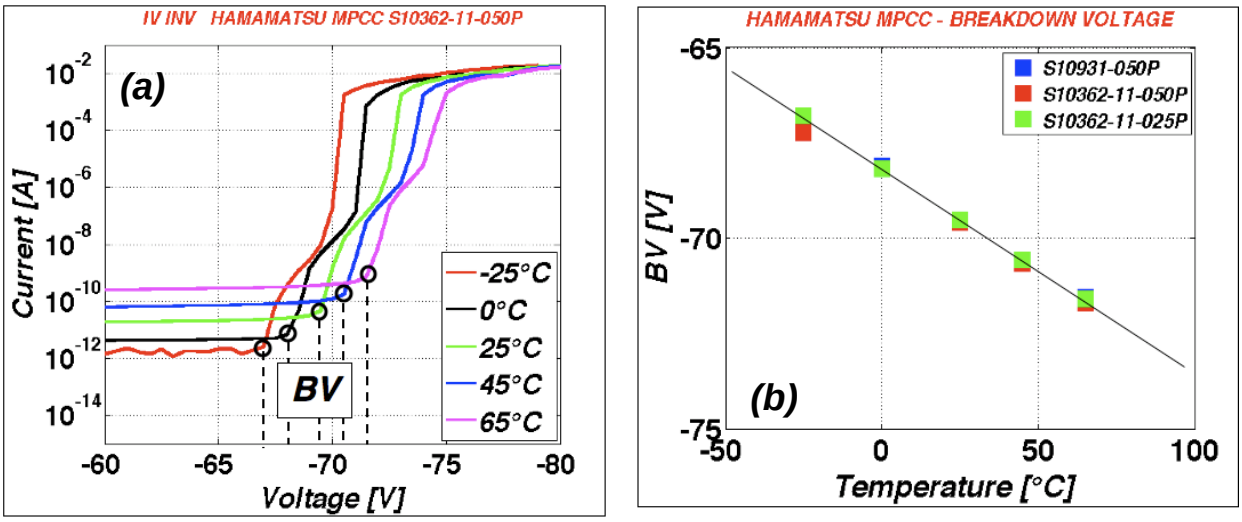

Figure 3.26: *(a) reverse current characteristics as a function of temperature for voltages close to breakdown. The black circles indicate the BV (b) Breakdown voltage as a function of the temperature for the three devices studied. BV at room temperature is -69V for all devices and it increases with temperature with a rate of 50mV/°C.*

single pixel quenching resistance ($R_{Q,cell}$). It is provided by Equation:

$$R_{Q,cell} = R_{MPPC} \cdot N_{PIXEL} \tag{3.5.1}$$

This simple equation allowed us to determine also the temperature dependence of the quenching resistance.

As an example, Figure 3.27 (a) shows the I-V characteristics in forward voltage operation of the S10362-050P MPCC as a function of the device temperature from -25°C (red line) up to 65°C (magenta line). From these data it is possible to determine (fitting the curves above 1 V) the device resistance and the single pixel quenching resistance, those values as a function of temperature are reported in Figure 3.27 (b) for the three Hamamatsu devices.

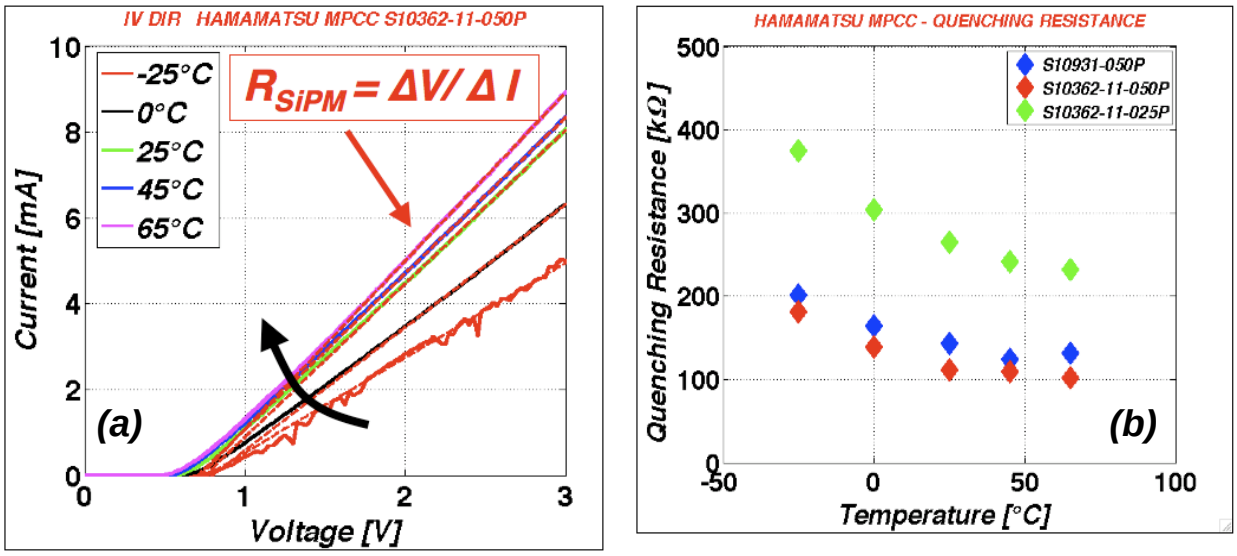

Figure 3.27*: (a) Forward voltage characteristics of the MPCC S10362-050P produced by Hamamatsu as a function of the temperature. The forward current values above 1V allowed to determine the resistance in series of the full device. Since the pixel number is known, (b) the single pixel quenching resistance as a function of temperature for all the devices can be extracted. The quenching resistance value is the same for the devices having the same area, while it is much higher for the device having smaller pixel area.*

It is interesting to observe that the devices having the same pixel active area, S10931-050P (blue points) and S10362-11-050P (red data) have similar quenching resistance values, while the device having pixels with a lower active area, the S10362-11-025P (green points) has a value that is almost double. At room temperature (25°C) the quenching resistance of the 50 μm × 50 μm pixel is roughly 150 kΩ, while the one of the 25 μm × 25 μm pixel is about 250 kΩ. Quenching resistance of ST SiPMs is about 225kΩ for pixels with an active area of 40 μm × 40 μm. the difference in the values is probably due to geometrical factors, but further measurements are in progress to understand if a difference in the resistance values can produce better device performances.

Finally, the quenching resistance value variation as a function of the temperature follows an exponential law, suggesting it is a polysilicon resistance.

Figure 3.28 (a) shows the forward current voltage characteristic in a semi logarithmic scale for the MPCC S10362-050P. As already mentioned in Chapter 2, the forward current is provided by two different phenomena: the generation current ($I_{0,scr}$) in the depletion region and the transport current ($I_{0,qnr}$) in the quasi neutral region. The first contribution is more evident at low voltages, while the second dominates at higher voltages. Since in the devices studied in Chapter 2 the first contribution is negligible, we will concentrate on the second one in order to make a comparison between the two producers. Forward current (I) in a diode is provided by:

$$I = I_{0,scr}\left(\frac{\exp(qV)}{nkt}\right) + I_{0,qnr}\left(\frac{\exp(qV)}{nkt}\right) \tag{3.5.2}$$

where q is the carrier charge, n is the ideality factor, k the Boltzmann constant and t the temperature. The curve slope in a semi-log vertical scale provides the ideality factor (see — 2.2.1 for a more detailed explanation) in each region, the fit intercept with the vertical axis provides $I_{0,scr}$ and $I_{o,qnr}$, as shown in Figure 3.28 (a).

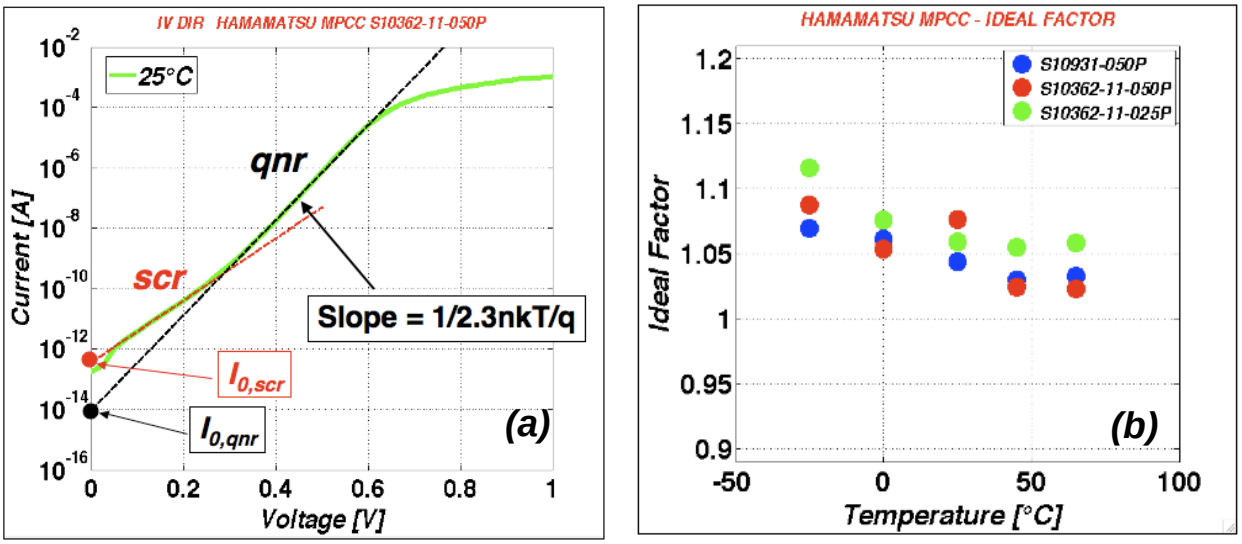

Figure 3.28: *(a) Forward current voltage characteristics at room temperature for Hamamatsu MPCC S10362-11-050P. forward current is provided by the sum of two contributions: carrier generation (scr, red line) and transport from the quasi neutral region (qnr, black line). The slope of the qnr provides the device ideality factor summarized in (b)as a function of temperature for the three Hamamatsu devices. n value at room temperature is 1.05.*

Figure 3.28 (b) reports the ideality factors, as determined by the slope of the qnr region, as a function of the device temperature for all the Hamamatsu SiPMs. At room temperature the n value is 1.05, closer to the ideality than the one obtained from ST devices (~1.18).

Finally, Figure 3.29 summarizes the transport currents ($I_{0,scr}$) as a function of the temperature for the three Hamamatsu devices. In the ideal junction $I_{0,scr}$ is provided by the formula:

$$I_{0,scr} \approx qn_i^2 A \frac{D_p}{N_D L_P} \tag{3.5.3}$$

where q is the electron charge, ni is the carrier intrinsic concentration, A the device area, Dp is the holes diffusion coefficient, N_D the majority carrier (electrons in this case) concentration and L_p is the diffusion length of minority carriers. The experimental data were fitted (solid

lines in figure) using the following parameters: N_D=9E15cm^{-3}, D_p =14 cm^{2}s^{-1}, and *Lp = 500 μm.* further measurements are needed in order to confirm these values.

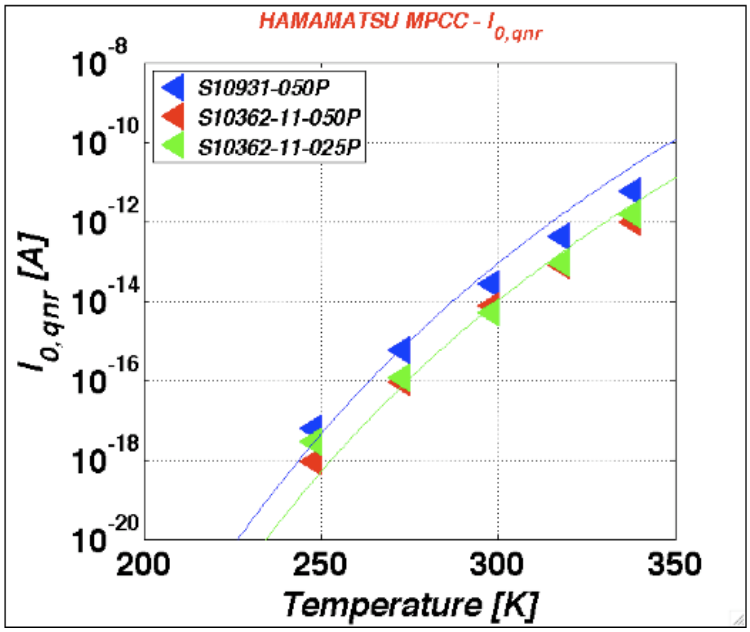

Figure 3.29: *Transport current as a function of the device temperature for the S10931-050P (blue points), S10362-11-050P (red points) and S10362-11-025P (green points). The solid lines are fits of the data obtained using Equation 3.5.3.*

§ 3.6 Conclusions

In this chapter the analysis performed on SiPM devices is reported. It should be reminded that a SiPM is an array of pixels connected in parallel. Each is given by a diode and a quenching resistance. The devices studied are arrays of 5x5, 10x10, 20x20 and 64x64 pixels produced by STMicroelectronics, each pixel has a size of 40 μm × 40 μm; and commercial devices having 400, 1600 and 3600 pixels produced by Hamamatsu photonics. The single pixel dimension are 50 μm × 50 μm, 25 μm × 25 μm and 50 μm × 50 μm, respectively. The data reported in this chapter can be summarized as follows:

1. issues not visible in single pixels become determinant in arrays. As an example, in section 3.5 it is shown that the crosstalk and the presence of random defects on the wafer affects the performances of arrays, becoming more important as the pixel number increases.
2. when the technology is optimized, devices with the same BV regardless of the number of pixel are produced.
3. the presence of trenches strongly reduces the optical crosstalk issue, regardless of the number of pixels. Moreover, trenches presence allows a more controlled process, as shown by the reduction on the spread in the parasitic resistance (section —3.2.1)
4. the array behaviour cannot be modelled assuming that the physics is the same proposed for the single cell, since two main phenomena occur in arrays: the crosstalk and the defects statistical presence. The first effect is strongly reduced but not avoided with trenches, while the second is a wafer intrinsic problem. In the devices there is a very low defect concentration , estimated of $1x10^9$ defects/cm^3 for the single cell. It means that these is 1.6 defect for each pixel. It is obvious that small statistical fluctuation in this number can produce large variations in the single pixel behaviour thus producing a spread in the array characteristic values. More studies are needed to correctly model the array behaviour.

Chapter 4

Radiation hardness

Radiation hardness: preliminary study

Silicon Photomultipliers (SiPM) are considered a promising candidate to substitute the traditionally used photomultipliers tubes in particle physics experiments and as for the time of flight of space experiments [86] and astrophysics experiments [87] thanks to some intriguing features: low weight, low consumption, constant performances for a long time and, for spectrometry applications, insensitivity to magnetic fields. Of course, in order to be a suitable candidate for space application, their radiation tolerance must be tested. Up to now a systematic study is missing, even if some interesting experiments performed irradiating with electrons [88], neutrons [89] and protons [87] have been reported in literature. This lack of experimental data can be partially explained considering that SiPM are formed by an array of Si avalanche photodetectors (SPAD) operating in Geiger mode and connected in parallel through opportunely designed resistances. Hence, it is expected that SiPM radiation tolerance is similar to the Si diodes one.

Aim of this chapter is to investigate both the single cells and SiPM arrays, produced by STMicroelectronics, behaviour as a function of the irradiation dose for both light ions, heavy ions and X-rays irradiation.

§ 4.1 Irradiations

Irradiations were performed using different ions and facilities. In this section a brief overview of the different species and facilities is reported.

X rays irradiations were performed at the Dipartimento di Fisica e Tecnologie Relative (DIFTER) at the University of Palermo. 10 keV X-rays were generated by the Tungsten L-lines radiation, produced by *Seyfert* Air-insulated diffraction X-ray tube type *SN60*. The samples were irradiated in air to fluences of 0.5, 5 and 20 krad(Si) using a flux of 3.9 rad(Si)/s. During irradiations all the samples were unbiased. A list of the samples is provided in Table 4.1.

B implantations were performed in vacuum with a 1.7MW *High Voltage* Tandetron using 10 MeV 11B with a total fluence ranging from 3.0×10^{7} cm^{-2} to 5×10^{10} cm^{-2}. Fluence rate was $\sim3\times10^{6}$ $B/cm^{2}\times s$. The ion projected range (Rp) is 10-12 μm. The full device list is summarized in Table 4.1.

Finally, heavy ion irradiation was performed using the Laboratorio Nazionale del Sud (LNS) of the istituto Nazionale di Fisica Nucleare (INFN) facilities: a Tandetron for Br implantation and a Linear Sincrotron (LS) for gold ion irradiation. The samples were placed in the test chamber according to the schematic shown in Figure 4.1 and the full list of samples is reported in Table 4.1.

The heavy ion beam is not uniform in the space, and it has an intensity shaped as a Gaussian profile. It has a circular section of about 8 mm^{2}. For this reason the test pattern was centred with respect to the beam centre. Since the test pattern is smaller than the beam section, also the SiPM arrays having 64×64 pixels closer to the test pattern experienced the direct beam irradiation.

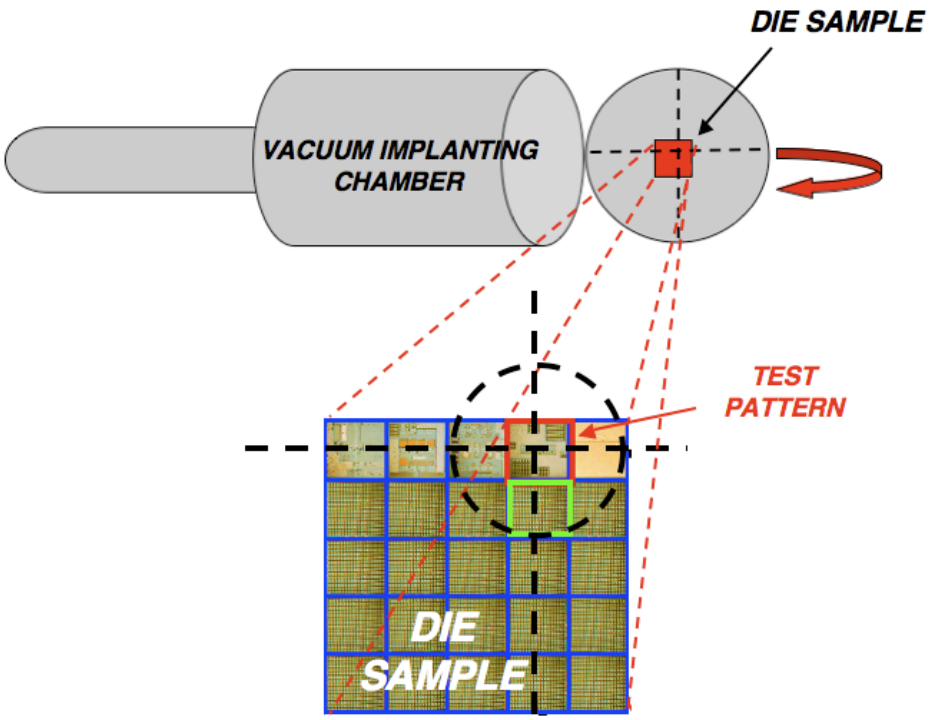

Figure 4.1: *Schematic of the vacuum implanting chamber and of the expected beam centre with respect to the die*

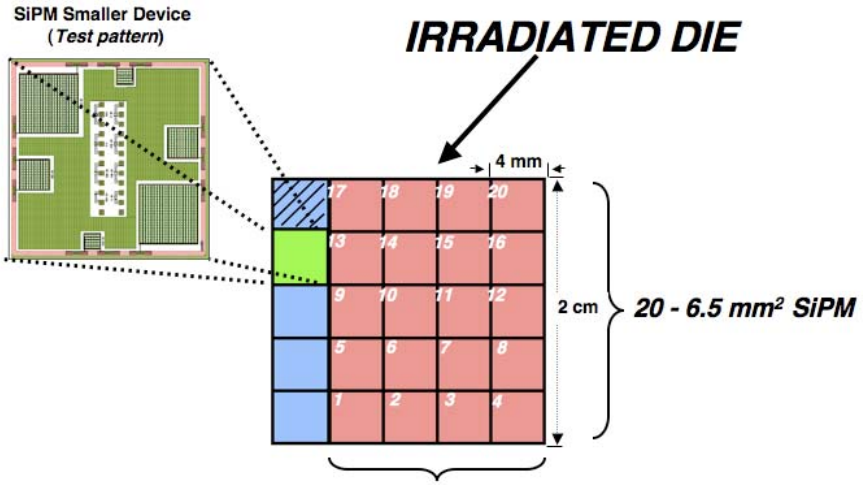

Figure 4.2: *Schematic of the test pattern position with respect to the die*

Species	Dose (ions/cm²)	Dose (rad)	Energy (eV)	Rp (μm)
X-rays	/	0.5	$10x10^3$	passing
X-rays	/	5	$10x10^3$	passing
X-rays	/	20	$10x10^3$	passing
B	$3.1x10^7$	310	$10x10^6$	10-11
B	$5x10^8$	$5x10^3$	$10x10^6$	10-11
B	$5x10^9$	$50x10^3$	$10x10^6$	10-11
B	$5x10^{10}$	$500x10^3$	$10x10^6$	10-11
B	$5x10^{11}$	$5x10^6$	$10x10^6$	10-11
Br	$5x10^8$	$255x10^3$	$196x10^6$	26
Br	$5x10^9$	$2.55x10^6$	$196x10^6$	26
Br	$1.25x10^{10}$	$6.4x10^6$	$196x10^6$	26
Au	$1x10^9$	$1.2x10^6$	$5.1x10^6$	291
Au	$1x10^{10}$	$6x10^6$	$5.1x10^6$	291
Au	$1x10^{11}$	$120x10^6$	$5.1x10^6$	291

Table 4.1: *irradiation an implantation conditions for: (a) X-rays, (b) B, (c) Br and (d) Au*

§ 4.2 X-rays irradiation

— 4.2.1 Electrical characterization

SiPM arrays electrical characterization was performed before and after X-rays irradiation. The IV obtained before (solid line) and after irradiation at the different irradiation doses, are compared in Figure 4.3 for a 10x10 array. The sample before irradiation shows the typical current voltage (I-V) reverse voltage characteristic acquired at room temperature (see chapter 3). A detailed description of the forward and reverse voltage characteristics is provided in paragraph § 3.2.

Briefly, the I-V can be divided into three separate regions: the region below breakdown that extends from zero up to BV, occurring at 27.9±0.1 V. In that region the dark current, quite low in the sample before irradiation (~10pA), linearly increases as a function of the irradiation fluence, this behaviour is summarized for more clarity in Figure 4.3 (a) (downward

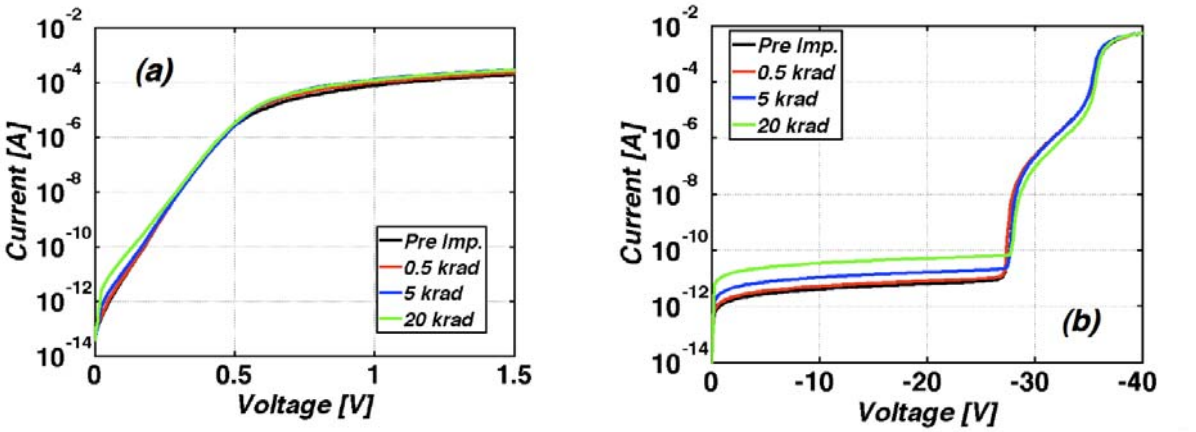

Figure 4.3: *Current voltage characteristic in (a) forward and (b) reverse voltage of SiPM 10×10 array before irradiation (black line) and after 0.5 Krad(Si) (red line), 5 Krad(Si) (blue line) and 20 Krad(Si) (green line). All curves were acquired at room temperature.*

pointing triangles). The region between BV and -36 V is the range of interest for the Geiger mode operation. In this region only small differences in the current value, already visible in the samples before irradiation (see after) are observed, to indicate that the irradiation damage does not affect significantly the device operation. Finally, in the region above -37 V the current is likely dominated by afterpulsing, since the secondary carriers generated during the primary avalanche cascade are able to trigger new avalanche phenomena due to the high electric field experienced by the carriers in the depletion region. Once again, no visible differences were observed before and after irradiation with X-rays.

The same kind of measurements were performed on single cells and arrays from 5x5 (circles) up to 64x64 (diamonds) cells. The leakage currents below breakdown (-20V) are summarized in Figure 4.4 (*a*), while the dark current at the operation voltage (-32V, ~15% above BV) are compared in Figure 4.4 (b). In both graphs the current values as a function of the irradiation dose are reported for all the measured devices. The leakage current (below BV) linearly increases as a function of the irradiation dose, as already observed after proton irradiation [88]. More interesting is the situation above breakdown. The dark current is not

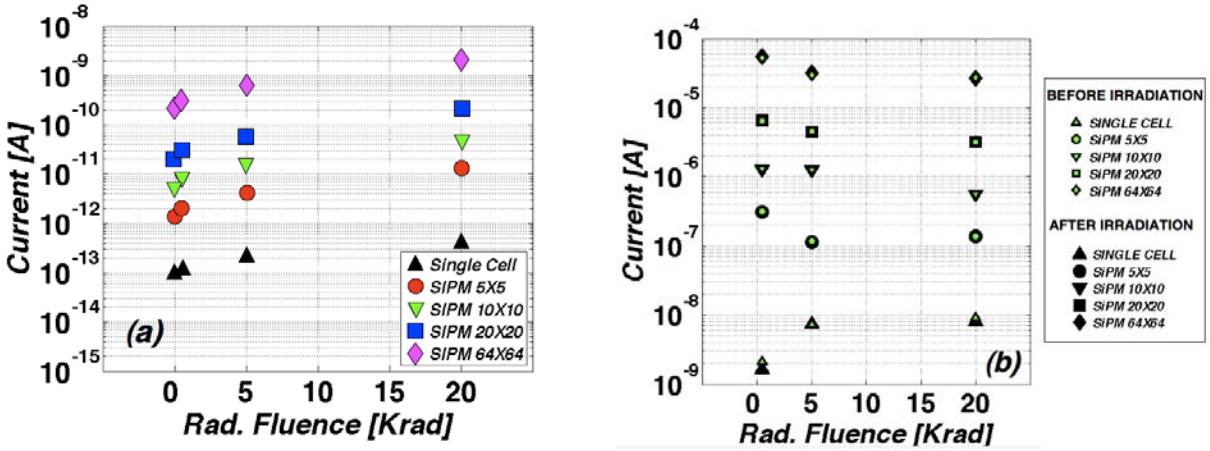

Figure 4.4: *(a) leakage current below breakdown (at -20V) and (b) dark current at operation voltage (-32 V, ~15% above breakdown) as a function of the irradiation dose for a single cell (upward pointing triangles), 5x5 (circles), 10x10 (downward-pointing triangles), 20x20 (squares) and 64 x64 (diamonds) SiPM arrays. The leakage currents before irradiation are also reported (open symbols).*

affected by irradiation, as clearly observed in figure. In fact, the only differences in the dark current values, also visible in Figure 4.3, are due to a spread already detected before irradiation on the different samples as clearly demonstrated by the almost perfect overlap of the before (open symbols) and after irradiation (filled symbols) data summarized in Figure 4.4 (b). The results obtained for the 10x10 array holds for all the measured devices, from single cells up to 64x64 arrays.

The data so far reported seem to indicate that the damage formed during X-rays irradiation is a quite low concentration and does not affect the final device performances. This result suggests that even after irradiation the devices are able to detect low photon fluxes. The confirmation of this hypothesis was provided by the optical characterization described in the next section.

— 4.4.2 Optical characterization

The devices were optically characterized using a laser operating at 659 nm and filters to reduce the light intensity. The results obtained using 10x10 arrays are reported in Figure 4.5, where the IV characteristics in dark (black line) are compared with the characteristics obtained when a photon flux of 220nW/cm2 (green line), 22nW/cm2 (blue line) and 2.2nW/cm2 (redline) shines the device before (solid lines) and after irradiation (dashed lines). The two extreme irradiation conditions are reported: 0.5 Krad(Si) in Figure 4.5 (a) and 20Krad(Si) in Figure 4.5 (b). The inspection of the results at low dose (Figure 4.5 (a)) clearly shows that the IV curves perfectly overlap for all the used fluxes, indicating that the device ability to detect low photon fluxes is not compromised by the irradiation process. Different is the situation after 20Krad(Si) irradiation and observed in Figure 4.5 (b): the leakage current below BV increases in dark, as already observed.

When light is shined on the device, the current slightly decreases with respect to the unirradiated case. This behaviour could be associated to a deterioration of the gain, in particularly a decrease, as already observed in ref. [88] for a different irradiation source.

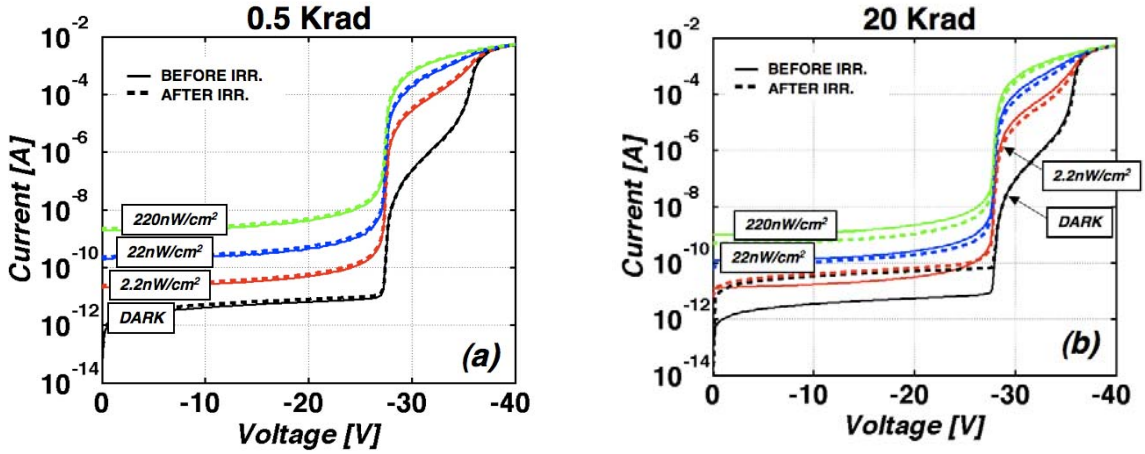

Figure 4.5: *IV characteristics in reverse voltage as a function of the light intensity before (solid lines) and after irradiation (dashed lines) in dark (black lines), during 2.2 nW/cm2 (red lines), 22 nW/cm2 (blue lines) and 220 nW/cm2 (green lines) illumination for a sample irradiated at (a) 0.5 krad and (b) 20 krad.*

More interesting results were obtained monitoring the devices gain as a function of the overvoltage according to the procedure already described in Chapter 2. [90]. As already mentioned, the devices presented a spread in the gain values before irradiation, this results was already obtained by the inspection of the dark currents reported in Figure 4.3 (b). The comparison of the gain before (open symbols) and after (filled symbols) irradiation with 0.5 krad (squares) and 20 krad (circles) reported in Figure 4.6 clearly shows a progressive reduction of the gain when the overvoltage increases at the highest dose. The same effect was measured after proton irradiation [87]. It is interesting to observe that our devices seem to have a higher radiation tolerance than those measured in Ref. [87]. In fact, devices in Ref. [87] already deviate from the unirradiated devices gain after proton irradiation of 8Gy (corresponding to 0.8 krad) while we observed a significant deviation only for X-rays doses of 20 krad. More measurements are in progress to quantify the radiation tolerance threshold.

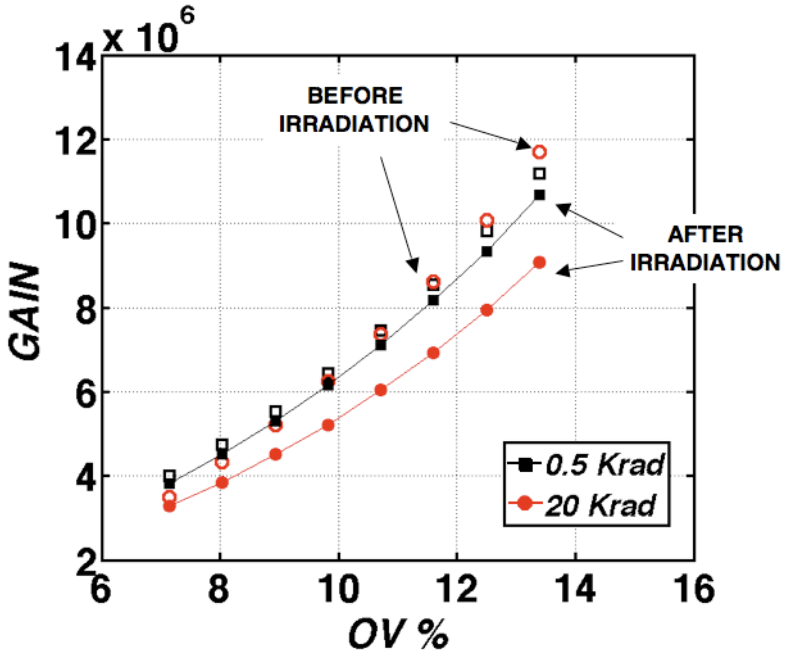

Figure 4.6: *Gain of 10×10 pixels SiPM before irradiation (open symbols) and after irradiation (filled symbols). The gain was measured from inverse current under illumination as described in Chapter 2[90]*

§ 4.3 Ion implantation

Dramatically different is the case of ion implantation. Even the lowest dose used causes a strong modification of the full I-V curve, as clearly shown in Figure 4.7, where the IV in forward (Figure 4.7 (a)) and reverse voltage (Figure 4.7 (b)) curves before (black dots) and after irradiation at increasing from 3.1×10^{7} B/cm^2 (red squares) up to 5×10^{10}B/cm^2 (magenta dots) doses are compared. The presence of defects strongly modifies both characteristics: in forward current the devices switch on at lower voltages increasing the dose, suggesting the presence of defects in the depletion region in concentration enough high to cause a current flow also at low fields. A progressive increase in the leakage current below threshold is observed as a function of the implantation dose. The difference between the curves increases

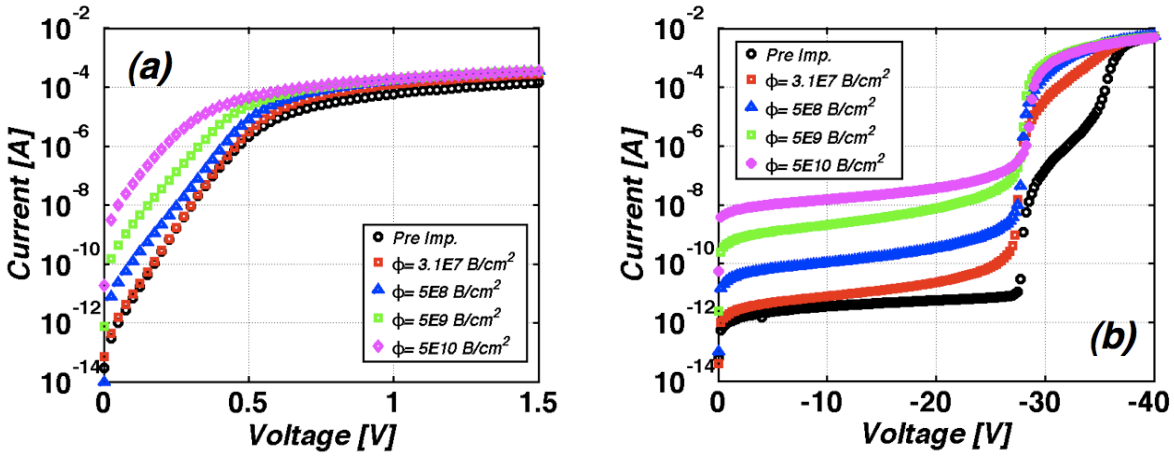

Figure 4.7: *Current characteristics in (a) forward and (b) reverse voltage at room temperature for a SiPM 10x10 array before irradiation (black dots) and after 3.1×10^{7} B/cm^2 (red dots), 5×10^{8} B/cm^2 (blue triangles), 5×10^{9} B/cm^2 (green squares) and 5×10^{10} B/cm^2 (magenta dots) ion irradiation.*

with voltage to approach a three order of magnitude difference between the unimplanted and 5×10^{10} B/cm2 implanted samples the at the operation voltage (-32V).

A more careful inspection of the curves can be performed by comparing the reverse voltage characteristics for the unirradiated sample (black line) and the sample irradiated to the lowest dose ($5\text{x}10^{7}$ B/cm^2, dashed red line), as shown in Figure 4.8 (a). A strong difference with respect to the x-rays irradiation case is evident from the figure. There are two main differences between the kinds of irradiation: first of all ion collision cascade is denser than x-rays, moreover, the projected range of 10 MeV ion implantation is about 12 μm from the surface, hence the ions can stop within the sensitive region of the device. In ion implantation most of the damage (Frenkel pair generation) occurs in a narrow region close to the ion end of range, hence a significant quantity of defects sits in this region [91]. The leakage current slightly increases with respect to the unimplanted sample until the depletion region approaches the implanted ion end of range. Once the damage is in the depletion region, divacancies, boron-carbon, carbon-oxygen and oxygen-vacancy complexes act as quite efficient generation centres, and cause a strong increase of the dark current. To confirm this

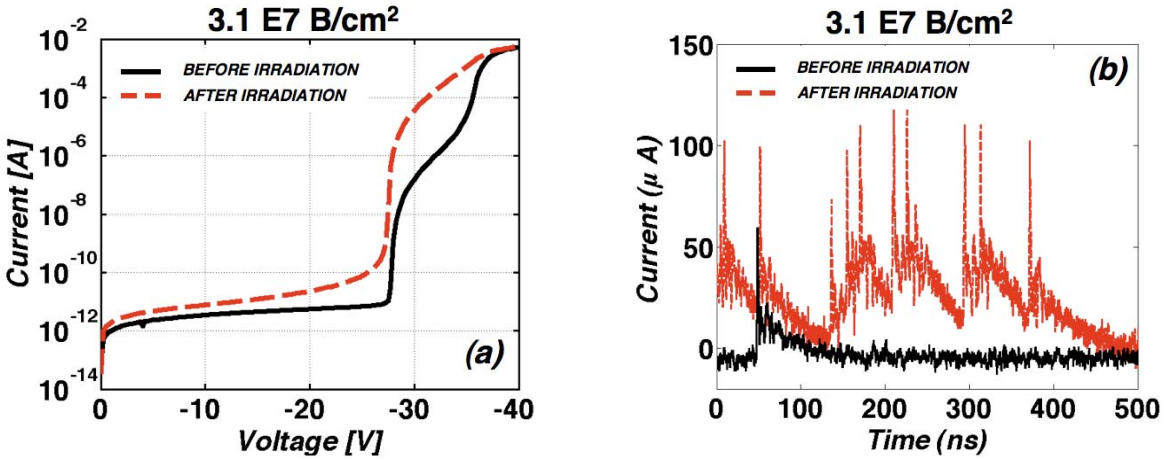

Figure 4.8: *(a) Dark current in inverse voltage at room temperature for a SiPM 10×10 array before irradiation (solid line) and after 3.1×10⁷ B/cm2 ion irradiation (dashed line). (b) Dark pulse observed with the oscilloscope for the same device using an OV of ~15% at room temperature before irradiation (solid line) and after irradiation (dashed line). After irradiation the dark current of the sensor is a continuous train of pulses due to the creation of various defects.*

hypothesis, the strong presence of afterpulsing was observed after ion implantation, as clearly visible from the inspection of Figure 4.8 (b), where the dark pulse shape, as acquired from the oscilloscope before and after implantation are plotted. Before implantation a single pulse is detected, while after implantation the primary pulse is immediately followed by a series of extra pulses. They are due to the carrier capture and retarded re-emission by the defects. The re-emitted charges trigger avalanche breakdowns immediately following the primary event [91].

The device deterioration is confirmed by the optical characterization. It is clear that the device sensitivity in the operation region is lost already after 3.1×10^{7} B/cm^2, as shown in Figure 4.9 (a), while the device is completely blind after 5×10^{10} B/cm^2 (see Figure 4.9 (b)).

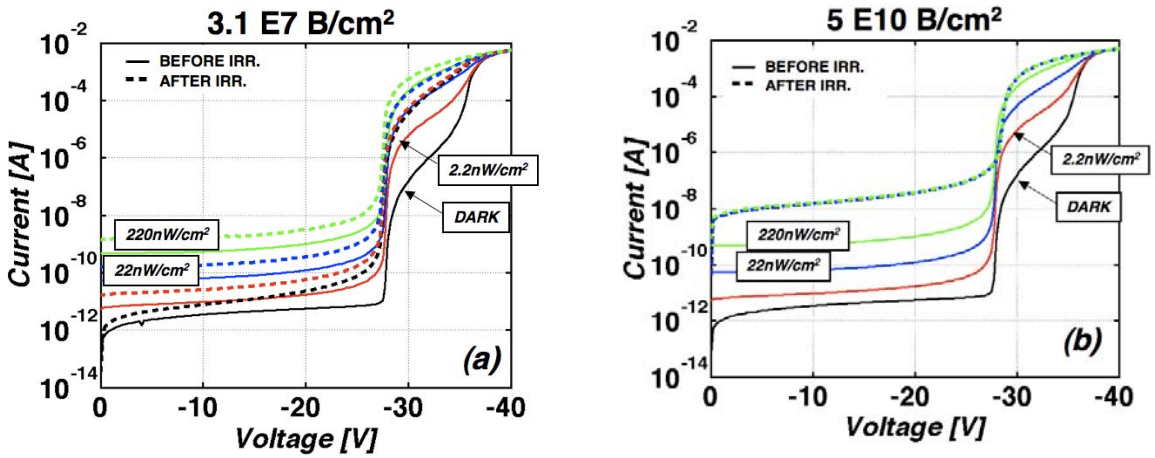

Figure 4.9: *Characteristics in reverse voltage as a function of the light intensity before (solid lines) and after irradiation (dashed lines) in dark (black lines), during 2.2 nW/cm^2 (red lines), during 22 nW/cm^2 (blue lines) and during 220 nW/cm^2 (green lines) illumination for a sample irradiated with (a) 3.1×10^7 B/cm^2 and (b) 5×10^{10} B/cm^2.*

§ 4.4 Heavy ion irradiations

The same study just described was carried out for samples that underwent heavy ion irradiation using both Br and Au.

— 4.4.1 Br irradiations

In Figure 4.10, the reverse voltage characteristics of a 20×20 array before (black circles) and after irradiation with 5×10^8 Br/cm^2 (red squares), 1×10^9 Br/cm^2 (blue triangles) and 1.25×10^{10} Br/cm^2 (green circles) are compared.

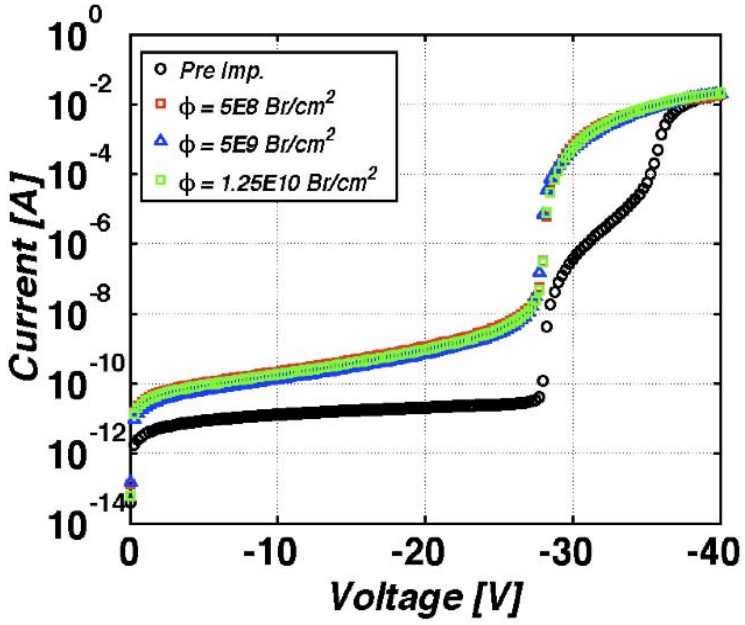

Figure 4.10: *Characteristics in reverse voltage as a function of the irradiation dose for an unirradiated device (black circles) and for devices irradiated with 5×10^{8} Br/cm^2 (red squares), 5×10^{9} Br/cm^2 (blue triangles) and 1.25×10^{10} Br/cm^2 (green squares).*

All the samples selected for the experiment, before ion irradiation, have identical electrical properties, i.e., Leakage Current, Dark Current, Breakdown Voltage and Ideality Factor with respect to the number of pixel. Leakage currents at voltages below BV increase but do not change as a function of the irradiation dose; above BV the dark currents are the same, much higher than before irradiation.

The same measurements were carried out on all the arrays and the results are summarized in Figure 4.11, where the current as a function of the Br irradiation dose are reported below breakdown (at -20V, Figure 4.11 (a)) and above breakdown (at -32V, Figure 4.11(b)).

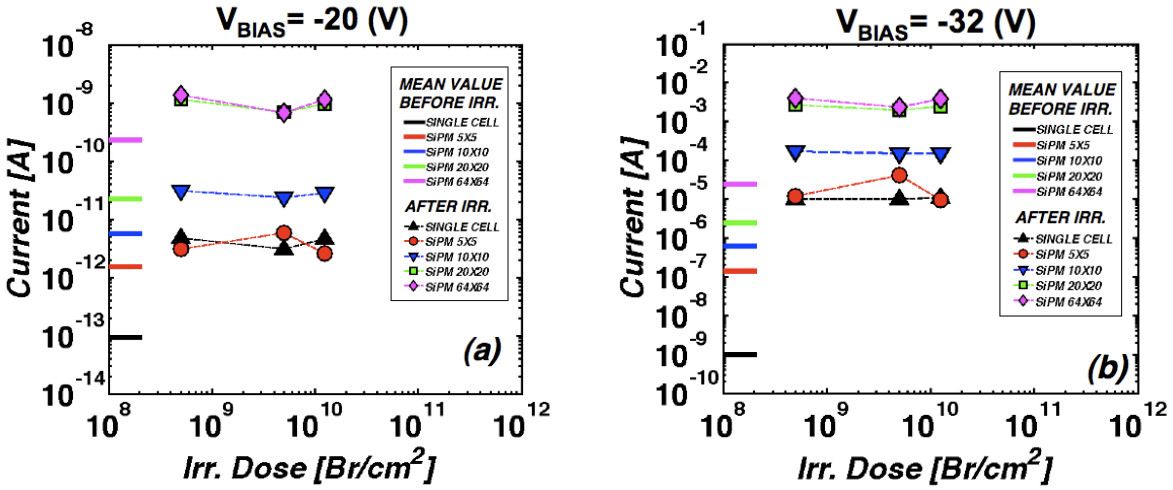

Figure 4.11: *Reverse Current as a function of the Br irradiation dose for a voltage of (a) -20 V and (b) -32V for single cells (black triangles) and 5×5 (red circles), 10×10 (blue triangles), 20×20 (green squares) and 64×64 (magenta diamonds) arrays. The solid lines refer to the unirradiated samples.*

As already observed from the row data the current does not change as a function of the irradiation dose, suggesting that the main damage features are introduced directly at the lowest irradiation dose. The device deterioration, as already observed for light ion implantation, is confirmed by the optical characterization. It is clear that the device sensitivity in the operation region is lost already after the lowest Br irradiation dose, as observed from the comparison of figures Figure 4.12 (a) and Figure 4.12 (b) where the IV reverse curves before and after irradiation, respectively, are shown as a function of the light optical power for a 20×20 array. A minimum sensitivity to the light flux is still present after 5×10^{8} Br/cm^{2} irradiation, but the device is blind in the operative region (-32 V).

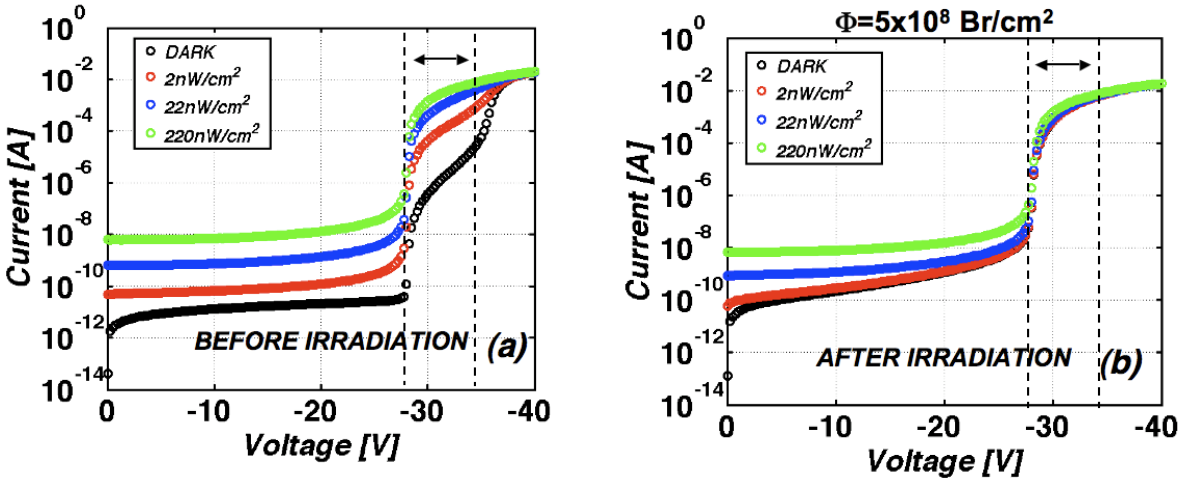

Figure 4.12: *Characteristics in reverse voltage as a function of the light intensity (a) before and (b) after irradiation in dark (black dots), during 2.2 nW/cm^2 (red dots), 22 nW/cm^2 (blue dots) and 220 nW/cm^2 (green dots) illumination for a sample irradiated with 5×10^8 Br/cm^2.*

A more interesting analysis can be performed on these samples: we monitored the dark current characteristics of all the SiPM on the die before and after (red lines in figure 4.xxa) 5x108 Br/cm2 irradiation and the comparison is shown in Figure 4.13 (a). The data clearly exhibit a spread in the current after irradiation. This spread was used to obtain information on the beam characteristics. In fact, all the device have exactly the same characteristics before irradiation (black lines), hence the current difference (I_{after} – I_{before}) was monitored as a function of the device position in the sample.

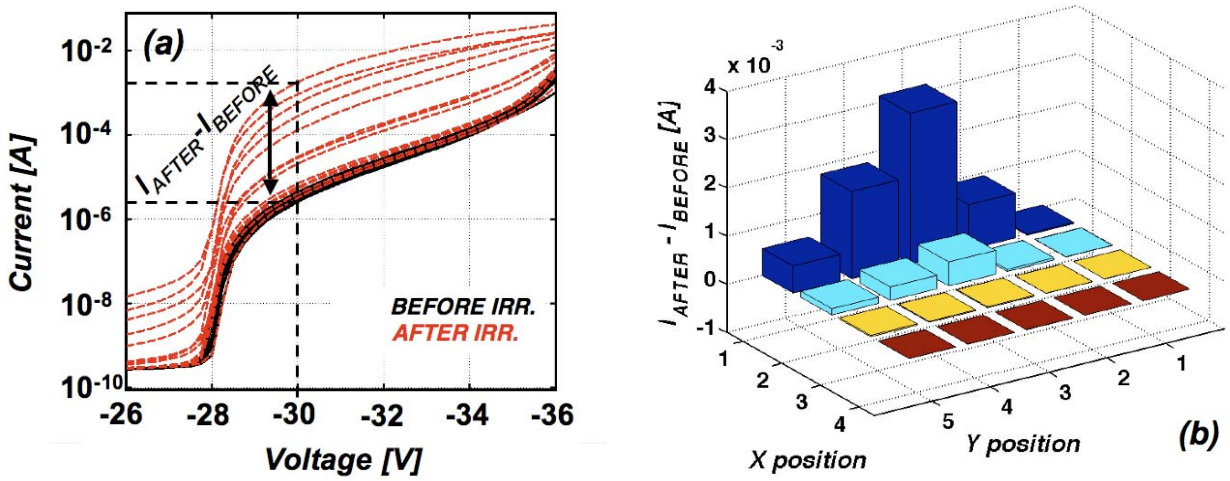

Figure 4.13: *(a) Characteristics in reverse voltage as a function of the device position for 64×64 arrays before (black lines) and after irradiation with 5×10^9 Br/cm^2 (dashed red lines); (b) histogram of the current differences as a function of the spatial position.*

The data indicate that the real beam is not aligned with the test pattern as expected. This could be the reason of the insensitivity of electrical parameters of the devices to the irradiation dose. The real alignment is shown in the schematic of Figure 4.14.

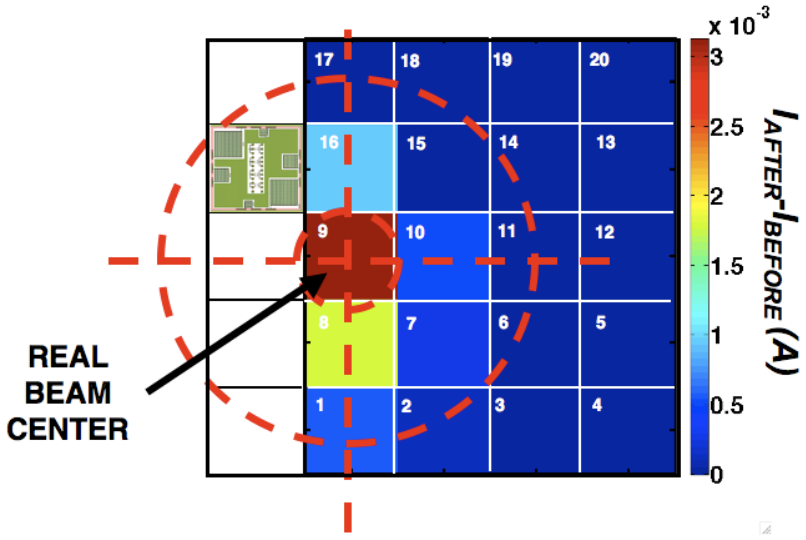

Figure 4.14: *Schematic of the device with respect to the REAL beam centre*

— 4.4.2 Au irradiations

A similar analysis was preformed on the Au irradiated samples. The three samples where placed at the end of the vacuum implanting chamber, according to the schematic shown in Figure 4.1, aligning the TEST PATTERN with the geometrical centre of the chamber. Two dies were disposed with the TEST PATTERN on the top and one with the TEST PATTERN on the bottom. Also in this case all the samples selected for the experiment, before ion irradiation, have identical electrical properties, i.e., Leakage Current, Dark Current, Breakdown Voltage and Ideality Factor with respect to the number of pixel. The devices I-V curves after Au irradiation are summarized in Figure 4.15 for a 20×20 array. Already after 1×10^{9} Au/cm^2 (red squares) a strong increase in the leakage current value with respect to the unirradiated samples (black circles). The leakage current increases with the irradiation dose and after a 1×10^{11} Au/cm^2 there is still an increase in the leakage current with respect to the lower dose (1×10^{10} Au/cm^2), thus suggesting that the damage in the surface region increases with the irradiation dose. Much worse is the situation in the operative region, where the

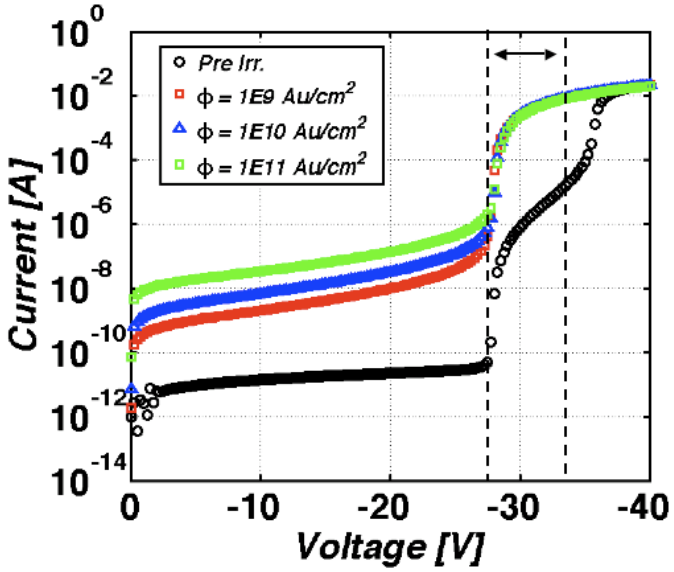

Figure 4.15: *Characteristics in reverse voltage as a function of the irradiation dose for an unirradiated device (black circles) and for devices irradiated with 1×10^{9} Au/cm^2 (red squares), 1×10^{10} Au/cm^2 (blue triangles) and 1×10^{11} Au/cm^2 (green squares).*

devices exhibit a strong increase in the dark current already after the lowest irradiation dose and all the data collapse on the same curve regardless of the irradiation fluence.

These conclusions are summarized in Figure 4.16 (a) and Figure 4.16 (b) where the leakage current at -20V and the dark current at -32V, respectively, are shown. The leakage current below BV could be linearly dependent on the irradiation dose. Indeed the statistics is too poor to perform a prediction about the real trend. Dashed line are only an eye guide, obtained fitting the data of the standard single cell and multiplying that fit for the pixel number for all the arrays dimensions. Marked data correspond to anomalous irradiation effects on the device. It should be mentioned that the fits do not correspond to the real data point for the largest arrays. The explanation of this "anomalous" behaviour is provided at the end of this section.

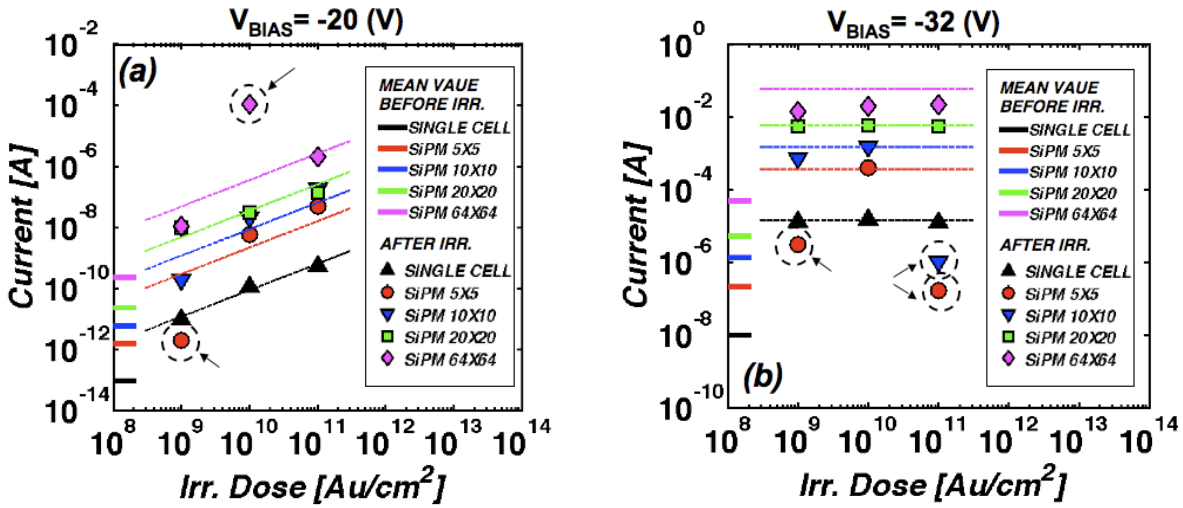

Figure 4.16: *Reverse Current as a function of the Au irradiation dose for a voltage of (a) -20 V and (b) -32V for single cells (black triangles) and 5×5 (red circles), 10×10 (blue triangles), 20×20 (green squares) and 64×64 (magenta diamonds) arrays. The solid lines refer to the unirradiated samples.*

The dark current above BV is constant after irradiation except for some deviations due to anomalous irradiation effects on the device. As previously reported, dashed line are only an

eye guide, obtained fitting the data of the standard cell and multiplying that fit for the pixel number for all the arrays studied. The currents after irradiation for SiPM 64×64 pixels are not those expected.

Also for these samples the optical characterization after irradiation does not provide any information: the devices are completely blind to the light, as shown in Figure 4.17 (b), where the reverse voltage characteristics during light irradiation to different optical powers are reported before (Figure 4.17 (a)) and after irradiation (Figure 4.17 (b)).

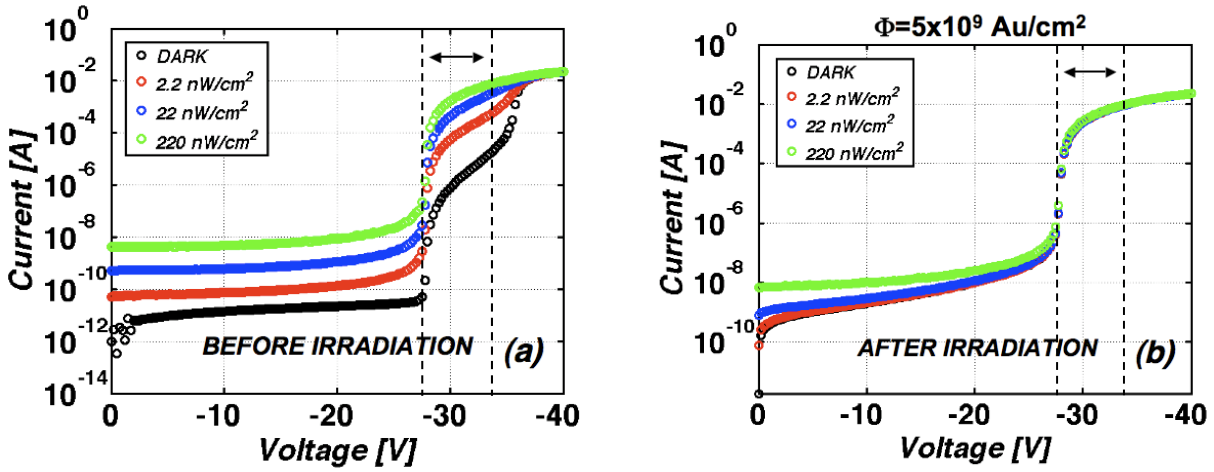

Figure 4.17: *Characteristics in reverse voltage as a function of the light intensity (a) before and (b) after irradiation in dark (black dots), during 2.2 nW/cm^2 (red dots), 22 nW/cm^2 (blue dots) and 220 nW/cm^2 (green dots) illumination for a sample irradiated with 5×10^9 Au/cm^2.*

Also in this case a detailed study to define the beam characteristics was carried out. To this purpose, the three samples in the irradiation chamber were placed as shown in Figure 4.18. The three dies where placed at the end of the vacuum irradiation chamber aligning the test pattern with the geometrical centre of the chamber. Two dies (DIE 1 and 3) were placed with the test pattern on the top part of the site, while the other die (DIE 2) with the test pattern on the bottom side of the site.

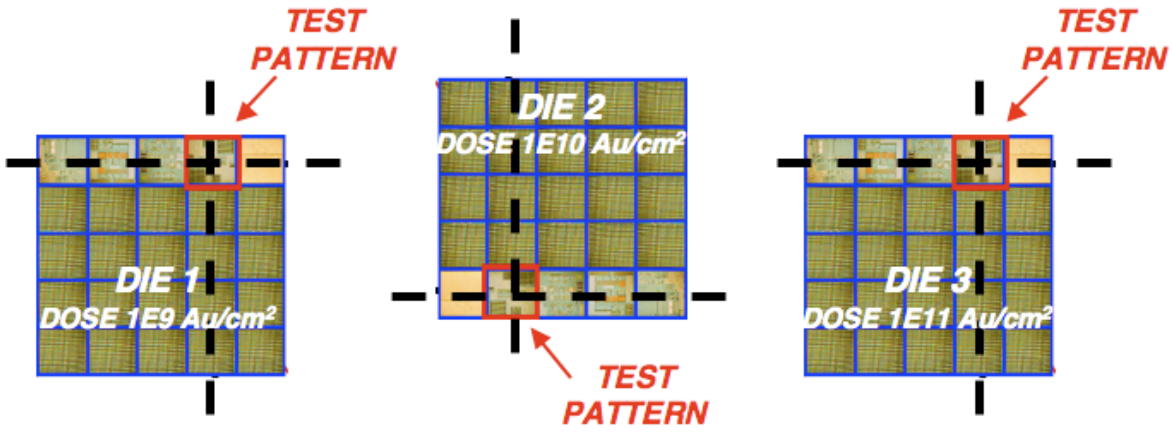

Figure 4.18: *Schematic of the die position with respect to the expected beam centre. Please note that DIE 2 is placed in the opposite way with respect to the other dies.*

The IV curves of the full SiPM (64 ×64 arrays, 20 sites) were collected before and after ion irradiation, as reported in Figure 4.19 (a). The difference between the dark current of the sensors after irradiation and before was used to reconstruct the ion beam profile, assuming

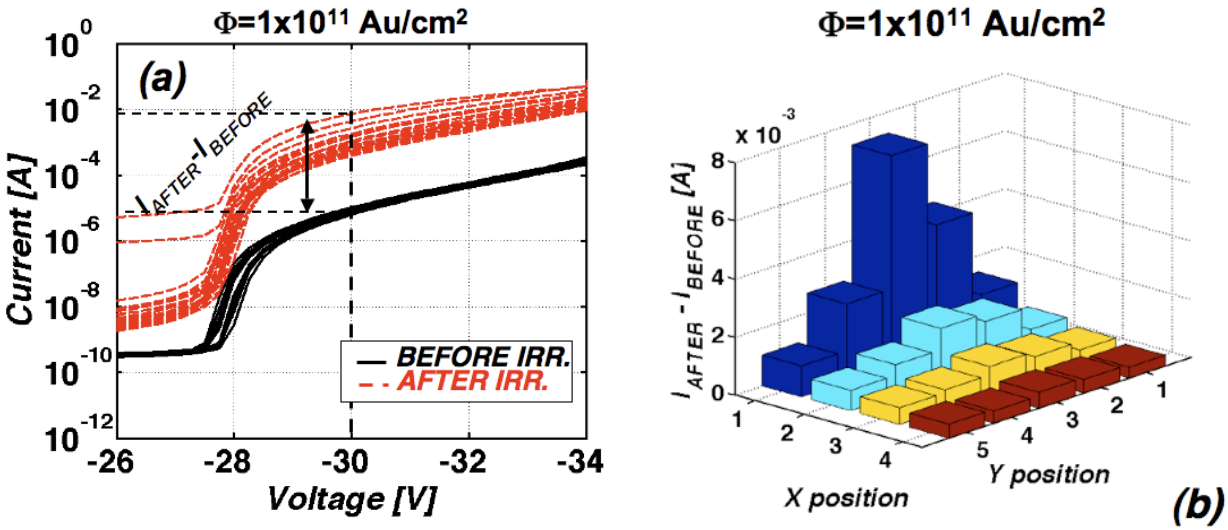

Figure 4.19: *(a) Characteristics in reverse voltage as a function of the device position for 64×64 arrays before (black lines) and after irradiation with 1×10^{11} Au/cm^2 (dashed red lines); (b) histogram of the current differences as a function of the spatial position.*

that the intensity of the beam is proportional to such difference. A histogram of the beam profile is shown in Figure 4.19 (b) as an example.

From the discrete distributions, similar to the one shown in Figure 4.19 (b), we interpolated the data with a cubic law and reconstructed a continuous surface, representing the current difference, that is proportional to the ion beam intensity. Joining the data of DIE 1 and 2, placed in the opposite way in the chamber, and opportunely normalizing, since the irradiation doses were not the same, it was possible to reconstruct the ions beam intensity profile.

The final beam reconstruction is shown in Figure 4.20. The beam so reconstructed has a diameter of 8 mm diameter, as expected, since it crossed a hole having 8 mm of diameter. It should be noted that this is only a demonstration of one possible application, and not the best, for this kind of sensor.

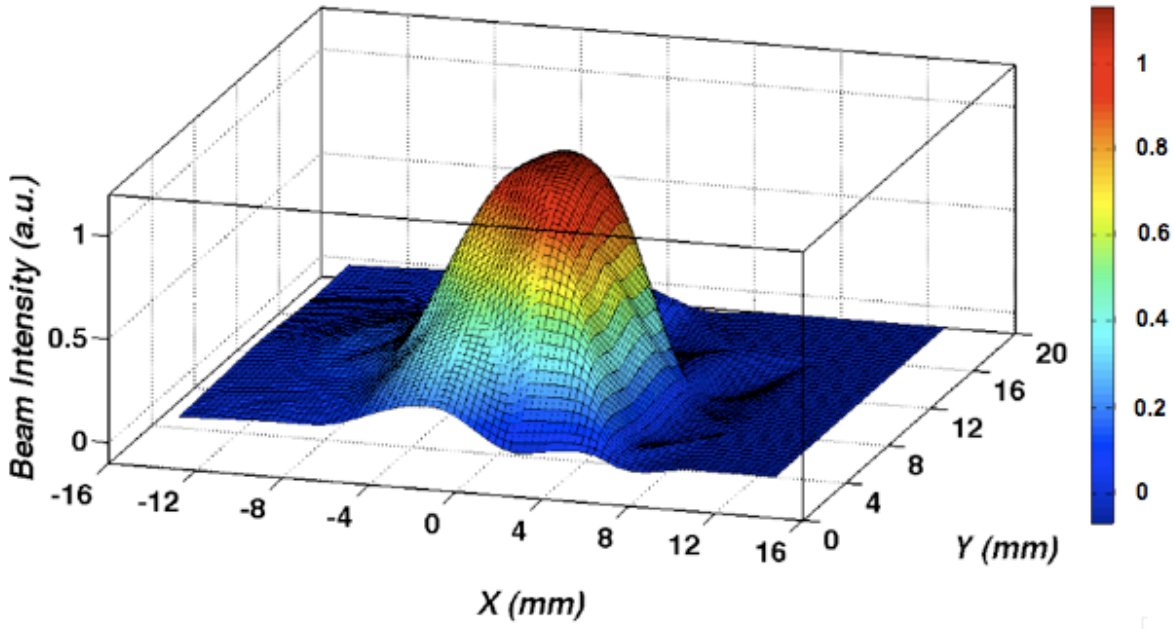

Figure 4.20: *Reconstruction of the beam profile*

The beam size, and the position of the die with respect to it, is clearly evidenced by the Em.Mi. image of the Die 2 after $1x10^{10}$ Au/cm^2. all the pixels directly invested by the beam

appear in the image as hot points. In the case of 64×64 pixels SiPM alny a fraction, about 1270 pixels are directly interested by the beam.

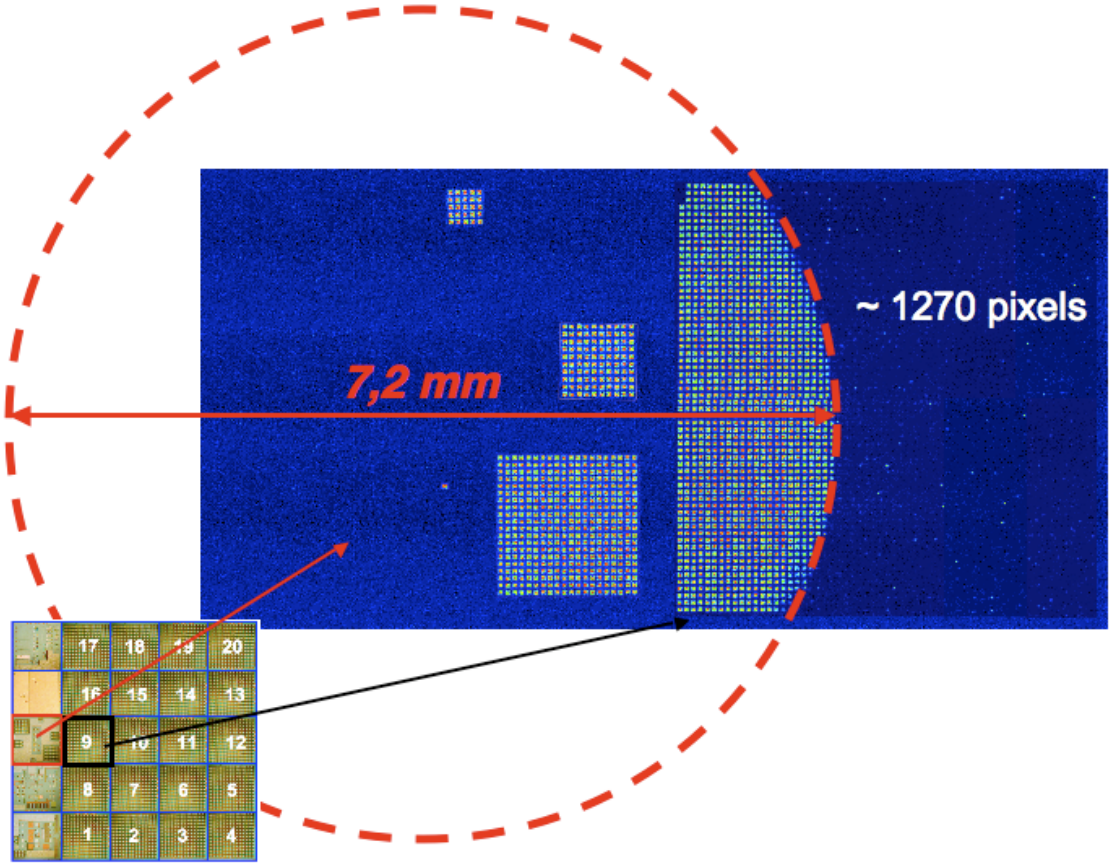

Figure 4.21: *Em.Mi. image of the test pattern. The lighter spots are the hot point. They exactly resemble the beam profile.*

If this last result is considered in the leakage current as a function of the beam dose (Figure 4.16 (b)) an interesting result is obtained: the dark current increases perfectly linearly with the pixel number. For clarity the same figure is reported hereafter (Figure 4.22 (a)). If the standard cell current is multiplied for the real number of pixels invested by the beam (~1270) the current increases linearly with the pixel number. A more clear picture is shown in Figure 4.22 (b) where the dark current at -32V as a function of the pixel number is shown for

unirradiated devices (blue dots) and for the devices irradiated with $1x10^{10}$ Au/cm^2 as a function of the real pixel number. The points collapse on two well defined straight lines.

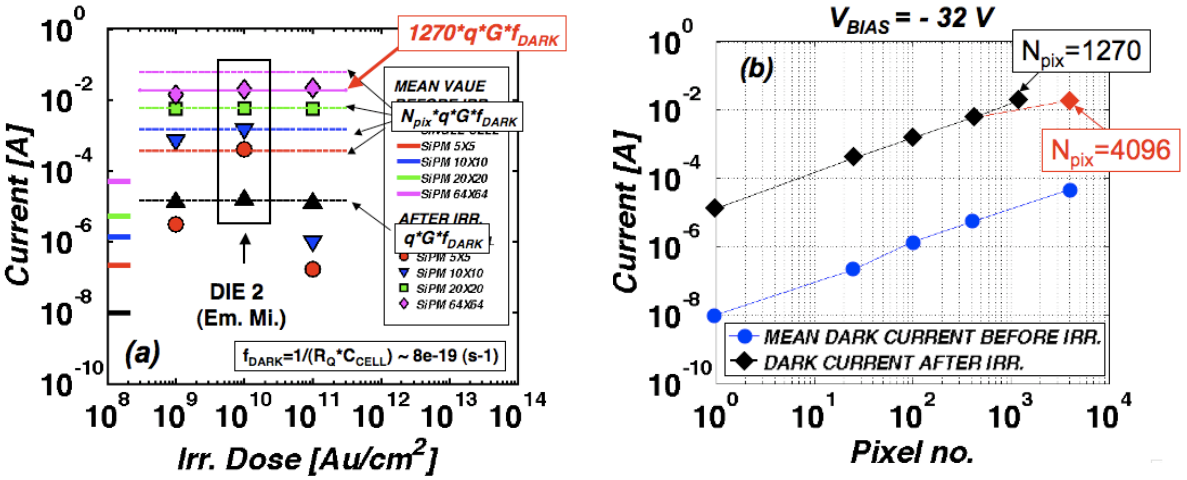

Figure 4.22: *Reverse Current as a function of the Au irradiation dose for a voltage of (a) -20 V and (b) -32V for single cells (black triangles) and 5×5 (red circles), 10×10 (blue triangles), 20×20 (green squares) and 64×64 (magenta diamonds) arrays. The solid lines refer to the unirradiated samples. The solid lines are fits of the data.*

§ 4.5 Conclusion

We performed electrical measurements on SiPM single cells and arrays before and after X-rays irradiation to doses from 0.5 up to 20 krad; light ion (boron) implantation to doses from 3.1×10^7 B/cm^2 up to 5×10^{10} B/cm^2; heavy ion irradiation with Br to doses from 5×10^8 Br/cm^2 to 1.25×10^{10} Br/cm^2 and Au to doses in the range 1×10^9-1×10^{11} Au/cm^2.

X-rays results are very encouraging since they demonstrate that the device does not loose its ability to detect single photons even after 20krad(Si) irradiation. Dramatically different is the case of both light and heavy ion implantation. In fact, the device is not operating correctly even after the lowest implantation doses used and it is completely blind after 5×10^{10} B/cm^2, 5×10^8 Br/cm^2, and 1×10^9 Au/cm^2. For heavy ion irradiation more conclusions can be drown:

leakage currents at voltages below BV (at -20V) are higher than before irradiation and after Br irradiation are independent from the irradiation dose, while after Au irradiation, still a dependence can be observed. Also dark currents are independent from irradiation dose in the Br case, while a linear dependence to the real number of pixels interested by the beam was observed after Au irradiation.

The beam uniformity is a big issue and the devices may be used to infer information on the beam characteristics

Finally, after heavy ion irradiation the sensor is not able to detect photons even at the lowest irradiation dose used in the experiments (3.1×10^{7} B/cm^2 and 1×10^{9} Au/cm^2).

The samples were used to propose a simple method to reconstruct the ion beam intensity profile. It is based on the difference in the dark current at a fixed voltage after and before irradiation. The reconstructed beam has a diameter of 8 mm, as expected.

APPENDIX

A Absorption in semiconductor

The absorption of photons in a semiconductor could be done by several mechanism of transition [92]. The most relevant are:

- *Band-to-Band Transition (Interband):* an absorbed photon could promote an electron from the valence band to the conduction band creating an electron-hole pair (Figure A.1 (a)).
- *Impurity to Band Transition:* an absorbed photon with low energy could results in a transition of an electron or hole from a band to an impurity level (Figure A.1 (b)).
- *Free carrier transition (Intraband)*: an absorbed photon can impart its energy to an electron in a given band, for example in the conduction band, causing it to move higher within the band (Figure A.1 (c)).
- *Phonon transition*: a long wavelength photon can release its energy directly to the lattice crating a vibration i.e. a phonon.
- *Excitonic transition*: a photon absorbed can create an electron and an hole at some distance from each bounded by their mutual Coulomb interaction (like a proton in a hydrogen atom). This entity is called exciton.

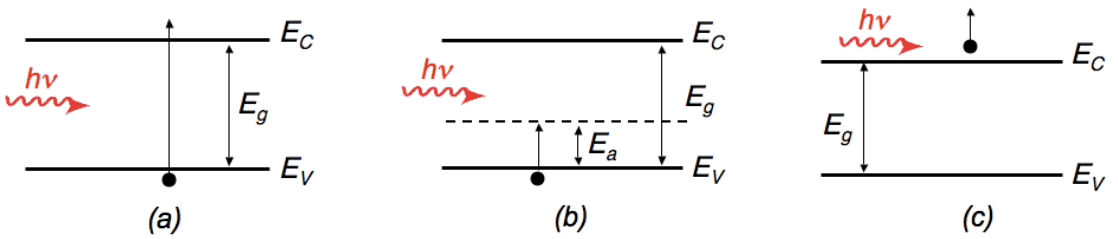

Figure A.1: *Examples of absorption of photons in a semiconductor: (a) Absorption of photons with energy > E_g can lead to band-to-band transition. (b) Absorption of photons with energy = E_a can excite an electron from the valence band into an impurity level. (c) Free carrier transition within the conduction band.*

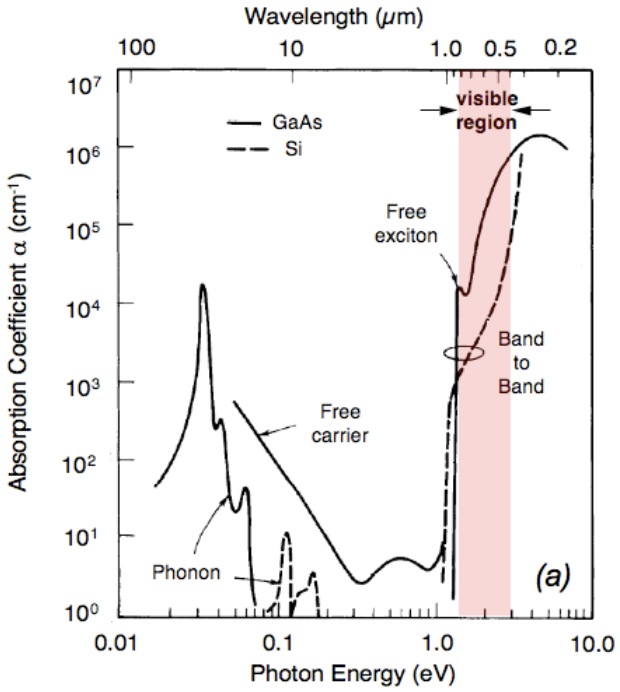

***Figure A.2**:Optical absorption coefficient α versus photon energy for Si and GaAs. in thermal equilibrium at T = 300 K.*

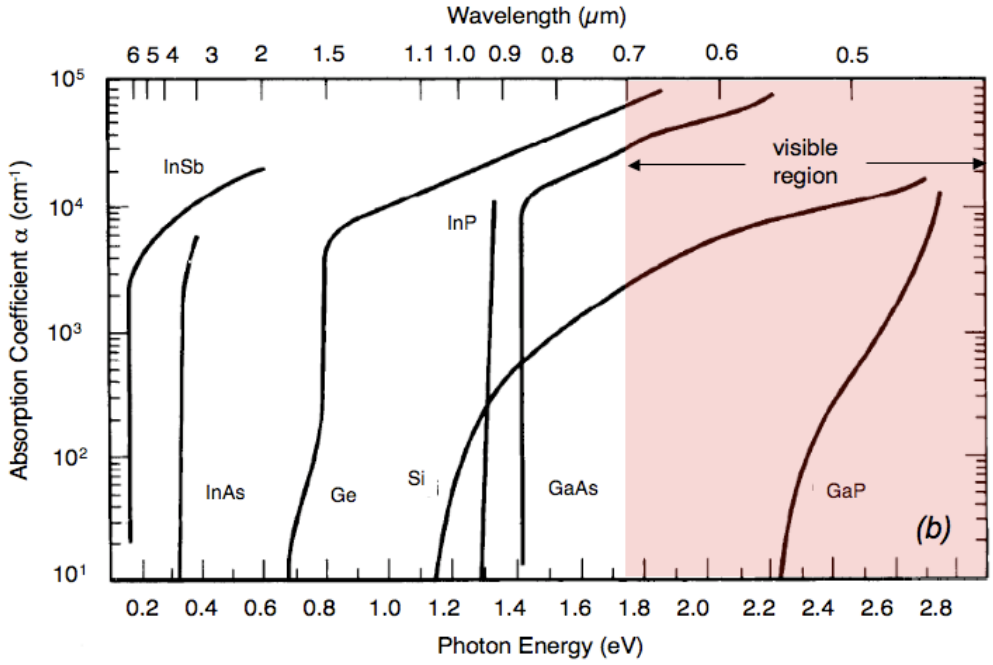

***Figure A.3**: Absorption coefficient versus photon energy for Ge, Si, GaAs and selected other III-V binary semiconductor at T = 300K in an expanded scale [93].*

All these transitions contribute to the overall absorption coefficient of the semiconductor. In Figure A.2 are shown the absorption coefficient of Si and GaAs for a wide region of photon energy and a greater magnification is shown in Figure A.3 for different semiconductor materials. For photons energies greater than the Band Gap energy of the semiconductor, E_g, the absorption is dominated by Band-to-Band transition, that form the basic principle for the photons detection for most of the solid state detector, so in the next we will talk only about this transition.

Band-to band transition, when a photon is absorbed, can occurs only if the energy of the photon is greater than the band gap of the semiconductor ($h\nu > E_g$), because electron from the valence band require such energy to transit in the conduction band. The wavelength of photons corresponding to such condition is called *bandgap wavelength* or *cutoff wavelength* [75] and is given by

$$\lambda_c = \frac{hc}{E_g} = \frac{1.24}{E_g(eV)} \tag{A.1}$$

For wavelength shorter than λ_c the incident photons are absorbed by the semiconductor and an electron-hole pair is generated increasing the overall conductivity. For Si semiconductor (E_g = 1.1eV) $\lambda_c \sim$ 1.12 μm., therefore a silicon detector could be used only to detect visible light.

But this is not the only condition for photons absorption that leads to band-to-band transition. In fact for this process other two conditions must be verified: the conservation of the energy and the conservation of the momentum.

The conservation of the energy requires that for a photon absorbed with energy $h\nu > E_g$ (or $\lambda < \lambda_c$ that is equivalent) the two states with energy E_1 and E_2, in the valence band and in the conduction band respectively, involved in the transition must be separated by $h\nu$. The energy is so conserved if:

$$E_2 - E_1 = h\nu \,. \qquad \text{A.2}$$

The conservation of the momentum require also that the momentum of the two states involved is equal to the momentum of the photon absorbed with energy $h\nu$, i.e:

$$k_2 - k_1 = \frac{2\pi}{\lambda} \qquad \text{A.3}$$

where λ is the wavelength of the photon absorbed and k_1 and k_2 the momentum of the two states involved.

The conservation of energy and momentum, therefore, require that a photon of frequency ν interact with electrons and holes of specific energies and momentum determined by the semiconductor E-k relation.

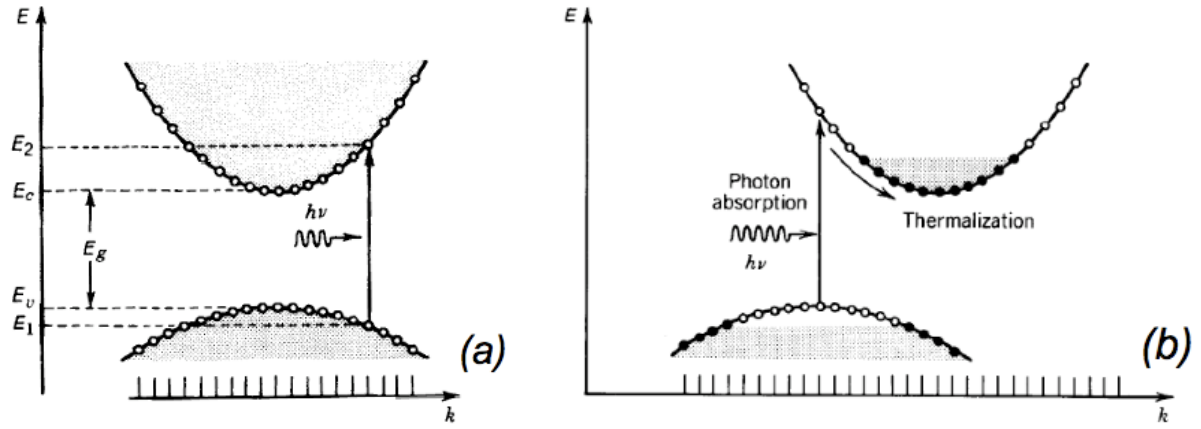

Figure A.4: (*a*) Photon absorption in a direct gap semiconductor. The photon generates an electron-hole pair by vertical transition ($k_1 \approx k_2$). (*b*) Photon absorption in an indirect gap semiconductor. The photon generates an excited electron and a hole by a vertical transition; the carriers then undergo fast transitions to the bottom of the conduction band and top of the valence band, respectively, releasing their energy in the form of phonons.

The photon-momentum magnitude $2\pi/\lambda$ is, however, very small in comparison with the range of values that electrons and holes can assume. The semiconductor E-k diagram extends to values of k of the order $2\pi/a$, where the lattice constant a is much smaller than the wavelength

λ. In direct band gap semiconductor, like GaAs, the momenta of the electron and the hole involved in interaction with the photon absorbed are therefore roughly equal ($k_1 \approx k_2$) and the transition appears as vertival in the E-k diagram (Figure. A.4 (a)). In indirect-gap semiconductor, the conservation of energy and momenta in photon absorption, is readily achieved by means of a two-step process (Figure. A.4 (b)): the electron is first excited to a high energy level within the conduction band by a vertical transition, it then quickly relaxes to the bottom of the conduction band by a process called thermalization in which its momentum is transferred to phonons. The generated hole behaves similarly. Since the process occurs sequentially, it does not require the simultaneous presence of three bodies and is thus not unlikely. Si is therefore an efficient photon detector, as is GaAs.

B Current in a p-n junction

The current of an ideal p-n silicone junction has been well explained by Shockley in 1949 [94]. In an ideal diode the current are due to the diffusion of minority carrier in the quasi neutral regions and follows the relation:

$$J = J_0\left[\exp\left(\frac{qV}{k_B T}\right) - 1\right] \tag{B.2.1}$$

where q is the electron charge, k_B the Boltzmann constant, T the temperature and J_0 is the saturation current. The saturation current I_0 is:

$$J_0 = q\sqrt{\frac{D_p}{\tau_p}}\frac{n_i^2}{N_D} + q\sqrt{\frac{D_n}{\tau_n}}\frac{n_i^2}{N_A} \tag{B.2.2}$$

where D_n and D_p are the diffusion constant respectively of electrons and holes, n_i is the intrinsic carrier concentration of the semiconductor, τ_n and τ_p the electrons and holes lifetime, N_A and N_D the acceptor and donor concentration in the n layer and in the p layer of the junction. Equation B.2 is the celebrated Schockley equation and is the ideal diode law. However the ideal equation can give only qualitative agreement for a real p-n silicon junction. The departure from the ideality are mainly due to surface effect, generation and recombination in the depleted region, high injection condition and series resistance effect.

Generation and recombination processes in the depleted region of the p-n junction lead to an increment of the saturation current. When the p-n junction is forward polarized, the major generation and recombination processes are the capture processes giving a recombination current J_{REC} in addition to the diffusion current . J_{REC} is given by the simplified equation:

$$J_{REC} \approx \frac{qW}{2}\sigma v_{th} N_t n_i \exp\left(\frac{qV}{2k_B T}\right) \tag{B.3}$$

where W is the depletion with, σ is the cross section of the capture center (under the assumption that is the same both for electron and hole), v_{th} the thermal velocity of the carrier and N_t the concentration of the generation-recombination centers. The total forward current is then the sum of the diffusion current of the minority carrier and of the recombination current in the depleted region. For the one-sided n+p abrupt junction the total forward current is:

$$J_F = q\sqrt{\frac{D_n}{\tau_n}}\frac{n_i^2}{N_A}\exp\left(\frac{qV}{k_B T}\right) + \frac{qW}{2}\sigma v_{th} N_t n_i \exp\left(\frac{qV}{2k_B T}\right) \tag{B.4}$$

Experimental data are generally represented by the empirical form:

$$J_F = J_0 \exp\left(\frac{qV}{nk_B T}\right) \tag{B.5}$$

where n is the ideality factor of the diode. If the diffusion current dominates n=1 while if the recombination current dominates n=2. If both current are comparable 1<n<2.

When the p-n junction is reverse polarized, the major generation and recombination processes are the emissions. The generation current in the depleted region in reverse polarization is:

$$J_{GEN} \approx \frac{qn_i W}{\tau_e} \tag{B.6}$$

where τ_e is the effective lifetime.

For the one-sided n+p abrupt junction the total reverse current is:

$$J_R = q\sqrt{\frac{D_n}{\tau_n}}\frac{n_i^2}{N_A} + \frac{qn_iW}{\tau_e} \tag{B.7}$$

In semiconductor where n_i is small, like silicon, the generation current may dominate at lower temperature, but at sufficient high temperature the diffusion current dominate.

In Figure B.1 are show the current voltage characteristics of the ideal diode and of a real silicon p-n junction.

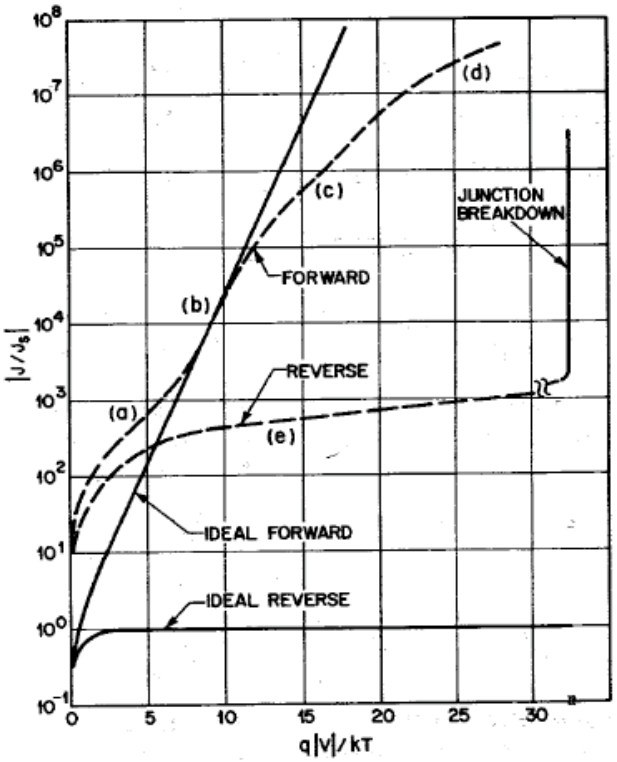

Figure B.1: *Current-voltage characteristics of the ideal diode (continuous line) and of a real Si diode (a) generation-recombination region, (b) diffusion current region, (c) high-injection region, (d) series resistance region, (e) reverse leakage current due to generation-recombination and surface effects [95].*

C Thesis results:

List of the papers published on these results:

1. *"Dark Count in Single Photon Avalanche Si Detectors",*R. Pagano, S. Libertino, G.Valvo, G. Condorelli, B. Carbone, A. Piana, M. Mazzillo, D. N. Sanfilippo, G. G. Fallica, G. Falci, S. Lombardo, Optical Component and Materials VII, Proc of SPIE, vol. 7598 – 75980Z,1-8, (2010)

2. *"Preliminary Radiation Hardness Test of Single Photon Si Detectors",*R. Pagano, S. Libertino, G.Valvo, G. Condorelli, B. Carbone, A. Piana, M. Mazzillo, D. N. Sanfilippo, P. G. Fallica, F. Principato, G. Cannella, G. Falci, S. Lombardo, Silicon Photonics V, Proc of SPIE, vol. 7606 – 760607,1-8, (2010)

3. *"Understanding dark current in pixels of silicon photomultipliers",* R. Pagano, S. Lombardo, S. Libertino, G.Valvo, G. Condorelli, B. Carbone, D. N. Sanfilippo, G. Fallica, Optical Component and Material VII, IEEE, Proc. Of 40th European Solid State Device Research Conference, 265-268 (2010).

List of the conferences attended presenting the results of the thesis

1. Photonics West 2010, S. Francisco, USA, Gennaio 2010, Symposium 7598 – Optical Component and Materials VII

2. Photonics West 2010, S. Francisco, USA, Gennaio 2010, Symposium 7606 – Silicon Photonics V

3. 40th European Solid-State Device Research Conference (ESDDERC 2010), Siviglia, Spain, Settembre 2010.

§ References

[1] W. Smith, "*Effect of Light on Selenium during the passage of an Electric Current*", Nature, (1873), p.303.

[2] A. Einstein, "*Über einen die Erzeugung und Verwandlung des Lichtes betreffenden heuristischen Gesichtspunkt*", Annalen der Physik, 17, 132-148 (1905).

[3] M. Planck, "*Entropy and Temperature of Radiant Heat*" Annalen der Physik, 1. 719-737 (1900)

[4] M. Planck, "O*n the Law of Distribution of Energy in the Normal Spectrum*" Annalen der Physik, 4, 553-558 (1901).

[5] Particle Data Group, "*Particle detectors for accelerator",* http://pdg.lbl.gov/2009/reviews/rpp2009-rev-particle-detectors-accel.pdf.

[6] J. Slepian, "*Hot Cathode Tube*" U.S. Patent 1, 450, 265, April 3, 1923 (Filed 1919).

[7] H. E. Iams and B. Salzberg, "*The secondary emission phototube*" Proc. IRE, 23, 55-64 (1935).

[8] V.K.Zworykin, G.A.Morton, L.Morton, "*The secondary-emission multiplier-a new electronic device*", Proc. IRE, 24, 3, 351-375 (1936).

[9] Hamamatsu Photonics: "*Photomultipliers Tube and Related Products*", available online http://www.hamamatsu.com.

[10] S.O. Flyckt et al., "*Photomultiplier Tubes: Principles and Application*", Philips Photonics, Brive, France (2002).

[11] A. Braem et al., "*Design, Fabrication and Performances of 10-in. TOM HPD*", Nucl. Instrum. Meth. A, 518 (204) 574-578.

[12] S. Einsenhardt et al., "*Hybrid photon detector for LHCb RICH*", Nucl. Instrum. Meth. A, 565 (2006) 234-240.

[13] *"Avalanche Photodiode: Users Guide*", PerkinElmer Optoelectronics, available online http://optoelectronics.perkinelmer.com.

[14] K. Deiters et al., "*Properties of the most recent avalanche photodiodes for the CMS electromagnetic calorimeter*" ", Nucl. Instrum. Meth. A, 442 (2000) 193-197.

[15] R. J. McIntyre, "*Theory of microplasma instability in silicon*", J. Appl. Phys., 32, (1961), 983.

[16] R.H. Haitz, "*Model for the electrical behavior of a microplasma*", J. Appl. Phys., 35 (1964), 1370.

[17] R. H. Haitz, "*Mechanisms contributing to the noise pulse rate of avalanche diodes*," *J. Appl. Phys.*, 36, (1965), 3123–3131,

[18] R. J. McIntyre, "*The distribution of gains in uniformly multiplying avalanche photodiodes: Theory*," *IEEE Trans. Electron Devices*, 19, 6, (1972), 703–713.

[19] "*SPCM-AQR Data Sheet*", PerkinElmer Optoelectronics, available online http://optoelectronics.perkinelmer.com.

[20] S. Cova et al., "*Active-quenching and gating circuits for single-photon avalanche diodes (SPADs)*", IEEE Trans. Nucl. Sci., 29, 1, (1982), 599–601.

[21] F. Zappa et al., "*Fully-integrated active-quenching circuit for single-photon detection*", Proc. of the 28th European Solid-State Circuits Conference, ESSCIRC 2002, pg. 355.

[22] S. Vasile et al., "*High gain avalanche photodiode arrays for DIRC applications*", IEEE Trans. Nucl. Sci. 46 (1999) 848.

[23] P. P. Antich, "*Avalanche photo diode with local negative feedback sensitive to UV, blue and green light*", Nucl. Instrum. Meth. A, 389 (1997) 491-498.

[24] G. Bondarenko, "*Limited Geiger-mode microcell silicon photodiode: new results*", Nucl. Instrum. Meth. A, 442 (2000) 187-192.

[25] V. Golovin, Avalanche Photodetector, Russian Agency for Patents and Trademarks, Patent No. RU 2142175 (1998).

[26] Z. Sadygov, Avalanche Detector, Russian Agency for Patents and Trademarks, Patent No. RU 2102820 (1998).

[27] Z. Sadygov et al., "*Three advanced designs of micro-pixel avalanche photodiodes: Their present status, maximum possibilities and limitations*", Nucl. Instrum. Meth. A 567 (2006) 70.

[28] C. A. Lee et al., "*Ionization rates of Holes and Electrons in Silicium*", Phys. Rew. 134, 3, (1964), 761-774.

[29] S. Cova et al., "*Avalanche photodiodes and quenching circuits for single photon detection*", Appl. Opt. 35,12, (1996), 1956-1976.

[30] M. Yokoyama et al., "*Development of Multi-Pixel Photon Coumters*", Proceding of SNIP Symposium, Standford, California, (2006), available ondine http://arxiv.org/abs/physics/0605241v1.

[31] B. Dolgoshein, "*Status report on silicon photomultiplier development and its applications*", Nucl. Instrum. Meth. A, 563 (2006) 368-376.

[32] M. Lesser, "*Antireflection coatings for silicon charge-coupled devices*", Optic. Eng. 26 (1986) 911.

[33] D. Renker, "*Geiger-mode avalanche photodiodes, history,propertiesand and problems*", Nucl. Instrum. Meth. A, 567 (2006) 48-56.

[34] W.G. Oldham et al., "*Triggering phenomena in avalanche diodes*", IEEE Trans. Electron. Dev. 19 (1972) 1056.

[35] C. Piemonte, "*A new Silicon Photomultiplier structure for blue light detection*", Nucl. Instrum. Meth. A 568 (2006) 224-232.

[36] Y. Musienko et al., "*The gain, photon detection efficiency and excess noise factor of multi-pixel Geiger-mode avalanche photodiodes*", Nucl. Instrum. Meth. A 567 (2006) 57-61.

[37] D. Renker et al., "*Advanced in solid state photon detectors*", JINST **4** P04004, (2009).

[38] W. Schokley, "*Statistics of the Recombination of Holes and Electrons*", Phys. Rev., 87, (1952), 835-843.

[39] R. N. Hall, "*Electron-Hole Recombination in Germanium*", Phys. Rev.,87, (1952), 387.

[40] G.A.M. Hurkx et al., "*A new analytical diode model including tunneling and avalanche breakdown*", IEEE Trans. Elect. Dev. 39, 9, (1992), 2090-

[41] S. Cova et al., "*Trapping Phenomena in Avalanche Photodiode in Nanosecond Scale*", IEEE Elect. Dev. Lett., 12, 12, (1991), 685-687.

[42] C. Piemonte et al., "*Characterization of the First Prototypes of Silicon Photomultiplier Fabricated at ITC-irst*", IEEE Trans. Nucl. Sci., 54,1, (2007) 236-244.

[43] A. Lacaita et al., "*On the bremsstrahlung origin of hot-carrier-induced photons in silicon devices*", IEE Trans. Electron. Dev., 40 (1993) 577.

[44] J. Bude et al., "*Impact ionization in semiconductor: Effects of high electric fields and high scattering rates*", Phys. Rev. B 45 (1992) 10958.

[45] J. H. Swoger and S. J. Kovacic, "*Enhanced luminescence due to impact ionization in photodiodes*", J. Appl. Phys. 74 (1993) 2565.

[46] S. Villa et al., "*Photon emission from hot electrons in silicon*", Phys. Rev. B, 52 (1993) 290.

[47] N. Akil et al.,"*A multimechanism model for photon generation by silicon junctions in avalanche breakdown*", IEEE Trans. Electron. Dev. 46 (1999) 1022.

[48] N. Otte, "*On the efficiency of photon emission during electrical breakdown in silicon*", Nucl. Instrum. Meth. A, 610 (2009) 105-109.

[49] J. Briare et al., "*Principles of Substrate Crosstalk generation in CMOS circuits*", IEEE Trans. Comp. Des. And Sys.,19 (2000) 645-653.

[50] Fan Ji et al. "*Evaluation of electrical crosstalk in high-density photodiode arrays for X-rays imagin application*", Nucl. Instr. Meth. A, 610 (2009) 28-30.

[51] P. Buzhan et al., "*Large area silicon photomultipliers: performance and applications*", Nucl. Instrum. Meth. A, 567 (2006) 78-82.

[52] S. Uozumi, "*Study and development of Multi Pixels Photon Counter fro GLD Calorimiter readout*", PoS, PD07 (2007) 22.

[53] A. Lacaita et al., "*Double epitaxy improves single-photon avalanche diode performance*", IEEE Electr. Lett., 25, 13, (1989),841-843.

[54] B. Dolgoshein, talk presentation, LIGHT07, Tegernsee, Germany, (2007).

[55] A. Spinelli et al,"*Physical and numerical simulation of Single Photon Avalanche Diode*", IEEE Trans. Elect. Dev., 44, 11, (1997),1931-1943.

[56] A. Lacaita et al., "*Observation of avalanche propagation by multiplication assisted diffusion in p-n junctions*", Appl. Phys. Lett., 57 (1990) 489.

[57] P.P. Webb et al., "*Recent developments in silicon avalanche photodiodes*", RCA Eng. 27, (1982),96-102.

[58] A. Lacaita et al., "*Photon-assisted avalanche spreading in reach-trough photodiodes*", Appl. Phys. Lett. ,62, (1993), 606.

[59] G.Ripamonti et al., "*Carrier diffusion effects in the time-response of a fast photodiode*". Sol. State Electr., 28,(1985), 925-931.

[60] N. Otte et all., "*A test of silicon photomultiplier as a readout for pet*", Nucl. Instrum. Meth. A, 545 (2005) 705-715.

[61] V. Andreev et all., "*A high-granularityscintillator calorimeter readout with silicon photomultiplier*", Nucl. Instrum. Meth. A, 540 (2005) 368-380.

[62] E. Grigoriev et al., "*Silicon Photomultiplier and their bio-medical application",* Nucl. Instrum. Meth. A, 571 (2007) 130-133.

[63] V- Dhulla et al., "*Silicon Photomultiplier: Detector for highly sensitive detection of fluorescence",* Proc. of CLEO (2008), CMQ6.

[64] http://www.linearcollider.org/about/What-is-the-ILC/The-project.

[65] Y.Kudenko, "The near neutrino detector for T2K experiment", Nucl. Instrum. Meth. A, 598 (2009) 289.

[66] A. Biland et al.,"*First detection of air shower Cherenkov light by Geiger mode-Avalanche Photodiodes*", Nucl. Instrum. Meth. A, 595 (2008) 165.

[67] I. Braun et al., " *First Avalanche-photodiode Camera Test (FACT): A novel camera using G-APDs for the observation of very high-energy-rays with Cherenkov telescopes"*, ", Nucl. Instrum. Meth. A, 160 (2009) 400-403.

[68] D.J. Herbert et al. "*The Silicon Photomultiplier for application to high-resolution Positron emission tomography*", Nucl. Instrum. Meth. A, 573 (2006) 84-87.

[69] G. Llosà et al., "*First results in the application of silicon photomultiplier matrices to small animal PET*", Nucl. Instrum. Meth. A, 610 (2009) 196-199.

[70] A. Kolb et al., "*Evaluation of Geiger-mode APDs fro PET block detector*", Phys. Med. Biol, 55 (2010) 1815-1832.

[71] M. Mazzillo et al., "*Single-photon avalanche photodiodes with integrated quenching resistor*", Nucl. Instrum. Meth. A, 591, (2008), 367-373.

[72] M. Mazzillo et al. "*Silicon Photomultiplier Technology at STMicroelectronics*", IEEE Trans. Nucl. Sci., 56, 4, (2009), 2434-2442.

[73] E. Sciacca et al., "*Silicon Planar Technology for Single-Photon Optical Detector*", IEEE Ttans. Electr. Dev.,50, 4 (2003) 918-925.

[74] M. Mazzillo, "*Single photon avalanche photodiodes arrays*", Sens. and Act. A, 138, (2007), 306-312.

[75] S. M. Sze, '*Physics of Semiconductors Devices*",2nd edition, J. Wiley & Sons, 1981.

[76] A Poyal et al.,"*Improved extraction of the activation energy of the leakage current in silicon p-n junction diode*", Appl. Phys. Lett., 78, 14 (2001), 1997-1999.

[77] H. M. Chuang, "*Temperature-Dependent Characteristics of Polysilicon and Diffused Resistor*", IEEE Trans. Elect. Dev., 50, 5, (2003), 1413-1415.

[78] A. Poyal et al., "*Silicon substrate effects on the current-voltage characteristics of advanced p-n junction*", Mat. Sci. Eng. B, 73, (2000), 191-196.

[79] H. Aharoni, "*Analysis of n^+p silicon junctions with varying substrate doping concentrations made under ultra-clean processing technology*", J. Appl. Phys.,81, (1997), 1270.

[80] C. R. Crowell and S. M. Sze, "*Temperature Dependence of Avalanche Multiplication in Semiconductor*", Appl. Phys. Lett, 9, 242, (1966).

[81] H. D. Lee et al., "*Characterization of shallow silicided junctions for sub-quarter micron ULSI technology. Extraction of silicidation induced Schottky contact area*", IEEE Trans. Electron Dev. 47, 4, (2000), 762.

[82] C. Piemonte et al., "*Characterization of the First Prototypes of Silicon Photomultiplier Fabricated at ITC-irst*", IEEE Trans. Nucl. Sci., 54, 1, (2007), 236-244.

[83] H. Otono et al., "*On the basic mechanism of Pixelized Photon Detector*", Nucl. Instrum. Meth. A, 610, 1, (2009), 397-399.

[84] G Brianti. "*Distortion of Fast Pulses in Coaxial Cables Numerical Analysis and Applications*" Cern Yellow Report, 65-10, (1965), 196.

[85] K. Schroder, "*Semiconductor Material and Device Characterization*",3rd ed.,Wiley-Interscience (2006) pp 262.

[86] V. Bindi et al., "*Preliminary study of silicon photomultipliers for space missions*", Nucl. Instrum. Meth. A, 572, (2007), 662–667.

[87] T. Matsumura et al., "*Effects of radiation damage caused by proton irradiation on Multi-Pixel Photon Counters (MPPCs)*", Nucl. Instrum. Meth. A, 603, (2009), 301–308.

[88] S. Sanchez Majos et al., "*Characterisation of radiation damage in silicon photomultipliers with a Monte Carlo model*", Nucl. Instrum. Meth. A, 594, (2008), 351–357.

[89] R. Bencardino et al., "*Development of a Fast-Neutron Detector With Silicon Photomultiplier Readout*", IEEE Trans. Nucl. Sci. 56, (2009), 1129–1134.

[90] Pagano, R. et al., "*Dark Count in Single Photon Avalanche Si Detectors*", Proc. SPIE 7598, (2010), 75980Z.

[91] Libertino et al., "*The effect of impurity content on point defect evolution in ion implanted and electron irradiated Si*", Appl. Phys. Lett. 70, (1997), 3002–3004.

[92] B. E. A. Saleh, M. C. Teich, "*Fundamentals of photonics*", J. Wiley & Sons, New York, 1991.

[93] G. E. Stillman,V et al., "*III-V Compound Semiconductor Devices: Optical Detectors*", IEEE Trans. Elect. Dev., 31, (1984), 1643-1655.

[94] W. Shockley, "*The theory of p-n Junctions in Semiconductors and p-n Junction Transistor*", Bell Sys. Tech. J., 28, (1949), 435.

[95] J. L. Moll, "*The evolution of the Theory of the Current-Voltage Characteristics of a p-n junction*", Proc. IRE, 46, (1958), 1076.